



SAPIENZA
UNIVERSITÀ DI ROMA

Dark Matter search with bolometric detectors

Scuola di Dottorato in Scienze Astronomiche,
Chimiche, Fisiche e Matematiche "Vito Volterra"
Dottorato di Ricerca in Fisica – XXIII Ciclo

Candidate

Filippo Orio

ID number 694438

Thesis Advisor

Prof. Fernando Ferroni

A thesis submitted in partial fulfillment of the requirements
for the degree of Doctor of Philosophy in Physics

December 15th 2010

Thesis not yet defended

Filippo Orio. *Dark Matter search with bolometric detectors.*

Ph.D. thesis. Sapienza – University of Rome

© 2010

EMAIL: filippo.orio@roma1.infn.it

*A mio padre,
che guardava il mondo
con occhi curiosi*

Contents

Introduction	2
1 The Dark Matter problem	3
1.1 Standard Cosmological Model	3
1.2 Dark Matter evidences	5
1.2.1 Spiral galaxies	5
1.2.2 Galaxy clusters	6
1.2.3 The Early Universe	6
1.2.3.1 The Big Bang Nucleosynthesis	7
1.2.3.2 The Cosmic Microwave Background	8
1.2.3.3 Large Scale Structure Formation	10
1.3 Dark Matter candidates	12
1.3.1 Light neutrinos	14
1.3.2 Axions	15
1.3.3 Weakly Interacting Massive Particles (WIMPs)	15
2 Dark Matter detection	19
2.1 Direct vs indirect detection	19
2.2 WIMP rate in a detector	21
2.2.1 Particle density and velocity distribution	21
2.2.2 Differential rate	22
2.2.3 Scalar and axial-vector interactions	23
2.2.4 Nuclear form factor correction	24
2.2.5 Quenching factor	25
2.2.6 Combining results	25
2.3 The annual modulation	25
2.4 WIMP detection techniques	28
3 TeO₂ bolometric detectors for 0νDBD search	33
3.1 Neutrino physics	34
3.1.1 Neutrino oscillations	34
3.1.2 Neutrino masses	36
3.1.3 Neutrinoless Double Beta Decay (0 ν DBD)	38
3.2 Experimental search for 0 ν DBD	40
3.2.1 Past and present experiments	42
3.3 CUORE and its precursors	44
3.3.1 CUORICINO	45

3.3.2	CUORE	46
3.3.3	On the road to CUORE: CUORE-0	48
3.3.4	CUORE Crystals Validation Run 2	49
4	The bolometric technique	51
4.1	Working principles	51
4.1.1	Energy absorber	52
4.1.2	The choice of TeO ₂	53
4.1.3	The thermal sensor	54
4.1.4	NTD-Ge thermistors	56
4.2	Detector operation	57
4.3	The single module	59
4.4	Signal readout	60
4.5	Detector noise	61
4.6	First level analysis	62
5	A new trigger for CUORE low energy analyses	65
5.1	Optimum Filter algorithm	65
5.1.1	White Noise case	66
5.1.2	Generalized case	67
5.1.3	The DFT convolution wraparound	67
5.1.4	Filter implementation	70
5.2	Optimum Trigger	72
5.3	Pulse Shape	74
5.4	Trigger efficiency	76
5.4.1	Low Energy Scan with Heater Pulses	76
5.4.2	Montecarlo evaluation and validation	78
6	Application and results	81
6.1	CCVR2 Analysis	81
6.1.1	CCVR2 setup	82
6.1.2	Calibration	83
6.1.3	Cuts efficiency	86
6.1.4	Time correlation check	88
6.1.5	Coincidences check	91
6.1.6	First Level Analysis Results	92
6.2	A first Optimum Trigger application: ¹²³ Te L line	92
6.2.1	The ¹²³ Te decay	94
6.3	Dark Matter limits from direct detection	96
6.4	Annual modulation in CUORE	97
	Conclusions	103
	Acknowledgments	105
A	Average Pulse and Noise Power Spectrum evaluation	107
B	Comparison of χ^2_{OT} with TVL and TVR	109

C Optimum Trigger Efficiencies in CCVR2 run	111
D Comparison with standard trigger on N-Pulses measurement	117
Bibliography	121

Introduction

What is the Universe made of? This enigma has always fascinated the mankind and in the recent years, step by step, we are moving closer to a solution.

From detailed investigations of the cosmic microwave background radiation as well as from galaxy surveys, a cosmological concordance model has been derived in which the most prominent contribution to the cosmological energy density comes from the cosmological constant Λ often called Dark Energy. Ordinary matter would only contributes to 4%, whereas the second biggest fraction would consist of Dark Matter.

The most favorable Dark Matter candidate is in the form of weakly interacting massive particles, so-called WIMPs. The attempts to detect WIMP Dark Matter proceed along two separate experimental ways. On one hand, the indirect searches in space-based experiments aim to the detection of WIMPs through the observation of their annihilation products. On the other hand, direct searches for WIMPs are carried on in low-background underground experiments, where the direct signal of a WIMP interaction with the target nucleus is detected.

We can enumerate a huge amount of underground experiments which may contribute to the Dark Matter quest even if, sometimes, it is not their main scientific aim. This is the case of the CUORE experiment, a bolometric experiment currently under construction at Laboratori Nazionali del Gran Sasso, that is optimized for the search of the double beta decay without emission of neutrinos. This process violates the lepton number by two units, and has never been observed. The observation of this nuclear decay would imply that lepton number is not conserved and that neutrinos are Majorana particles, a breakthrough in the picture of nature we have. Moreover it could provide information on the absolute mass scale of neutrinos because a virtual neutrino is exchanged and the propagator is proportional to its mass.

This Ph.D. work was performed within the CUORE collaboration, that will be ready to start a 1-ton experiment within a couple of years. This experiment will search for the neutrinoless double beta decay of ^{130}Te using TeO_2 bolometers. Bolometers are calorimeters working at low temperatures able to measure the temperature rise produced by the energy release of an impinging particle. Such detectors are hence sensitive to nuclear recoils and can also be used to search for Dark Matter interactions. The only caveat is that these recoils have energies of few keV, while CUORE bolometers have thresholds of the order of tens of keV.

This thesis concerns the development of a new trigger for CUORE, capable of pushing the energy threshold down to few keV. Accessing this region, TeO_2 bolometers could play an important role in the search of Dark Matter interactions and nuclear decays.

This thesis is divided in six chapters. In Chapter 1 we give an overview on the observational evidence for Dark Matter in cosmology and astrophysics and we discuss the possible candidates for baryonic and non-baryonic dark matter, focusing on WIMPs.

In Chapter 2 we discuss the detection of WIMP Dark Matter. We calculate the expected signal from Dark Matter interactions, including the annual modulation effect, and, at the end of the chapter, we shortly review the most recent results from running Dark Matter experiments.

In Chapter 3, after a brief overview of neutrino physics, the scientific motivations for the search of neutrinoless double beta decay are introduced, followed by a description of the experimental status. At the end of the chapter we focus on CUORE and its precursors.

In Chapter 4 we describe the bolometric technique and the materials used in CUORE. In Chapter 5 a new trigger algorithm, based on the Optimum Filter technique, is proposed.

In Chapter 6 we apply the the developed trigger on data and we analyze the low energy region of the CUORE bolometers. At the end of the chapter we estimate CUORE performances in the Dark Matter quest.

Chapter 1

The Dark Matter problem

The Swiss astronomer Fritz Zwicky first reported the observation that the galaxies of the Coma cluster move faster than expected [1]. Taking into account the cluster luminosity to deduce its mass, the orbital velocities of the individual galaxies in the cluster should be lower than observed. It was the 1933. During the last 70 years, this picture has only undergone a small correction and still holds today. Vast observations from scales of galaxies ($\lesssim 100$ kpc) to clusters of galaxies (hundreds of Mpc) have the same problem: the mass that shines falls short in accounting for the gravitational effect. As a solution, Zwicky proposed that there should be a non-luminous matter component that was later referred to as “Dark Matter”.

In this chapter we present the theoretical framework used to modelize our Universe and the manifold observational evidences of Dark Matter existence. We also discuss the most favourable Dark Matter candidates.

1.1 Standard Cosmological Model

The current cosmological picture is based on few assumptions [2]. First of all, the laws of physics are assumed to hold in all local inertial frames (*Lorentz invariance*). In addition, the Earth position is assumed not to be atypical in the Universe. Consequently, the observed large scales isotropy leads to the conclusion that the Universe must appear to be isotropic from any arbitrary location. This requires the Universe to be homogeneous (*Cosmological Principle*).

The further assumption that the spatial component of the metric describing the Universe can be time dependent leads to the Robertson-Walker metric:

$$ds^2 = dt^2 - a^2(t) \left(\frac{dr^2}{1 - kr^2} + r^2 d\theta^2 + r^2 \sin^2\theta d\phi^2 \right) \quad (1.1)$$

where $a(t)$ is the time-dependent scale parameter describing the expansion or contraction of the Universe. The energy content of the Universe is directly connected to the curvature parameter k , which can have three possible values for an open, infinite Universe with hyperbolic curvature ($k = -1$), a flat, infinite Universe with no curvature ($k = 0$) or a closed and finite Universe with spherical curvature ($k = +1$). Within the Robertson-Walker metric, Einstein’s equations of general relativity simplify to the so-called Einstein-Friedmann equations. They describe the time evolution of the cosmic scale factor, dependent on the density $\rho(t)$ and the pressure $p(t)$

of the cosmic substrate as well as on the cosmological constant Λ :

$$\left(\frac{\dot{a}(t)}{a(t)}\right)^2 = H^2(t) = \frac{8\pi G\rho(t)}{3} - \frac{k}{a^2(t)} + \frac{\Lambda}{3} \quad (1.2)$$

$$\frac{\ddot{a}(t)}{a(t)} = -\frac{4\pi G}{3}(\rho(t) + 3p(t)) + \frac{\Lambda}{3} \quad (1.3)$$

where $H(t)$ is the expansion rate of the Universe (*Hubble parameter*) and G is the Newtonian gravitational constant.

One can define a critical density $\rho_{c,0}$ at the present epoch $t = t_0$ as:

$$\rho_{c,0} = \frac{3H_0^2}{8\pi G} . \quad (1.4)$$

This term was originally used as a means to determine the geometry of the Universe where ρ_c is the critical density for which the Universe is flat (assuming a vanishing cosmological constant). Since this value depends only on constants, it is itself a universal constant, except for the not yet certain, accurate value for the Hubble constant H_0 . By introducing the dimensionless Hubble scaling factor

$$h_0 = \frac{H_0}{100 \text{ km s}^{-1} \text{ Mpc}^{-1}} , \quad (1.5)$$

the present value is $\rho_{c,0} = h_0^2 \cdot 18.8 \cdot 10^{-30} \text{ g cm}^{-3}$. One can also introduce the total matter density parameter

$$\Omega_m = \frac{\rho}{\rho_c} \quad (1.6)$$

and the equivalent density parameter for the cosmological constant

$$\Omega_\Lambda = \frac{\Lambda}{3H_0^2} . \quad (1.7)$$

Using these definitions into Eq. 1.2, we obtain:

$$1 + \frac{k}{a^2 H_0^2} = \Omega_m + \Omega_\Lambda , \quad (1.8)$$

meaning that the present total energy density of the Universe ($\Omega_{tot} = \Omega_m + \Omega_\Lambda$) is directly linked with its curvature.

The equations 1.2 and 1.3, together with the values of Ω_m and Ω_Λ , determine the past and the future of the Universe. Observations in the last decade indicate that the Universe is best described by models with a cosmological constant density $\Omega_\Lambda \simeq 0.75$.

The non-vanishing term Ω_Λ can be attributed within the framework of quantum field theory to the energy density of the vacuum and is often called Dark Energy. The associated negative pressure of the quantum vacuum causes in general relativity a gravitational repulsion. In consequence, for models with a positive Λ the before slowed down expansion can become an accelerated expansion in a later phase of the Universe. The ultimate fate of all models with $\Lambda \neq 0$ are determined by the present values of H_0 , Ω_m and Ω_Λ . Hence great observational effort is made to determine these values as precisely as possible.

1.2 Dark Matter evidences

1.2.1 Spiral galaxies

The first Dark Matter evidence (after the Zwicky claim) came from galaxy dynamics in the 70's, when V. C. Rubin and W. K. Ford [3] measured the rotation curves of the outermost stars of the Andromeda galaxy. A spiral galaxy such as Andromeda consists of a central bright bulge surrounded by a rotating disk of younger stars. They correspond to about 80% of light galaxies in areas of low density, while in core areas of galaxy clusters they are very rare (about 10%).

Measurements of the galactic rotation speed as a function of radius have now been conducted for many spiral galaxies. Assuming that the stars in the spiral galaxy have a circular orbit around the center of the galaxy, we can calculate the rotation velocity by equating the gravitational and centrifugal forces using Newtonian dynamics:

$$v(r) = \sqrt{\frac{GM(r)}{r}} \quad (1.9)$$

where $M(r) = 4\pi \int \rho(r)r^2 dr$ and $\rho(r)$ is the mass density profile that should be falling beyond the optical disk. If the matter density was given only by the visible mass, the velocity would be expected to drop $\propto 1/\sqrt{r}$ outside the disk, where $\rho(r)$ becomes negligible. Experimental data show that velocity keeps a constant trend even far beyond the visible disk (see Fig. 1.1).

The difference between the observed rotation curves and the ones expected by the luminous material is ascribed to the gravitational effect of Dark Matter. A constant orbital velocity can be obtained by introducing an additional spherically symmetric halo component, so that the total mass is $M(r) \propto r$ and the density is $\rho(r) \propto r^{-2}$. This Dark Matter halo is furthermore supported by additional observa-

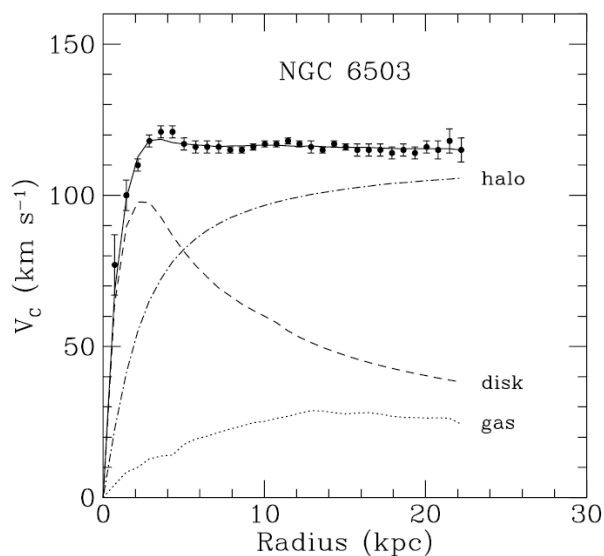


Figure 1.1. Rotation curve of NGC 6503. The dotted, dashed and dash-dotted lines are the contributions of gas, disk and Dark Matter halo, respectively. Figure taken from [4].

tions, *e.g.* vertical velocity dispersions that support the fact that the Dark Matter cannot be contained alone in the disk, as well as material orbiting perpendicularly to the normal disk, which concludes to an almost spherical gravitational potential [5].

1.2.2 Galaxy clusters

As told at the beginning of this chapter, the first Dark Matter evidence came from a much larger scale than that of a single galaxy, the Coma galaxy cluster. Galaxy clusters are aggregates of a few hundred to a few thousand galaxies, gravitationally bound to each other and otherwise isolated in space.

The relative contribution of Dark Matter component in a galactic cluster is specified by the Mass-to-Light Ratio (M/L), that represents the ratio of gravitational mass and luminosity for an object. For example, the Coma cluster has a M/L value of 400 solar masses per solar luminosity. Studies of this ratio at different scales confirmed that these structures are completely dominated by non-luminous matter [6].

The mass of a cluster can be determined using different methods. One consists in measuring the velocities of individual galaxies in the clusters at dynamical equilibrium [7] and estimating the total cluster mass from the virial theorem, according to which the average kinetic energy $\langle T \rangle$ and the average potential energy $\langle V \rangle$ of a system are related by the equation

$$\langle T \rangle = -\frac{1}{2}\langle V \rangle . \quad (1.10)$$

The resulting potential energy is used to infer the mass of the cluster.

The X-ray emission of hot intra-cluster gas, assumed to be at hydrostatic equilibrium, can also be used to estimate the cluster mass [8]. X-ray profiles of the gas are measured and then fit to temperature and density distribution models to determine the mass of the cluster.

A third technique for mass inference is the gravitational lensing method [9]. General relativity states that compact gravitational bodies bend nearby photon paths. In particular, the deflection angle α of a light ray passing at a distance r from a body of mass M is

$$\alpha = \frac{4GM}{c^2} \frac{1}{r} \quad (1.11)$$

where G is the gravitational constant and c is the velocity of light. Thus, when light rays pass through large gravitational masses such as galaxy clusters, they are deflected by the gravitational field produced by the cluster, in a manner similar to the way an optical lens bends light to form an image (see Fig. 1.2).

1.2.3 The Early Universe

We have seen in the previous sections that, on distance scales of the size of galaxies and clusters of galaxies, evidence of Dark Matter appears to be compelling. Despite this, the observations discussed do not allow us to determine the total amount of Dark Matter in the Universe. We discuss in these sections how such information can be extracted from the analysis of the light nuclei abundances, related to Big Bang Nucleosynthesis (BBN), and from the study the Cosmic Microwave Background (CMB).

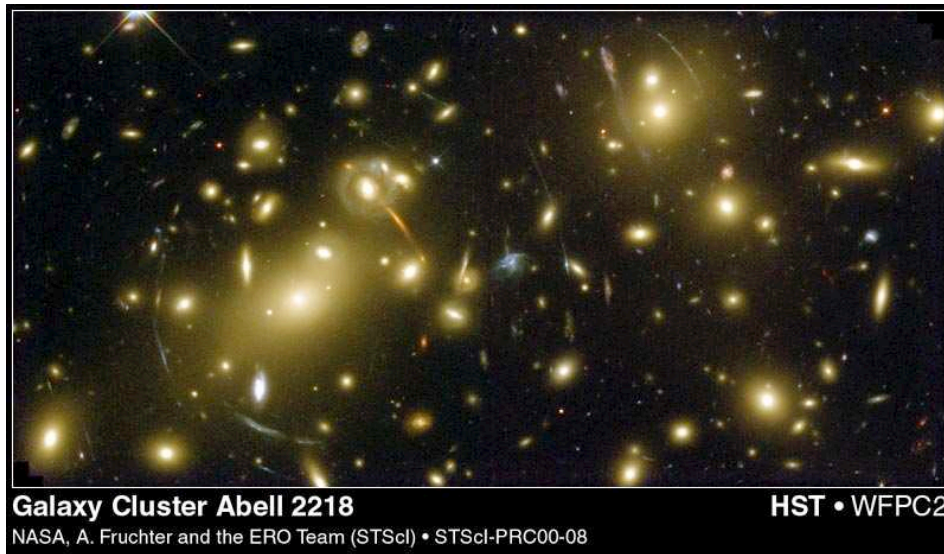


Figure 1.2. Galaxy Cluster Abell 2218 with giant luminous arcs and many arclets. Light from distant galaxies passes by the gravitational mass of the cluster and gets bent, creating a lensing effect. Picture from the Hubble Space Telescope.

1.2.3.1 The Big Bang Nucleosynthesis

To study nature on its largest scales, we turn to observations related to the early Universe. Studies of Big Bang Nucleosynthesis lead to robust and independent measurements of the baryon density of the Universe, and therefore represent a cornerstone for the existence of nonbaryonic Dark Matter. Big Bang Nucleosynthesis is a non-equilibrium process that took place over the course of a few minutes in an expanding, radiation-dominated plasma with high entropy and many free neutrons [10]. The predictions of Big Bang Nucleosynthesis for the light element abundances are shown in Fig. 1.3.

In the first 10^{-5} s of the Universe, before the QCD transition, there were roughly equal numbers of electrons, positrons, neutrinos, antineutrinos and photons. The ratio of photons to nucleons, *i.e.* protons and neutrons, was more than a billion to one. The nuclei had not been formed and the ratio of neutrons and protons was unity due to the weak processes that interconvert them. At about one second, when the Universe had cooled to around 10^{10} K, the weak processes were not able to keep the same number of neutrons and protons. At the temperature of $\sim 10^9$ K the first formation of D, ^3H , ^3He and ^4He took place. As the Universe continued to expand and cool, the processes maintaining equilibrium slowed down according to the temperature evolution and, after five minutes, most neutrons were “trapped” in ^4He nuclei, while most protons remained free. There was also formation, in much smaller amounts, of D, ^3He , ^7Li but the low density and temperature caused the elemental composition of the Universe to remain unchanged until the formation of the first stars a few billion years later.

The photon density sets the time and interval of nucleosynthesis through its control of the Universe’s expansion rate; given equal photon densities, a greater baryon density leads to a faster rate of fusion to ^4He and fewer nucleons left over in ^2H

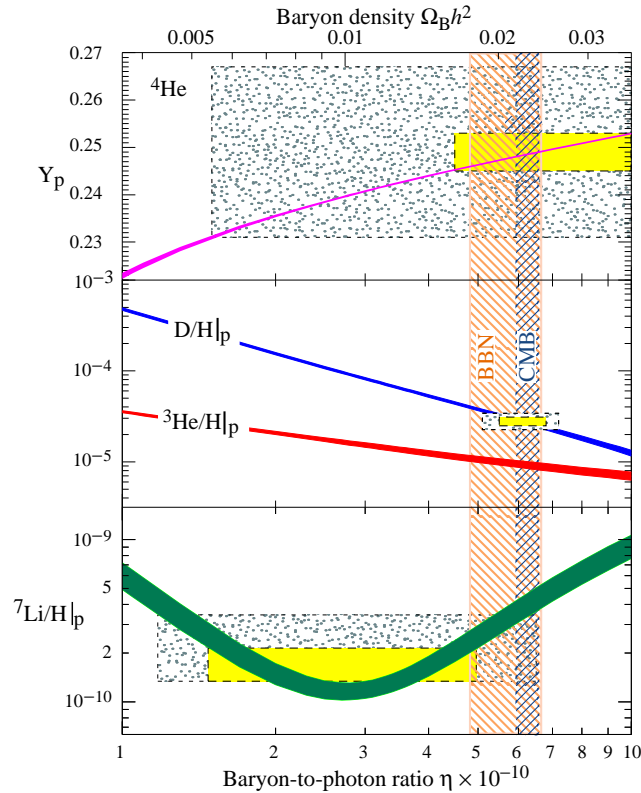


Figure 1.3. The abundances of ${}^4\text{He}$, D, ${}^3\text{He}$, and ${}^7\text{Li}$ as predicted by the standard model of Big Bang Nucleosynthesis. The bands show the 95% CL range. Boxes indicate the observed light element abundances (smaller boxes: $\pm 2\sigma$ statistical errors; larger boxes: $\pm 2\sigma$ statistical and systematic errors). The narrow vertical band indicates the CMB measure of the cosmic baryon density (see Sec. sec:CMB), while the wider band indicates the BBN concordance range (both at 95% CL). Figure from [11].

and ${}^3\text{He}$. Since the photon density is well-known from the microwave background’s black body temperature, light element ratios thus provide an excellent “baryometer” with which to measure the abundance of ordinary matter.

Deuterium is the most powerful of these baryometers, since it is a delicate nucleus, easily destroyed within stars and therefore no longer created in the modern Universe. Since the deuterium abundance is sensitive to η and decreases with time, any measurement of deuterium yields a direct upper limit on η . Current deuterium measurements from quasar absorption lines [11] indicate $4.7 \leq \eta \leq 6.5$ (95% CL), implying a modern baryon density of $0.017 \leq \Omega_b h^2 \leq 0.024$ (95% CL), *i.e.* $\Omega_b \simeq 0.05$. This means that all the baryonic matter that we are made of and that we study at particle accelerators constitutes only less than 5% of the energy density of the Universe.

1.2.3.2 The Cosmic Microwave Background

Nowadays, a photon is likely to travel several Hubble distances, 3700 – 4700 Mpc, before being scattered or absorbed. However, the expansion of the Universe implies

that at earlier times, the Universe was hotter and denser. At the early age of a temperature above ~ 3000 K, the formation of stable atoms was hindered, as matter and radiation were in thermal equilibrium. Matter existed in an opaque plasma state of ionized atoms, which strongly absorbed electromagnetic radiation of all wavelengths. When the plasma cooled below the temperature of ~ 3000 K, it was cool enough for hydrogen and helium nuclei to collect electrons and become stable atoms. Stable atoms absorb only characteristic frequencies or frequencies high enough to ionize them. This means that the expanding Universe became transparent to almost all wavelengths, at least for photons with quantum energy less than the ionization energy of the atoms. That is called the era of decoupling of matter and radiation.

If the Universe began in a hot and dense state, then it should be filled with a relic background of the last scatterings before decoupling. This remnant of the transparency point, at which the expanding Universe dropped below about 3000 K so that radiation could escape, should have a Planck black-body spectrum:

$$\int_0^\infty \frac{\nu^3 d\nu}{e^{h\nu/k_B T_r} - 1} \propto T_R^4 \quad (1.12)$$

where ν is the radiation frequency, T_R is the radiation temperature, h and k_B are respectively the Planck constant and the Boltzmann constant. This microwave radiation, so-called Cosmic Microwave Background (CMB), is isotropic and constant with time.

The FIRAS instrument (Far Infrared Absolute Spectrophotometer [12]) inside the COBE satellite (COsmic Background Explorer [13]) measured, at any angular position on the sky, the spectrum of the CMB to be an ideal blackbody up to 1 part in 10^4 . However, the DMR instrument (Differential Microwave Radiometer [14]) also inside COBE found for the first time that the CMB have intrinsic anisotropies at a level of a part in 10^5 . Later, the Wilkinson Microwave Anisotropy Probe (WMAP [15]) mission was designed to determine the geometry, content, and evolution of the Universe via a 13 arcminute FWHM resolution full sky map of the temperature anisotropy of the CMB. Fig. 1.4 shows the temperature fluctuations of the CMB anisotropy in the full sky as measured by COBE and WMAP.

The microwave background's temperature fluctuations record inhomogeneities in the photon-baryon fluid at the era of last-scattering. These inhomogeneities can be seen as incoherent acoustic waves in the photon-baryon fluid of the last-scattering surface, and the densities of baryonic and non-baryonic matter have strong effects upon these oscillations: baryons increase the inertia of the oscillating photon-baryon fluid, while Dark Matter reduces the driving effect of those oscillations upon the gravitational potential. Fig. 1.5 shows the CMB power spectrum from various experiments. On the one hand, the position of the first peak in Fig. 1.5 probes spatial geometry and leads to an experimental value of $\Omega_{tot} = 1.011 \pm 0.012$. Since we know (see Sec. 1.1) that $\Omega_{tot} = \Omega_m + \Omega_\Lambda = 1$ for a flat Universe in the Standard Cosmological Model, we do have a flat Universe. On the other hand, the relative height of peaks in Fig. 1.5 probes baryon density. Using WMAP 7 years data only [16], the best fit values for cosmological parameters for the flat Universe model are:

$$\Omega_m h^2 = 0.1334 \pm 0.0055 \simeq 0.266 h^2 \quad (1.13)$$

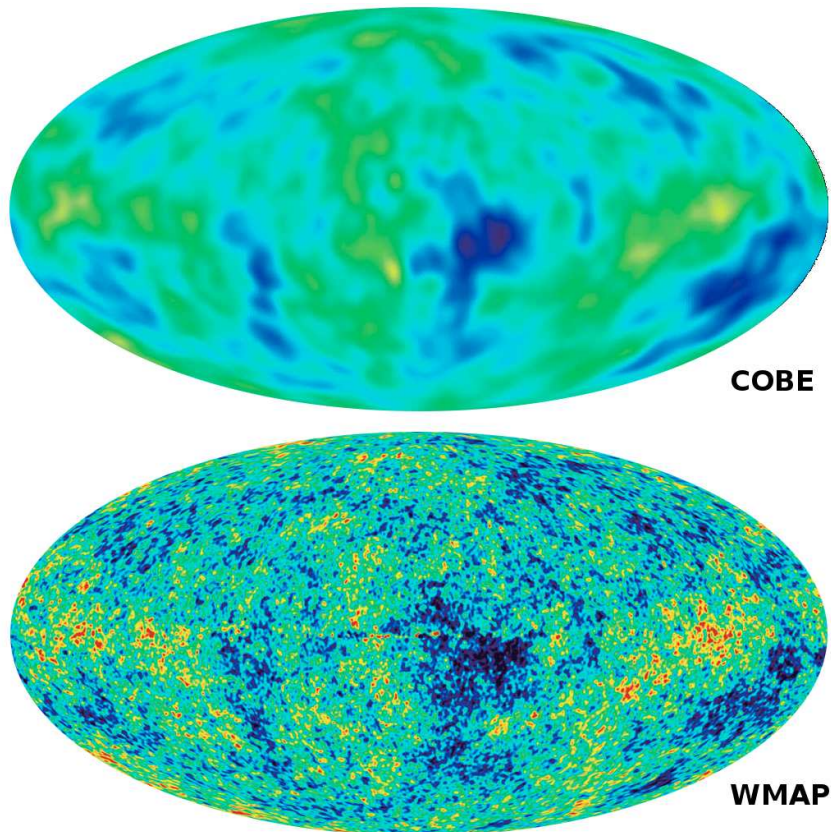


Figure 1.4. Full sky maps of the CMB anisotropies computed by data measured with the COBE (upper) and WMAP (lower) experiment corrected by the foreground of the galactic plane and effects by the local motion. Pictures from <http://map.gsfc.nasa.gov/>.

$$\Omega_b h^2 = 0.02258 \pm 0.00057 \simeq 0.0449 h^2 . \quad (1.14)$$

The result of Ω_b is in agreement with estimations using arguments from BBN that we have described in the previous section. The contribution of baryonic matter is very little compared with the total of matter in the Universe, approximately 25% of the matter density of the Universe is thus not baryonic and therefore a natural solution is to search for undiscovered particles.

1.2.3.3 Large Scale Structure Formation

Very rigorous constraints on the cosmological model as well as on the Dark Matter distribution arise from arguments of cosmic structure formation. As mentioned in the previous section, the precise black-body nature of the CMB supports the theory of an almost perfectly homogeneous early Universe with tiny modulation of its density field, yielding to the small anisotropies of the CMB. These density contrasts are enhanced by gravitation force with time, leading eventually to the formation of galaxies or clusters if the selfgravity of an overdense region becomes large enough to decouple from the overall Hubble expansion.

Currently, the Sloan Digital Sky Survey (SDSS) is systematically mapping a quarter of the entire sky and determining the position and absolute brightness of

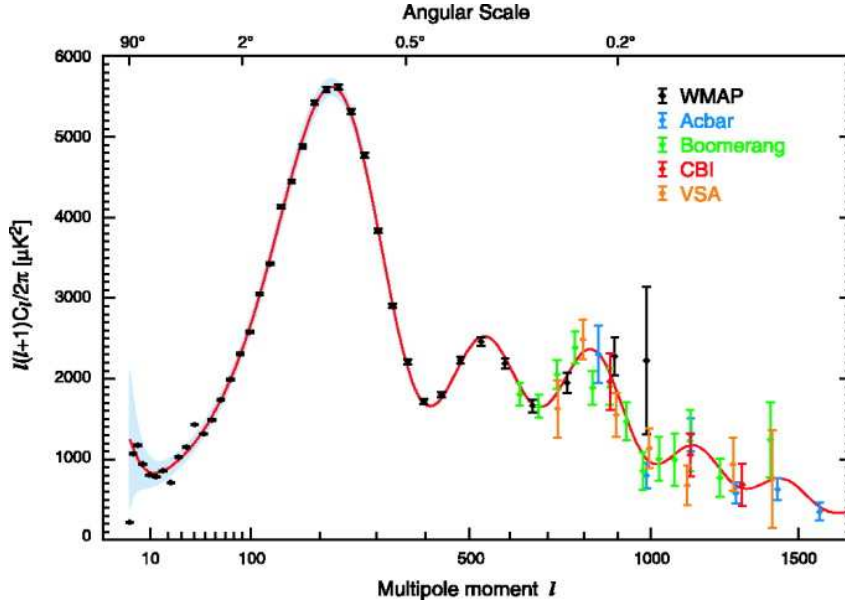


Figure 1.5. Temperature power spectrum of primary CMB anisotropies as estimated from WMAP data. WMAP power spectrum in black and a best fit standard cosmology model, compared with other measurements of the CMB power spectrum such as Boomerang, Acbar, CBI and VSA. Figure from [17].

more than 100 million celestial objects [18]. Using this galaxy survey measuring the geometry of the Universe through the distance-redshift relation, one could extract oscillatory features in the matter power spectrum as predicted in the baryon acoustic oscillations [19]. The latest results [20], combining the obtained matter distribution with the WMAP data of the CMB, also lead to a scenario with a best-fit value of $\Omega_m = 0.286 \pm 0.018$ (68% CL). This value does not include any information from the overall shape of the power spectra and hence is an extremely clean cosmological measurement expected to be independent of systematics.

Among cosmologists there is much work done which attempts to model the observed large-scale structure of the Universe, *e.g.* SDSS, by numerical computer simulations. Particularly, lots of N-body-simulations are done based on the Big Bang model. Starting with assumptions about the type of matter that makes up the Universe and initial density perturbations, it is possible to simulate the evolution of the distribution of matter in time. The results can then be compared with the observations to support or refute cosmological models and hence constrain the model parameters. Within the simulations one can distinguish mainly two different scenarios describing the matter properties.

On one hand, one speaks of Hot Dark Matter (HDM), if the particle masses are very low ($m \leq 100$ eV), so they stay relativistic for a long time. Due to their relativistic behaviour, primordial density fluctuations of galactic sizes or smaller are damped by free streaming of these particles. Hence large scale structures form first and later fragment into smaller ones, *e.g.* galaxies. This is the so-called it Top-down scenario. Neutrinos with non-zero mass, a HDM candidate within the standard model of particle physics, could in principle contribute significantly to the matter

content of the Universe. However, neutrino streaming results in very low density contrast on galactic scales, thus making galaxy formation nearly impossible [21].

On the other hand, one speaks of Cold Dark Matter (CDM), if the matter would consist of very massive particles. Unlike baryons that are frozen to the radiation field prior to recombination, these heavy particles could decouple from the cosmic fluid much earlier and be free to cluster as soon as they become non-relativistic. Thus initial density fluctuations show no damping by free streaming at physically relevant scales. In this picture the smallest structures, *e.g.* of sub-galactic size, form first driven by the CDM (*Bottom-up* scenario).

The outcome of these numerical simulations to study large scale structure formation strongly support models with a cosmological constant $\Lambda \neq 0$ and a large fraction of non-baryonic Cold Dark Matter [22]. Hot Dark Matter does not provide a good fit with observations, since essentially all small-scale structures corresponding to supercluster scale or below are wiped out.

1.3 Dark Matter candidates

As we have seen in the previous sections, the evidence for Dark Matter is compelling at all observed astrophysical scales. Nevertheless, very little about Dark Matter is known. In particular, the identity of the particle (or particles) which accounts for it remains a mystery. According to the collected experimental data, we can summarize our knowledge in four points:

1. Dark Matter must be essentially stable, or at least have a life time long compared to the present age of the Universe.
2. Dark Matter is predominantly non-baryonic in nature. This is supported by evidences from BBN and CMB, as described previously.
3. Dark Matter is slow-moving. More precisely, a Cold Dark Matter candidate must be non-relativistic throughout the formation of large scale structure.
4. Dark Matter is very weakly interacting. This is supported by upper limits on self-interaction from astrophysical observations, *e.g.* the *Bullet Cluster* (see after) and terrestrial searches.

There is a wide range of possible Dark Matter candidates. Their mass could be as small as that of axions with $m = 10^{-5}$ eV to black holes of mass $m = 10^4 M_{\odot}$ (about 75 orders of magnitude greater). At the highest masses there are historical candidates, which do not fit one of the conditions above. Baryonic candidates, for example, are MAAssive Compact Halo Objects (MACHOs) [23, 24, 25, 26] such as brown dwarfs (balls of H and He with masses below $0.08 M_{\odot}$), jupiters (masses near $0.001 M_{\odot}$), black hole remnants (masses near $100 M_{\odot}$) and neutron stars. But astronomical surveys for MACHOs (*e.g.* [27]) indicate that these objects cannot make up all the amount of Dark Matter that is needed in our galactic halo.

There is also the possibility that the Dark Matter problem could be explained by non-Newtonian gravity models, in which the strength of the gravitational force decreases less rapidly than r^{-2} at large distances. This idea is based on the fact that Newton's law has never been verified in the case where the acceleration is extremely

small, hence at the scale of galaxies, where the gravitational force is extremely small due to the very large distances. This theory of *MOdified Newtonian Dynamics* (MOND), first introduced by Mordehai Milgrom in 1983 [28], states that the simple equation $\vec{F} = m \vec{a}$ should be:

$$\vec{F} = m \mu(a/a_0) \vec{a} \quad (1.15)$$

with $\mu(x) = 1$ if $x \gg 1$ and $\mu(x) = x$ if $x \ll 1$.

However, gravitational lensing by the colliding galaxy clusters 1E0657-56 is a convincing dynamic system giving theory-independent proof of Dark Matter dominance at large scales [32]. It is made up of two subclusters in the process of merging, which appear to have passed directly through one another (see Fig. 1.6). The space between galaxies is large enough so that the galaxies in each subcluster have passed through the other subcluster without collisions. The intracluster medium (ICM), on the other hand, has been shocked and heated by the interactions, and remains concentrated closer to the collision point.

This sets the stage for a very beautiful test of the Dark Matter model: if the mass of the clusters is dominated by collisionless Dark Matter, then weak lensing will show two centers near the concentrations of galaxies. If, on the other hand, the mass is mainly in the ICM, with the high mass-to-light ratio of galaxies and clusters explained by modified gravity, then weak lensing should show one center, near the gas.

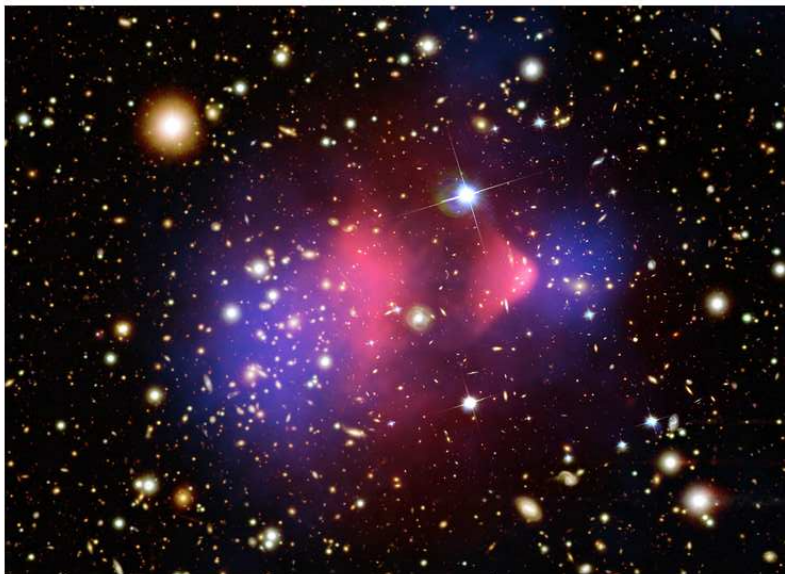


Figure 1.6. The galaxy cluster 1E 0657-56, also known as the *Bullet Cluster*. Hot gas detected by Chandra [29] in X-rays is seen as two pink clumps in the image and contains most of the baryonic matter in the two clusters. An optical image from Magellan [30] and the Hubble Space Telescope [31] shows the galaxies in orange and white. The blue component, the Dark Matter, is detected indirectly by the gravitational lensing of background objects.

When this system is studied and mapped with weak lensing, it shows that the lensing mass is concentrated in the two regions containing the galaxies, rather than in the two clouds of stripped gas which contain most of the baryonic mass and significantly separated from the highest intensity of X-rays [32, 33]. Weakly interacting Dark Matter would move together with the galaxies, and therefore explains the observed system. The bullet cluster of 1E0657-56 is not the unique example, more cases have been studied and all agree to a non-baryonic Cold Dark Matter [34, 35]. These observations present difficulties for alternative gravity theories.

In the following sections, we present some of the candidates discussed in the literature, focusing our attention especially on WIMPs (Sec. 1.3.3), the present most favourable Dark Matter candidate.

1.3.1 Light neutrinos

Within the Standard Model of particle physics, only one non-baryonic Dark Matter candidate is currently known to exist: the neutrino ν with non-zero mass as required by the experimentally well established phenomenon of neutrino oscillations (see Sec.3.1). Even though neutrinos are disfavoured as the dominant Dark Matter constituent because they damp small density fluctuations at the early Universe, their great abundance could contribute significantly to the total density. One can calculate the contribution of the neutrinos to the total density of the Universe Ω_ν as a function of their assumed masses m_{ν_i} (in fact, the sum of the three different neutrino species $\sum m_{\nu_i}$):

$$\Omega_\nu = \frac{8\pi G}{3H_0^2} n_\nu \sum m_{\nu_i} \quad (1.16)$$

with the number density n_ν of the present day neutrinos. The neutrinos decouple from other particles, *e.g.* electrons and photons, at a temperature $T \sim 1$ MeV when their reaction rate becomes less than the expansion rate of the Universe. Light neutrinos with $m_\nu < 1$ MeV are therefore still relativistic when they decouple (Hot Dark Matter) and their number density per flavour is linked to the photon density n_γ [19]:

$$n_\nu = \frac{3}{4} \cdot \frac{4}{11} \cdot n_\gamma = \frac{3}{4} \cdot \frac{4}{11} \cdot \frac{2\zeta(3)}{\pi^2} T^3 \simeq 113 \text{ cm}^{-3} \quad (1.17)$$

where $T = 2.725$ K is the CMB black body temperature, $\zeta(x)$ is the Riemann's zeta function, the factor $3/4$ comes from Fermi statistics and the factor $4/11$ is due to the rise of n_γ by e^+e^- annihilation. The total density contribution for a Dirac neutrino (or half of this for a Majorana neutrino) can then be written [36] as:

$$\Omega_\nu = \frac{\sum m_{\nu_i}}{93 \text{ eV}} h^{-2} . \quad (1.18)$$

Experimental results (that will be discussed in Sec. 3.2) limit the contribution of the neutrino masses to the total density of the Universe to an almost negligible magnitude. However, neutrinos may still play an important role as Dark Matter and for structure formation if they are a subdominant component of a Cold Dark Matter scenario. Leaving the fact that neither baryonic matter nor neutrinos can account for the full amount of Dark Matter needed in the Universe, a new yet unknown component ought to be postulated from cosmology. This coincides with extensions to the Standard Model of particle physics providing a natural solution to this problem, which will be discussed in the next sections.

1.3.2 Axions

The axion is a hypothetical elementary particle introduced to resolve the violation of the combined symmetries of charge conjugation and parity (CP violation) in quantum chromodynamics (QCD) as postulated by R. Peccei and H. Quinn [37]. CP violation, in fact, according to the Standard Model of particle physics, should produce a neutron electric moment 10 orders of magnitude larger than the current experimental lower limit of $10^{-28} e \text{ cm}$.

The Peccei-Quinn idea was to promote the violating CP term in QCD to a field (thus a particle). This can be accomplished by adding a new global symmetry (called *Peccei-Quinn symmetry*) to the Standard Model that becomes spontaneously broken. Once this symmetry is broken, a new particle results and naturally relaxes the CP violation to zero. This new particle is hence called the axion.

Explicit calculations of non-trivial QCD vacuum effects provide axion masses m_a in a wide range of $10^{-12} \text{ eV} \leq m_a \leq 10^6 \text{ eV}$ [38]. The axion is described by the spontaneous symmetry breaking scale of the Peccei-Quinn symmetry, f_a , and is related to the mass as

$$m_a \simeq 6 \mu\text{eV} \cdot \left(\frac{10^{12} \text{ GeV}}{f_a} \right) \quad (1.19)$$

while the axion-photon coupling $g_{a\gamma\gamma}$ is defined as

$$g_{a\gamma\gamma} = \frac{\alpha g_\gamma}{\pi f_a} \quad (1.20)$$

where α is the fine structure constant and g_γ is a dimensionless model dependent coupling parameter.

Axions may be created in the early Universe as a non-relativistic condensate [39]. The average axion relic density can be estimated as

$$\Omega_a h^2 \sim \left(\frac{f_a}{10^{12} \text{ GeV}} \right)^{7/6}. \quad (1.21)$$

The axion's couplings to matter are thought to be extremely small, however, its conversion into two photons can be stimulated with the help of a resonant cavity and a strong magnetic field. This conversion also determines the principle of detection. Several ongoing experiments, such as CAST (CERN Axion Solar Telescope) [40], ADMX (Axion Dark Matter eXperiment) [41] and PVLAS (Probing Vacuum with polarised Light) [42], are trying to detect axions, so far without conforming success. Together with astrophysical and cosmological constraints, *e.g.* considering effects of axions on the evolution of stars of all types the limit on the axion mass is set to $m_a \lesssim 10^{-2} \text{ eV}$ [11] with an allowed mass window of interest to Dark Matter of $\mu\text{eV} \lesssim m_a \lesssim \text{meV}$. Ongoing and future experiments are expected to probe the couplings of axions to various particles and set limits on the contribution of axions to the Dark Matter content of the Universe.

1.3.3 Weakly Interacting Massive Particles (WIMPs)

Although the composition of Dark Matter remains unknown, one natural candidate is a weakly interacting massive particle. The so-called WIMPs (generally denoted χ)

have several advantages. First of all, they arise naturally in many models, *e.g.* supersymmetric models. Moreover, they are “cold”, as required for structure formation, and they can be generated as a thermal relic of the Big Bang, with approximately the required density.

In the very early Universe, in fact, the particles χ were in thermal equilibrium since the temperature was much higher than their mass ($T \gg M_\chi$). The number density of these relativistic particles in the ideal gas approximation is $n_\chi \propto T^3$. They are rapidly converting to lighter particles and vice versa via processes like $\chi\bar{\chi} \leftrightarrow \bar{l}l$, where $\bar{l}l$ are quark-antiquark, lepton-antilepton pairs, Higgs and/or boson pairs, if the mass M_χ is larger than twice the masses of these particles. After the temperature of the Universe drops below M_χ , the number density exponentially falls ($n_\chi \propto e^{-M_\chi/T}$) and the annihilation rate of the WIMPs $\Gamma_\chi = \langle\sigma v\rangle n_\chi$ (σ is the thermal averaged total annihilation cross section, v is the relative velocity) becomes smaller than the expansion rate of the Universe, that is $\Gamma_\chi < H$. The annihilation of the particles then becomes inefficient and a relic abundance remains (they “freeze-out”). Quantitatively, using the Boltzmann equation one can determine the matter contribution of the WIMPs:

$$\Omega_\chi = \frac{8\pi G}{3H_0^2} M_\chi n_\chi \simeq \left(\frac{3 \times 10^{-27} \text{ cm}^3 \text{ s}^{-1}}{\langle\sigma v\rangle} \right) h^{-2}. \quad (1.22)$$

This approximation is independent of the WIMP-mass but is only determined by the total annihilation cross section. Fig.1.7 shows numerical solutions of the Boltzmann equation. The equilibrium (solid line) and actual (dashed lines) abundances per comoving volume are plotted as a function of $x = M_\chi/T$, which increases with increasing time. As the annihilation cross section is increased, the WIMPs stay in equilibrium longer and the relic abundance today is smaller.

Within the Standard Model of particle physics, a heavy neutrino could be an ideal candidate. But as described in the previous section, the experimental mass limits exclude them. A fourth generation heavy neutrino was a possibility until measurements of the Z_0 width showed that there are exactly three neutrino families [11]. Additionally a so-called “sterile” neutrino [43], a hypothetical neutrino that does not interact via any of the fundamental interactions but gravity is recently also experimentally disfavoured [44]. However, an extension to the Standard Model, called Supersymmetry (SUSY), predicts a doubling of the existing particle. This theory is motivated to solve the hierarchy problem of particle physics as well as to unify the electro-weak forces with gravity towards a Grand Unified Theory (GUT). The new symmetry relates elementary particles of one spin to another particle that differs by half a unit of spin and are known as superpartners. Since the spectrum of the Standard Model does not provide such particles, the symmetry must be broken to allow the superpartners to have different masses, in fact much higher masses and are therefore not yet discovered. Normal and supersymmetric particles acquire a new quantum number called R-parity:

$$R = (-1)^{3(B-L)+2S} \quad (1.23)$$

where B , L and S are the baryon, lepton and spin number operators respectively. When $R = 1$ this corresponds to ordinary particles, when $R = -1$ to the corresponding superpartners. If R-parity is broken, it means that there are no selection

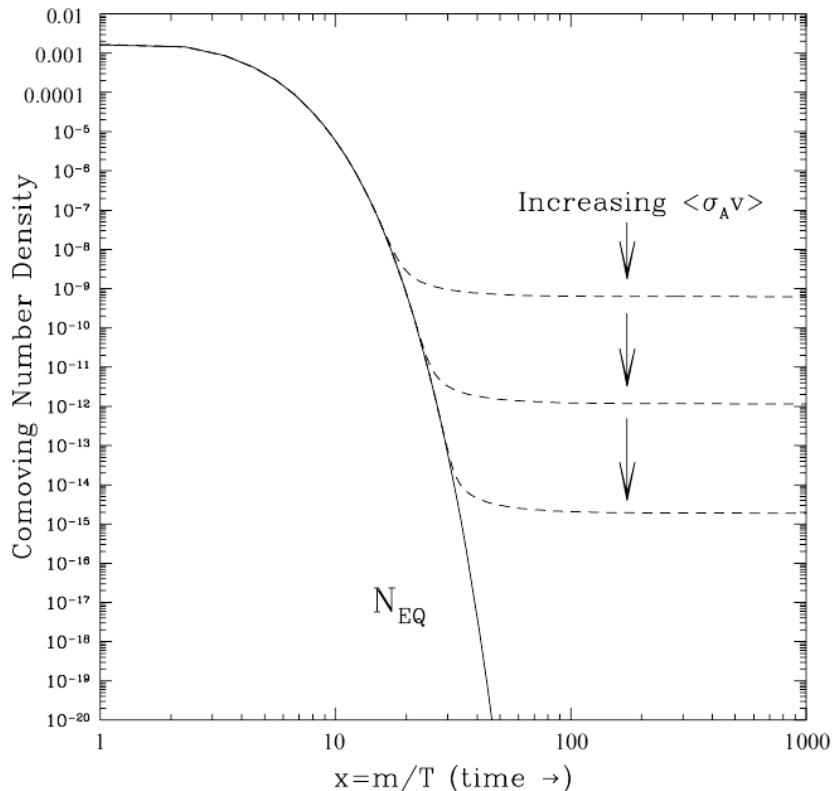


Figure 1.7. Evolution of the WIMP’s comoving number density as function of temperature (in units of the WIMP mass m) in the early Universe. The solid curve represents the equilibrium abundance, while the dashed lines correspond to actual abundances for various choices of velocity-weighted annihilation cross section. The temperature of the “freeze out” occurs when the reaction rate drops below the expansion rate. Figure from [36].

rules to prevent the decay of the supersymmetric particles in the spectrum with masses of order a few GeV or heavier. The scale of R-parity violation regulates the strength of baryon and lepton number violation processes, which have not been observed in nature so far and severe constraints on R-parity violation arise. If this R number is conserved, then a lightest supersymmetric particle (LSP) will have to be stable. A detailed theoretical description of the motivations for SUSY, the framework of supersymmetric Lagrangians and the concepts of the Minimal Supersymmetric Standard Model (MSSM) can be found in [45] and references therein. Assuming supersymmetric models with the LSP being the lightest mass eigenstate of a general superposition of neutral spin 1/2 fermions, namely the *photino* (the superpartner to the photon), the *zino* (the superpartner of the Z_0 boson) and the *higgsino* (the superpartner of the neutral Higgs boson), the so-called *neutralino* turns out to be an ideal Dark Matter candidate. The cosmic abundance of the neutralino would be determined by the freeze-out from thermal equilibrium (see Eq. 1.22) with their annihilation and scattering cross sections, as well as masses depending on specific parameters of the assumed supersymmetric model. Despite the strong theoretical motivation for supersymmetry, no convincing experimental evi-

dence for the existence of supersymmetric particles has been found until today. The search for supersymmetric particles, with masses proclaimed to be around the weak scale, is one of the prime goals of the next generation accelerators, most notably the Large Hadron Collider (LHC) at CERN, that started to operate in 2009. Until these results, the cosmological need for a suitable CDM candidate is the strongest empirical hint to supersymmetry, with stringent limits on the neutralino mass and interaction cross sections from the non-observation at present accelerators.

Beyond the discussed neutralino, there are other particle Dark Matter candidates, which currently seem almost impossible to detect and which are beyond the scope of this work. For instance, the gravitino, the spin $3/2$ superpartner of the graviton, the mediator particle of gravity states from the “hidden sector” and thought responsible for supersymmetry breaking, can be a stable particle with masses in the TeV range. This would be the case, if the gravitino is the LSP of R-parity conserving supersymmetric models. Another candidate is the axino, the spin $1/2$ superpartner of the axion (which was discussed in the previous section). For more details on supersymmetric candidates and the current experimental limits to them, see [46] and references therein.

Chapter 2

Dark Matter detection

In the previous chapter we have introduced the subject of Dark Matter and the strong evidence in favour of its existence. The problem of Dark Matter is still one of the biggest remaining mysteries in modern physics and one should not be surprised of the huge experimental effort made in this field. If weakly interacting massive particles really populate our galactic halo there is a reasonable hope that they could be directly or indirectly detected with suitable experiments on earth or in space. Nevertheless one must emphasize that the detection of Dark Matter particles will not be sufficient to conclusively identify the nature of Dark Matter, since it is highly unlikely to provide enough informations to reveal the underlying physics (*e.g.* supersymmetry). In contrast, experiments at the modern colliders may identify a long-lived weakly interacting particle, but will not be able to test its cosmological stability or abundance. Only by combining the informations provided by many different experimental approaches, the mystery of Dark Matter particle nature will be solved. In this chapter, after a brief description of the possible experimental strategies for Dark Matter search, we will focus on the direct detection approach. In particular, the calculation of the expected WIMP rate in a detector and its annual modulation will be discussed. At the end of the chapter a short overview on the status of the research in this field and the latest results will be given.

2.1 Direct vs indirect detection

The attempts to detect WIMP Dark Matter proceed along two separate experimental ways: indirect detection and direct detection.

The indirect searches aim to the detection of WIMP through the observation of their annihilation products. This can happen, for example, if the WIMP is the neutralino, which is a Majorana particle and therefore it is the anti-particle of itself. The annihilation of two neutralinos can occur in the galactic halo or inside astrophysical objects like the Sun or the Earth, where it should be enhanced because of the accumulation of WIMPs due to gravity.

When WIMPs annihilate, they can produce quarks, leptons, gauge bosons, Higgs bosons and gluons. One of the most favorable experimental channels is the search for positrons. The origin of positrons comes when heavier particles either decay and/or hadronize. WIMP annihilation is then expected to produce an equal mixture of electrons and positrons, but this raises the generally low electron-positron

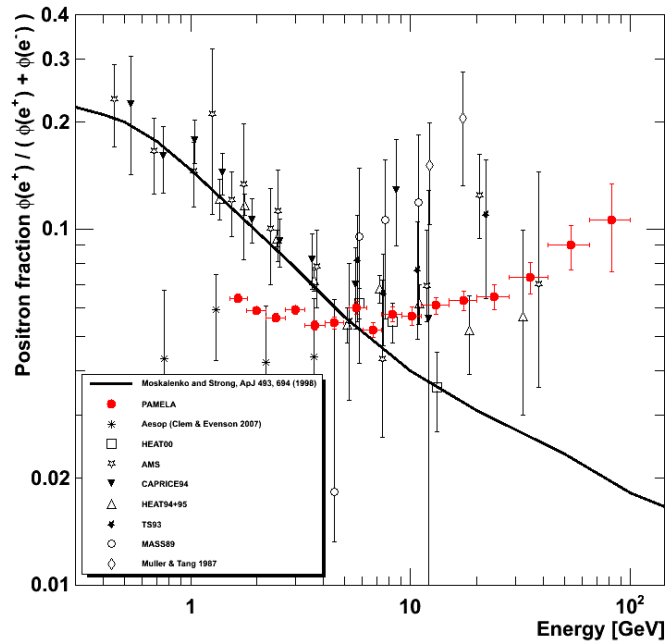


Figure 2.1. PAMELA positron fraction compared to other experimental data and theoretical calculations by Moskalenko and Strong [52]. Figure adapted from [53].

ratio from more trivial background processes. Therefore WIMP annihilation should appear as a broad excess of high-energy positrons, inconsistent with the declining power laws expected from background processes. In the last years, multiple experiments' results have been interpreted as possible products of WIMPs. For example, the PAMELA experiment, which began its three-year satellite mission in June of 2006, reported an anomalous rise in the cosmic ray positron fraction (the positron to positron-plus-electron ratio) above 10 GeV (see Fig. 2.1), confirming earlier indications from HEAT [47] and AMS-01 [48]. The observation by PAMELA of this rising positron fraction up to 100 GeV, further complemented with the ATIC [49], Fermi [50], HESS [51] data on the electron-positron spectrum up to a few TeV, has led to significant adjustments in the understanding of the local high energy electron-positron budget. The search for antimatter anomalous fluxes will be improved by AMS-02 [54] that, combining searches in different channels (antiprotons, positrons, anti deuterons, gamma rays) could have higher sensitivity to WIMP annihilation signals.

Additional informations can be obtained by muon neutrinos, that can be produced by annihilation of neutralinos trapped inside the Sun or the Earth. Neutrinos, like gamma rays, keep their original direction and for this reason they are now one of the most promising hopes for indirect detection methods in present and future neutrino telescopes. For example, the SuperKamiokande neutrino detector [55], the IceCube experiment [56] or the ANTARES neutrino telescope [57] can set limits on the rate of WIMP annihilations in the Sun.

Direct searches for WIMPs are carried on in low-background underground experiments, where the direct signal of a WIMP interaction with the target nucleus

is detected. This signal is given by the nucleus recoiling after the WIMP elastic scattering. As we will see, the energy spectrum of the recoils increases roughly exponentially towards low energies and extends up to several tens keV. Its shape depends on the WIMP mass, the mass of the target nucleus and the WIMP velocity distribution.

2.2 WIMP rate in a detector

The differential rate per unit mass of elastic nuclear recoils is expected to be featureless and smoothly decreasing, with the typical form [58]:

$$\frac{dR}{dE_R} = \frac{R_0}{E_0 r} e^{-E_R/E_0 r} \quad (2.1)$$

where E_R is the recoil energy, R_0 is the total event rate, E_0 is the most probable incident kinetic energy of WIMP of mass M_χ and $r = 4M_\chi M_A / (M_\chi + M_A)^2$ is a kinematic factor for a target nucleus of mass M_A . This equation represents the simplest case of a detector stationary in the Galaxy. In practice Eq. (2.1) is considerably more complicated due to several corrections:

- The total rate depends on the wimp-nucleon coupling. Results will be different for spin-dependent and spin-independent interactions.
- The target consists of more than one element.
- The detector is not stationary in the Galaxy. It is on the Earth, orbiting around the Sun, moving through the Galaxy with a velocity $v_E \simeq 230$ km/s.
- A nuclear form factor correction must be also taken into account, owing to the nucleus finite size and depending mostly on nuclear radius and recoil energy.
- In most of the detectors, only a fraction of the whole recoil energy is detected. True recoil energy differs from the observed one by a quenching factor $f_n \leq 1$ depending on target material and detection strategy.

2.2.1 Particle density and velocity distribution

Differential WIMP density is given by

$$dn = \frac{n_0}{k} f(\mathbf{v}, \mathbf{v}_E) d^3v \quad (2.2)$$

where

$$k = \int_0^{2\pi} d\phi \int_{-1}^{+1} d(\cos\theta) \int_0^{v_{esc}} f(\mathbf{v}, \mathbf{v}_E) v^2 dv \quad (2.3)$$

is the normalization constant. Here $n_0 = \rho_\chi / M_\chi$ is the mean WIMP number density for Dark Matter density ρ_χ (standard value is $0.3 \text{ GeVc}^{-2} \text{ cm}^{-3}$), \mathbf{v} is the WIMP velocity relative to the Earth, \mathbf{v}_E represents Earth velocity relative to the Galaxy, v_{esc} is the local Galactic escape velocity (typical value is 600 km/s) and dn is the particle density of Dark Matter with relative velocities within d^3v about \mathbf{v} . Assuming a Maxwellian Dark Matter velocity distribution with average $v_0 = 220$ km/s

$$f(\mathbf{v}, \mathbf{v}_E) = e^{-|\mathbf{v} + \mathbf{v}_E|^2 / v_0^2}, \quad (2.4)$$

we obtain, using $v_E \simeq v_0$,

$$k = k_1 = k_0 \left[\operatorname{erf} \left(\frac{v_{esc}}{v_0} \right) - \frac{2}{\pi^{1/2}} \frac{v_{esc}}{v_0} e^{-v_{esc}^2/v_0^2} \right], \quad (2.5)$$

where $k_0 = (\pi v_0^2)^{3/2}$ is the normalization in case of $v_{esc} = \infty$.

2.2.2 Differential rate

The event rate per unit mass on a target of atomic number A is

$$dR = \frac{N_0}{A} \sigma_A v dn \quad (2.6)$$

where N_0 is the Avogadro number ($6.02 \cdot 10^{26} \text{ kg}^{-1}$) and σ_A is the ‘‘zero momentum transfer’’ cross-section per nucleus. In the case of spin-independent interaction, this cross-section can be easily obtained as

$$\sigma_A = \sigma_0 \frac{\mu_A^2}{\mu_n^2} A^2 \quad (2.7)$$

where σ_0 is the WIMP-nucleon cross-section, $\mu_A = M_A M_\chi / (M_A + M_\chi)$ is the reduced mass of the system ‘‘WIMP-nucleus’’ and μ_n is the reduced mass of the system ‘‘WIMP-nucleon’’. Then:

$$R = \frac{N_0}{A} \sigma_A \int v dn = \frac{N_0}{A} \sigma_A n_0 \langle v \rangle \quad (2.8)$$

We define R_0 as the event rate per unit mass for $v_E = 0$ and $v_{esc} = \infty$:

$$R_0 = \frac{2}{\pi^{1/2}} \frac{N_0}{A} \frac{\rho_\chi}{M_\chi} \sigma_A v_0 \quad (2.9)$$

Substituting Eqns. (2.2,2.9) in Eq. (2.8), we obtain

$$R = R_0 \frac{\pi^{1/2}}{2} \frac{\langle v \rangle}{v_0} = R_0 \frac{k_0}{k} \frac{1}{2\pi v_0^4} \int v f(\mathbf{v}, \mathbf{v}_E) d^3 v \quad (2.10)$$

and the differential form

$$dR = R_0 \frac{k_0}{k} \frac{1}{2\pi v_0^4} v f(\mathbf{v}, \mathbf{v}_E) d^3 v. \quad (2.11)$$

The recoil energy of a nucleus struck by a WIMP of kinetic energy $E = \frac{1}{2} M_\chi v^2$, scattered in centre-of-mass at angle θ ,

$$E_R = E r (1 - \cos\theta)/2 \quad (2.12)$$

where

$$r = \frac{4M_\chi M_A}{(M_\chi + M_A)^2}. \quad (2.13)$$

Assuming the scattering isotropic, the recoils are uniformly distributed in E_R over the range $0 \leq E_R \leq E_r$. Thus

$$\frac{dR}{dE_R} = \int_{E_{min}}^{E_{max}} \frac{1}{E_r} dR(E) = \frac{1}{E_0 r} \int_{v_{min}}^{v_{max}} \frac{v_0^2}{v^2} dR(v), \quad (2.14)$$

where we define $E_0 = \frac{1}{2} M_\chi v_0^2 = (v_0^2/v^2)E$, while $E_{min} = E_R/r$ is the smallest particle energy which can give a recoil energy of E_R and v_{min} is the Dark Matter particle velocity corresponding to E_{min} , *i.e.*

$$v_{min} = \left(\frac{2E_{min}}{M_\chi} \right)^{1/2} = v_0 \left(\frac{E_R}{E_0 r} \right)^{1/2}. \quad (2.15)$$

Substituting into Eq. (2.11), we obtain

$$\frac{dR}{dE_R} = \frac{R_0}{E_0 r} \frac{k_0}{k} \frac{1}{2\pi v_0^2} \int_{v_{min}}^{v_{max}} \frac{1}{v} f(\mathbf{v}, \mathbf{v}_E) d^3v \quad (2.16)$$

that, with non-zero v_E and finite $v_{max} = v_{esc}$, gives

$$\frac{dR}{dE_R} = \frac{k_0}{k_1} \frac{R_0}{E_0 r} \left\{ \frac{\pi^{1/2}}{4} \frac{v_0}{v_E} \left[\text{erf} \left(\frac{v_{min} + v_E}{v_0} \right) - \text{erf} \left(\frac{v_{min} - v_E}{v_0} \right) \right] - e^{-v_{esc}^2/v_0^2} \right\}. \quad (2.17)$$

2.2.3 Scalar and axial-vector interactions

In the above equations we have considered only the spin independent scattering. Nevertheless, the interactions between nuclei and WIMP can be of two types, depending on the WIMP-quark coupling:

- scalar or spin-independent interaction (SI): happens through the exchange of a squark or a Higgs and can be very important, especially for heavier nuclei
- axial-vector or spin-dependent interaction (SD): happens through the exchange of a squark or a Z boson

The theoretical calculations leading to the WIMP-nucleus cross-section from the WIMP-quark coupling will not be discussed here. The total WIMP-nucleus elastic cross section for an element with mass number A can be written as:

$$\sigma_A = \sigma_{A,SI} + \sigma_{A,SD} \quad (2.18)$$

While the spin-independent cross section is proportional to $\mu_A^2 A^2$ (as can be seen in Eq. 2.7), the spin-dependent cross section is proportional to $\mu_A^2 I_s$ [59]. The factor I_s has the form

$$I_s = (a_p \langle S_p \rangle + a_n \langle S_n \rangle)^2 J(J+1), \quad (2.19)$$

where a_p and a_n are the effective WIMP-nucleon couplings, $\langle S_p \rangle$ and $\langle S_n \rangle$ are the expectation values of the proton and neutron spins within the nucleus and J is the total nuclear spin. Only nuclei with non-zero J can have SD interactions.

2.2.4 Nuclear form factor correction

So far, we have neglected the dependence on the momentum transfer ($q = \sqrt{2M_A E_R}$). When the wavelength \hbar/q is no longer large compared to the nuclear radius, the cross-section decreases with increasing q . It is useful to introduce a “nuclear form factor” F , function of the dimensionless quantity qr_n (using units in which $\hbar = 1$), where r_n is the effective nuclear radius. Cross-sections then behave as

$$\sigma(qr_n) = \sigma_0 F^2(qr_n), \quad (2.20)$$

considering the two different cases of SI and SD interactions. Several multi-parameter fits to charge density have been proposed to calculate SI $F(qr_n)$. Among them, the distribution proposed by Helm [60] has the advantage of yielding an analytic form factor expression:

$$F(qr_n) = 3 \frac{j_1(qr_n)}{qr_n} e^{-\frac{(qs)^2}{2}} \quad (2.21)$$

where $s \simeq 0.9$ fm is a measure of the nuclear thickness and j_1 is the Bessel function:

$$j_1(qr_n) = \frac{\sin(qr_n) - qr_n \cos(qr_n)}{(qr_n)^2}. \quad (2.22)$$

Nuclear radius can be approximated by equation:

$$r_n^2 = c^2 + \frac{7}{3}\pi^2 a^2 - 5s^2, \quad (2.23)$$

where $a \simeq 0.52$ fm and $c \simeq (1.23A^{1/3} - 0.60)$ fm. In Fig. 2.2 are reported the obtained form factors for some typical nuclei.

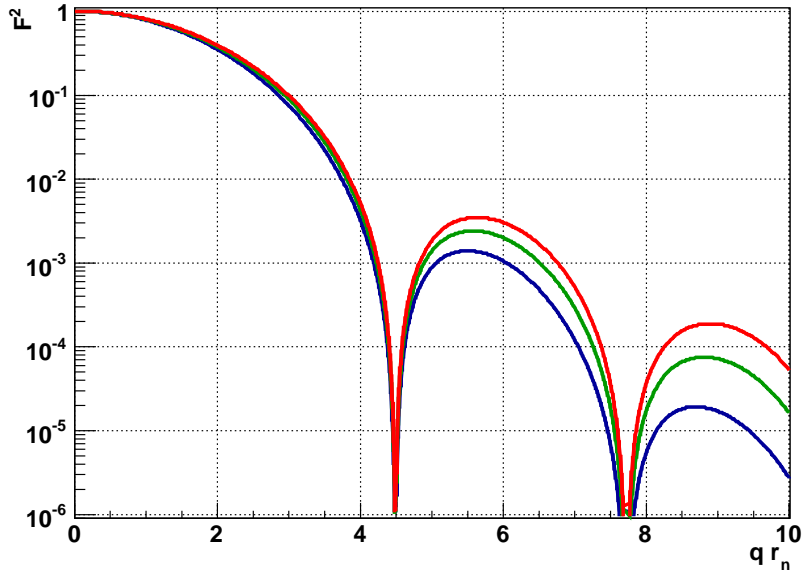


Figure 2.2. Spin-independent nuclear form factors for ^{131}Xe (in red), for ^{40}Ar (in blue) and for ^{73}Ge (in green).

In the case of spin-dependent interactions, a useful approximation is to consider only the contribution coming from the unpaired nucleon (“single particle model”) or from nucleons of the same type as the unpaired nucleon (“odd-group model”). In this case the form factor can be written:

$$F(qr_n) = j_0(qr_n) = \frac{\sin(qr_n)}{qr_n}. \quad (2.24)$$

More precise calculations have been carried out for a small number of nuclei (for example see [61] and [62]).

2.2.5 Quenching factor

The signal induced by a given nuclear recoil energy is usually less than the signal produced by an electron recoil of the same energy. This is due to the different energy percentages going to detectable channels (*i.e.* light or electric charge, for example) and to undetectable ones (for example heat). The ratio f_n between observed energy and true energy is named quenching factor and can be determined by neutron scattering measurements. While this additional calibration factor could be incorporated to yield observed spectra directly in terms of E_R , working with the γ -calibrated energies for easy identification of γ background is usually preferred. Consequently E_R in the above formulas should be replaced by the “visible” energy E_v , using $E_R = E_v/f_n$ and, considering possible variations of f_n with E_R ,

$$\frac{dR}{dE_R} = f_n \left(1 + \frac{E_R}{f_n} \frac{df_n}{dE_R} \right) \frac{dR}{dE_v}. \quad (2.25)$$

2.2.6 Combining results

All the equations above are strongly dependent on mass number A . Since detectors are often composed by several different materials, one has to consider the different contribution of each of them. The total differential recoil rate per kg of target mass can be obtained by

$$\left. \frac{dR}{dE_R} \right|_{total} = \sum_A x_A F_A^2 \left. \frac{dR}{dE_R} \right|_A \quad (2.26)$$

where F_A^2 is the nuclear form factor for a target nucleus with mass number A , $dR/dE_R|_A$ its differential rate calculated in Eq. (2.17) and x_A its fraction of the total target mass.

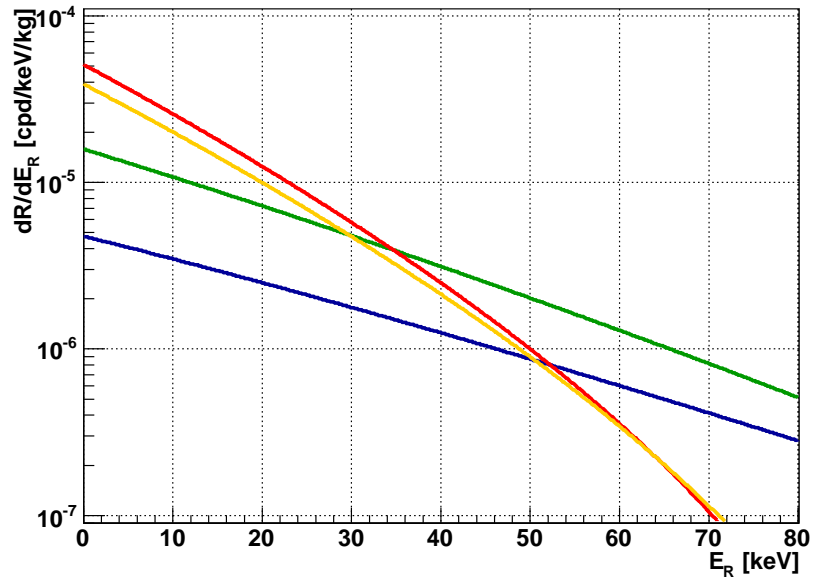
For example, TeO₂ bolometers (that will be introduced in Sec. 3.3) are composed by several different Te isotopes and ¹⁶O atoms (see Tab. (2.1)), with $f_n \simeq 1$ since in bolometers the whole energy is converted into phonons and fully detected [63]. Moreover, spin-dependent interactions in TeO₂ are negligible since it is composed almost exclusively by spin-0 nuclei and, even for the small non-zero spin isotopes, scalar cross sections are favoured by the high mass number. The obtained TeO₂ spectral function is shown in Fig. 2.3.

2.3 The annual modulation

It is important to stress that only few experiments are able to distinguish nuclear recoils from other background events, exploiting the different interaction features of

Table 2.1. Composition of a TeO₂ bolometer. Data from [64].

Isotope	A	Natural abundance in Tellurium	TeO ₂ mass fraction (x_A)
¹²⁰ Te	120	0.0009	0.0008
¹²² Te	122	0.0255	0.0204
¹²³ Te	123	0.0089	0.0071
¹²⁴ Te	124	0.0474	0.0379
¹²⁵ Te	125	0.0707	0.0565
¹²⁶ Te	126	0.1884	0.1506
¹²⁸ Te	128	0.3174	0.2538
¹³⁰ Te	130	0.3408	0.2725
¹⁶ O	16		0.2004

**Figure 2.3.** Differential rate of WIMP spin-independent elastic scattering on TeO₂ (in yellow), on ¹³¹Xe (in red), on ⁴⁰Ar (in blue) and on ⁷³Ge (in green), for $M_\chi = 100$ GeV and $\sigma_0 = 10^{-45}$ cm².

the various particles in the detector. Without this capability, direct Dark Matter searches become more complex.

In fact, the energy spectrum of WIMP-induced nuclear recoils, that can be calculated using the above formulas, is exponentially decreasing with the recoil energy in the typical range $1 \div 100$ keV and, unfortunately, its shape is smooth and featureless. The absence of any feature in the spectrum and the low energy region where it is confined makes it practically impossible to distinguish this signal from the low-energy background of the detector, which comes partially from intrinsic sources (radioactive contaminations inside the detector itself or in the nearby material) and partially from external sources like cosmic rays and neutrons entering the detector area. It is clear now that it's impossible to detect a "positive" WIMP signal just by looking at the shape of the experimental spectrum. However, the absence of a positive signal does not mean no result at all: every experiment, providing an observation of nuclear recoils at low-energy, can set limits on the WIMP presence in our Galaxy, excluding those WIMPs that would produce a nuclear recoil event-rate higher than observed. Moreover, a reduction of the background, obtained for example working in an underground site or using background suppression or discrimination methods, increases the sensitivity of the detector and allows the experiment to set more and more stringent limits to the WIMP parameters.

Saying that the WIMP-induced nuclear recoil spectrum has no distinctive features is true for the shape of the spectrum but not for the WIMP signal in general. The recoil spectrum produced by WIMP-nucleus scattering in a target detector is expected to show the so-called annual modulation effect [65]. Since Earth rotates around the Sun and the Sun itself moves into the galactic reference frame (see Fig. 2.4(a)), we can express the Earth's speed with respect to the Galaxy (v_E) as the sum of the two motions:

$$v_E = v_{\odot} + \langle v_{rot} \rangle \cos\gamma \cos(\omega(t - t_0)) \quad (2.27)$$

where v_{\odot} is the average Earth's speed in its motion around the Sun and γ is the angle between the Earth's rotation plane and the galactic plane. The period and phase of the cosine function are known to be $\omega = 2\pi/T$ ($T = 1$ year) and $t_0 = 2^{nd}$ June. It is customary to express the Earth's velocity in units of the parameter v_0 , defined above as the parameter of the Maxwellian WIMP speeds distribution function. The adimensional quantity $\eta = v_E/v_0$ shows the following time-dependence:

$$\eta(t) = \eta_0 + \Delta\eta \cos(\omega(t - t_0)) \quad (2.28)$$

where the amplitude of the annual-modulated component ($\Delta\eta \simeq 0.07$) is small compared to the average value $\eta_0 \simeq 1.05$. In this framework, the expected WIMP signal in the Earth reference system can be written (first order Taylor approximation):

$$S = S_0 + S_m \cos(\omega(t - t_0)) \quad (2.29)$$

where $S_0 = S[\eta_0]$ is the time-independent signal and $S_m = \left. \frac{\partial S}{\partial \eta} \right|_{\eta_0} \Delta\eta$ is the amplitude of the modulated signal. As we can see from the expressions of S_0 and S_m and from Fig. 2.4(b), the amplitude of the annual modulation is only a few percent of the time-independent signal, strongly dependent on M_χ and E_R . Moreover, its contribution to the total signal S can be not only positive but also negative or zero. To

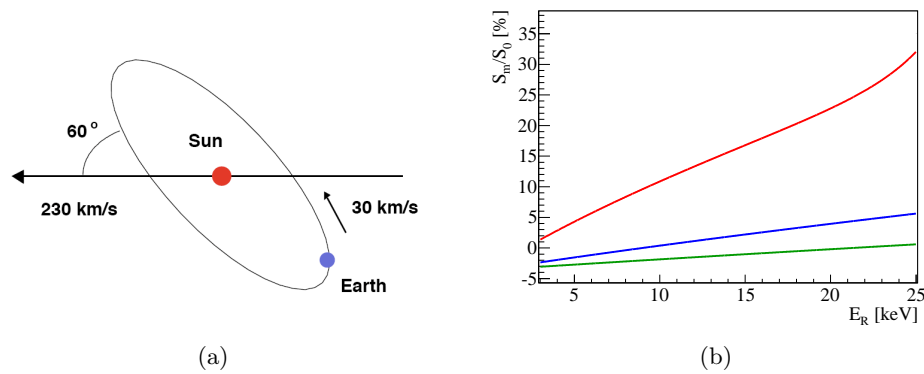


Figure 2.4. Left: The combined motion of the Earth around the Sun (average velocity $\langle v_{rot} \rangle = 30$ km/s) and of the Sun itself with respect to the Galaxy ($v_{\odot} = 232$ km/s) is responsible for the annual modulation effect. Right: Predicted ratio of the modulated to the constant WIMP signal in TeO_2 for $M_{\chi} = 20$ GeV in red, $M_{\chi} = 50$ GeV in blue and $M_{\chi} = 100$ GeV in green.

point out the presence of such fluctuation, superimposed on a constant count-rate of WIMP interactions but also background from other sources, is not an easy task. What is needed is a large mass detector, with a background well stable over time and high exposure time.

Despite the difficulties related with its detection, the annual modulation effect remains the main signature of a possible Dark Matter signal, a positive indication that, if observed, would allow to constrain the WIMP parameters space with an allowed region instead of several exclusion plots. It is important to point out that two different analysis can be performed in this case: a model-independent analysis, in which only the presence of the modulation is looked for in the data and a model-dependent analysis, where, assuming a complete model framework, one allows (or excludes) a region in the space of the parameters M_{χ} and σ . Therefore, if a modulation signature is discovered in the experimental data, it is possible to extract informations on the WIMP relevant quantities only in the framework of a given model (for example: spin-independent WIMP-nucleon interactions, non-rotating halo, Maxwellian distribution of WIMP velocity, Galactic escape velocity and so on).

2.4 WIMP detection techniques

A variety of techniques are presently in use for WIMP searches. Due to the numerous ways to achieve sensitivities to the WIMP properties (*e.g.* high A , high target mass, low threshold, low background, background-rejection and background-subtraction techniques, etc.), only a few, among those the most successful and most promising ones, are discussed in this section. One of the main difficulties of any such technique is the low signal rate to be expected from supersymmetric model calculations. The typical counting rates are much lower than the usual radioactive backgrounds. Therefore, common to all WIMP searches is the goal to reduce the natural radioactive contamination by using extremely pure substances and to actively reject background events by special techniques.

Experimentally, there are several ways of particular importance to measure the

event rate of WIMP-nucleus collisions discussed previously. First, one may search for scintillation light created by the energy deposit of the WIMP in the target detector, *e.g.* NaI or Xe detectors. Hereby, the recoiling particle directly or indirectly excites electrons to energy levels above their ground states, from which they may decay by emission of ultraviolet or visible photons. Due to the reasonably low backgrounds, by using ultrapure materials, and large masses achievable, scintillators are naturally used for annual-modulation searches. This has been successfully done by DAMA/NaI and DAMA/LIBRA experiments [66] at Laboratori Nazionali del Gran Sasso (Italy), which claims to have found an annual modulation on data taken over thirteen annual cycles. With the measured effect, the collaboration obtains a model independent evidence for the presence of a Dark Matter particle component in the galactic halo at 8.2σ C.L. (see Fig. 2.5). However, the deduced value for the WIMP-mass and the WIMP-nucleon cross section (see Fig. 2.6) remains the only claimed direct observation of WIMPs. No other experiment could yet confirm the observed signal. Moreover, the complete allowed parameter region by the DAMA evidence is excluded by many other experiments. Without regard to the exception of annual modulation, the described detection technology offers little or no direct background rejection capability. An important background rejection technique possible with many detectors is nuclear-recoil discrimination. In NaI scintillators, this can be achieved by pulse shape, since nuclear recoils yield more quickly decaying scintillation pulses than electron recoils.

Liquid noble gas detectors with scintillation readout have shown recently competitive WIMP sensitivities. Most notably has been liquid xenon (LXe), started by the DAMA/LXe experiment [68], but also liquid neon and liquid argon in the DEAP/CLEAN experiments [69]. Liquid argon is also used in the WARP collaboration [70]. Furthermore, argon is also used for the ArDM experiment [71], presently

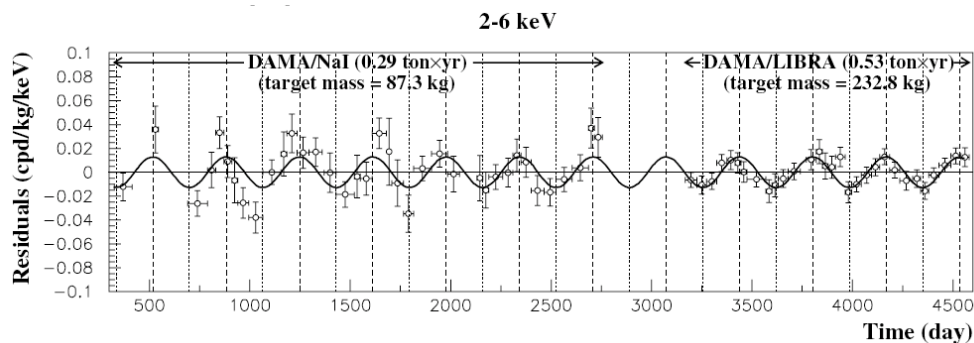


Figure 2.5. Experimental model-independent residual rate of the single-hit scintillation events, measured by DAMA/NaI and DAMA/LIBRA in the (2 - 6) keV energy interval as a function of the time. The zero of the time scale is January 1st of the first year of data taking of DAMA/NaI. The experimental points present the errors as vertical bars and the associated time bin width as horizontal bars. The superimposed curve is the cosinusoidal function behavior with a period $T = 1$ y, with a phase $t_0 = 152.5$ d (June 2nd) and with modulation amplitude equal to the central value obtained by best fit over the whole data, that is (0.0129 ± 0.0016) cpd/kg/keV. The dashed vertical lines correspond to the expected maximum of the signal (June 2nd), while the dotted vertical lines correspond to the expected minimum. The total exposure is $0.82 \text{ ton} \times \text{y}$ [66].

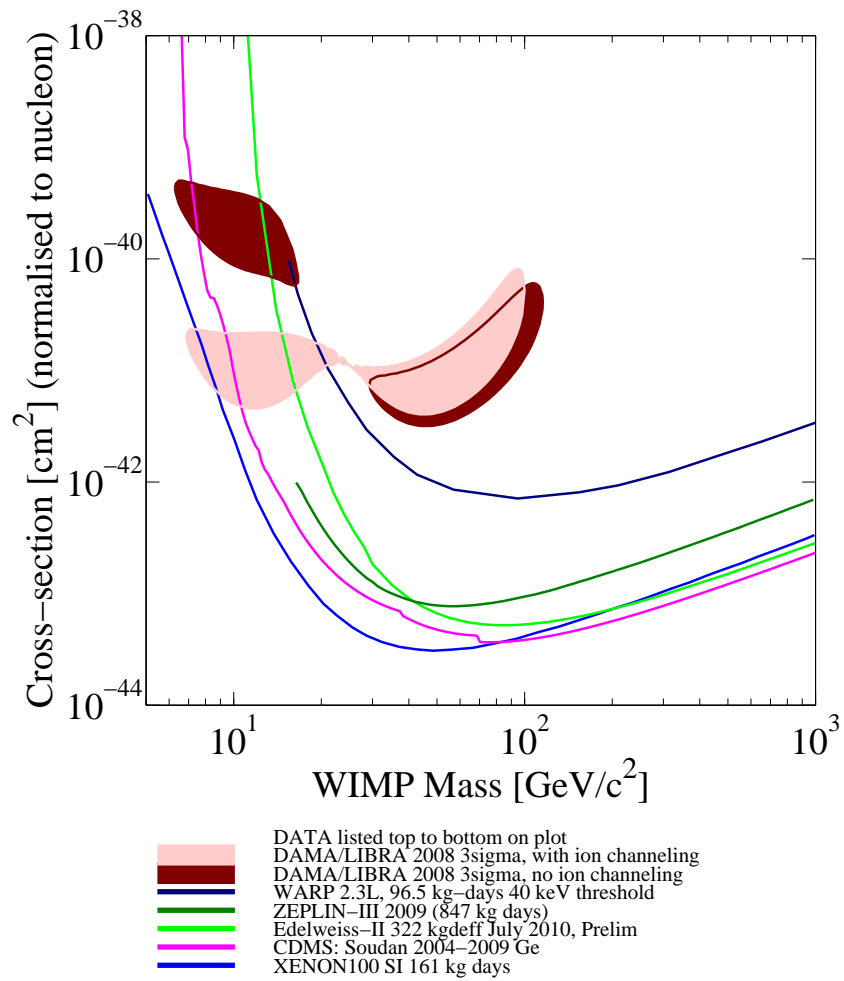


Figure 2.6. Current limits from various direct Dark Matter search experiments in the WIMP mass - WIMP-nucleon cross section (normalized to nucleon) plane. Figure is generated using [67].

under construction and commissioning on surface at CERN, aiming towards one ton two-phase liquid argon detector. LXe as a target for WIMP detection, on the other hand, has particularly good intrinsic properties, *e.g.* high mass, high scintillation and ionization efficiency and high radiopurity. However, the recoil discrimination achievable is of greater importance. This is realized firstly, as in NaI scintillators, by pulse shape analysis of the scintillation light, which is the basis of single-phase LXe experiments such as XMASS [72] in Japan and UK-based ZEPLIN-I [73]. More powerful discrimination in LXe can be achieved by recording also the ionization produced by the WIMP-interaction. The recoiling nucleus travels through the target material before stopping, ionizing atoms as it passes. The lower velocities of nuclear recoils though, induce less ionization relative to the ionization induced by electromagnetic interactions with electrons of the shell by β and γ radiation. This helps to significantly lower the background rate for Dark Matter searches. In liquid noble gas detectors this yields to a different ionization/scintillation ratio for nuclear and electron recoils, respectively. This detection principle is implemented by the ZEPLIN-II/III/IV [74, 75, 76], the XENON 10/100/1T [77, 78, 79] and the LUX [80] experiments. To obtain stable operation conditions the current experiments use two-phase LXe. Hereby, the charge produced by the recoil first drifts out of the liquid into a gaseous phase, where a proportional scintillation signal (electroluminescence) can be observed.

Another way to detect WIMP-nucleus collisions in a target detector is to search for the ionization signal in a semiconductor, notably in high-purity Germanium detectors. These detectors were initially used to look for the neutrinoless double beta decay of an isotope in the detector itself (see Sec. 3.1.3 and Sec. 3.2). The main problem of those detectors is the large background rate from natural radioactivity. However, the best limits have been achieved by the Heidelberg-Moscow and IGEX experiments [81, 82]. Next generation experiments aim at a further reduction in activity and are currently being built, *e.g.* the GERDA [83] and MAJORANA [84] experiments, all primarily aimed at neutrinoless double beta decays. A further possibility to search for the energy deposition by a WIMP-nucleus scattering is the “cryogenic” or “bolometric” approach. Whereby one may cool the target to very low temperatures of around 10 mK, so that a 10 keV energy deposit causes a measurable proportional increase in the detector temperature (see Ch. 4 for details). This heating can be measured *e.g.* by a superconducting thermometer attached to the target which is shifted toward the normal conducting phase by the temperature increase. The initial prospect of detectors of this type was to obtain very low recoil energy thresholds combined with a very high energy resolution. However, it was soon demonstrated that a simultaneous measurement of the ionization signal, together with the heat or phonon signal, also provides a good discrimination against electron recoils. In fact, a recoiling nucleus produces proportionally less ionization than an electron recoil of the same energy. Experiments using the hybrid technique of simultaneous ionization and heat collection are the EDELWEISS experiment [85], as well as for example the CDMS II experiment [86]. The latest sensitivity limits on the WIMP mass and WIMP-nucleon cross section of these experiments is also shown in Fig. 2.6. As an alternative, the CRESST collaboration [87] has developed cryogenic CaWO_4 phonon detectors and pursued the use of scintillation for the second signal channel, next to the heat signal. In particular, instead of using photomultipliers to obtain the scintillation signal, a second phonon-mediated de-

tector with a light absorber is placed adjacent to the primary detector. A similar approach with scintillating sapphire bolometers is undertaken by the ROSEBUD collaboration [88].

Besides the well established techniques discussed in this section, further approaches to detect Dark Matter directly are investigated. One promising technique uses superheated droplets detectors or “bubble detectors”. The goal of these detectors is to detect single bubbles induced by nuclear recoils in heavy liquid bubble chambers. In this implementation of the method, the metastable state of the target liquid is preserved by dispersing it into a viscous/inmiscible gel, effectively resulting in a collection of mini-bubble chambers. The great advantage of this technique, besides the low costs, the room temperature operation and the well known detector technology is the nuclear recoil discrimination power. The energy deposition by an electron recoil is too distributed to cause a bubble to boil, contrary to nuclear recoils. Among the experiments exploiting this technique, there are SIMPLE [89], PICASSO [90] and COUPP [91].

Finally, a powerful, though technologically challenging possibility to proof that a signal is of galactic origin is to correlate events with the Earth’s motion through the galactic WIMP halo. So, the goal is to measure the direction of the recoiling particle and to make use of the diurnal modulation of the signal due to directionality of the “WIMP wind”. This is the motivation behind the DMTPC experiment [92].

Chapter 3

TeO₂ bolometric detectors for 0 ν DBD search

In 1914 Chadwick observed that the electrons emitted in β decays have a continuous spectrum, unlike what happens in α and γ decays. Nevertheless, if the decay products were only an electron and a nucleus, electrons would have necessarily a monochromatic spectrum. To overcome this paradox, Pauli proposed a “desperate way out” to save energy conservation, introducing a new particle that was not detected in the decay, the “neutron”. After that the true neutron was identified by Chadwick, the new particle was renamed by Fermi “neutrino” (ν).

Electron neutrinos were detected for the first time by Cowan and Reines in 1956 and found to be left-handed in 1957. The muon neutrino was discovered in 1962, while the tau neutrino was not discovered until 2000.

Great interest in neutrino physics was raised by the discovery of flavor non-conservation. The first hints for this phenomenon date back to the late '60, when a deficit in the solar neutrino flux was observed. It took about thirty years to completely understand that neutrinos change flavor along the path from the sun to the earth. This phenomenon, named “oscillation”, was predicted by Pontecorvo in 1956 and shows that neutrinos have mass. Oscillations were then observed also in neutrinos produced in the atmosphere by cosmic rays and in neutrinos produced in nuclear reactors and accelerators.

In the last decade almost all oscillation parameters have been measured, giving a much clearer picture of neutrino physics. Most of the remaining open questions concerns its mass, which absolute value and nature cannot be determined by oscillation experiments. The search for neutrinoless double beta decay (0 ν DBD) is currently the only experimental technique able to probe neutrino mass and nature.

In this chapter, we present a brief review of the neutrino physics, focusing mostly on the experimental search for 0 ν DBD, that is the main scientific aim of the CUORE experiment.

3.1 Neutrino physics

3.1.1 Neutrino oscillations

The first indication of neutrino oscillations came from the chlorine solar neutrino experiment conducted by Raymond Davis Jr, in the Homestake mine in South Dakota [93]. This experiment observed only one third of the neutrinos coming from the sun predicted by the Standard Solar Model. The “solar neutrino problem”, as it came to be known, was solved by the Gallium experiments GALLEX [94] and SAGE [95]. Finally the SNO experiment confirmed that electron neutrinos were being converted into other neutrino flavors through the comparison of charged current reactions (sensitive only to ν_e) to neutral current reactions (sensitive to all three flavors) [96]. Finally, in 2002, the KamLAND collaboration published the first observation of the oscillation effect in neutrinos emitted by nuclear reactors [97]. The oscillation pattern is clearly visible in the last KamLAND publication (see figure 3.1).

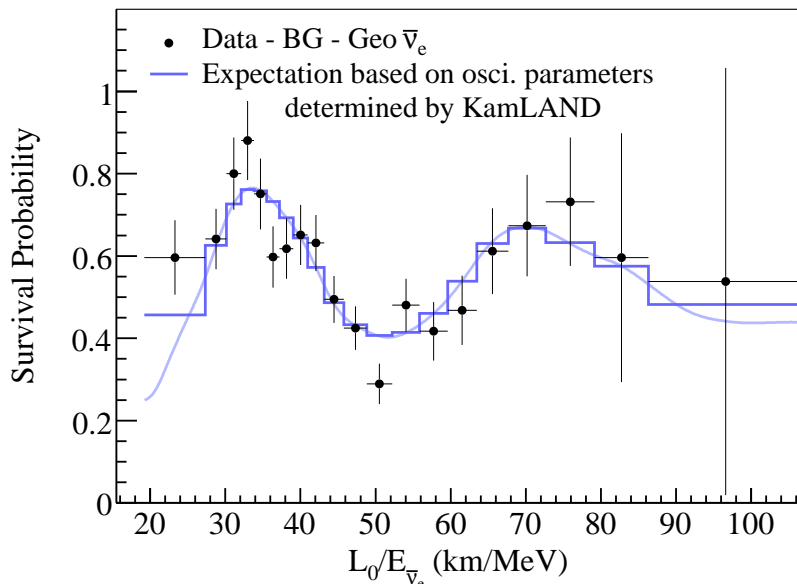


Figure 3.1. Electron anti-neutrino survival probability as a function of L/E measured by the KamLAND experiment. L_0 is the effective baseline taken as a flux-weighted average ($L_0 = 180$ Km). Figure taken from [98].

Moreover an anomaly in the atmospheric neutrino flux was observed by Super-Kamiokande [55]. The anomaly consisted in a difference between the flux of downward-going and upward-going ν_μ . The explanation for this observation is that the ν_μ s were oscillating into ν_τ s.

Neutrino oscillations occur because the weak flavor eigenstates (ν_e , ν_μ and ν_τ) are not aligned with the neutrino mass eigenstates (m_1 , m_2 and m_3). Flavor eigenstates $|\nu_f\rangle$ are related to mass eigenstates $|\nu_k\rangle$ by the Pontecorvo-Maki-Nakagawa-

Sakata (PMNS) neutrino mixing matrix:

$$|\nu_f\rangle = \sum_{k=1}^3 U_{fk}^* |\nu_k\rangle, \quad f = (e, \mu, \tau), \quad k = (1, 2, 3) . \quad (3.1)$$

The PMNS matrix U_{fk} can be parameterized as [99]:

$$U = \begin{bmatrix} 1 & 0 & 0 \\ 0 & c_{23} & s_{23} \\ 0 & -s_{23} & c_{23} \end{bmatrix} \times \begin{bmatrix} c_{13} & 0 & s_{13}e^{-i\delta} \\ 0 & 1 & 0 \\ -s_{13}e^{i\delta} & 0 & c_{13} \end{bmatrix} \times \begin{bmatrix} c_{12} & s_{12} & 0 \\ -s_{12} & c_{12} & 0 \\ 0 & 0 & 1 \end{bmatrix} \\ \times \begin{bmatrix} e^{i\phi_1/2} & 0 & 0 \\ 0 & e^{i\phi_2/2} & 0 \\ 0 & 0 & 1 \end{bmatrix} \quad (3.2)$$

where s_{12} and c_{12} indicate $\sin\theta_{12}$ and $\cos\theta_{12}$ for example. The angles θ_{12} , θ_{23} and θ_{13} are known as the mixing angles, and the parameter δ is a phase which account for the CP violation. In addition the parameters ϕ_1 and ϕ_2 are Majorana phases. These phases can also violate CP, but they are not observable in neutrino oscillations.

In the simple case with only two neutrino flavors ($\nu_f, \nu_{f'}$) and two mass eigenstates (ν_1, ν_2) the mixing matrix can be expressed in terms of a single mixing angle θ without phases (CP violation can occur only when there are three or more states). In this approximation the probability of detecting a neutrino with flavor f' at a distance L from the source, where they were produced with flavor f , is:

$$P(\nu_f \rightarrow \nu_{f'}; t) = \sin^2 2\theta \sin^2 \left(\frac{\Delta m^2}{4E} L \right) \quad (3.3)$$

where $\Delta m^2 = m_2^2 - m_1^2$ and E is the neutrino energy. As this equation clearly shows, oscillation experiments can extract the mixing angles and the squared mass differences but not the absolute mass value. The current results are summarized in Tab. 3.1, where it can be seen that the two mass splittings, as well as two over the three mixing angles have been measured with reasonable precision, while the small mixing angle θ_{13} is compatible with zero. If this angle vanishes the mixing matrix could be reduced to two independent 2×2 matrices, excluding the possibility of CP violation with neutrinos.

Table 3.1. Measured oscillation parameters [100].

Oscillation Parameter	Value
solar mass splitting	$\Delta m_{21}^2 = 7.65_{-0.20}^{+0.23} \times 10^{-5} \text{ eV}^2$
atmospheric mass splitting	$ \Delta m_{23}^2 = 2.40_{-0.11}^{+0.12} \times 10^{-3} \text{ eV}^2$
solar mixing angle	$\sin^2 \theta_{12} = 0.304_{-0.016}^{+0.022}$
atmospheric mixing angle	$\sin^2 \theta_{23} = 0.50_{-0.06}^{+0.07}$
'CHOOZ' mixing angle	$\sin^2 \theta_{13} = 0.010_{-0.011}^{+0.016}$

While the solar mass splitting is known with sign (*e.g.* $m_2 > m_1$), thanks to the matter effect in the sun, the atmospheric mass splitting is known only as absolute

value. This implies that we do not know if the mass hierarchy is normal ($m_3 > m_{1,2}$), following the pattern of the charged leptons, or inverted ($m_3 < m_{1,2}$). These possible scenarios are depicted in figure 3.2.

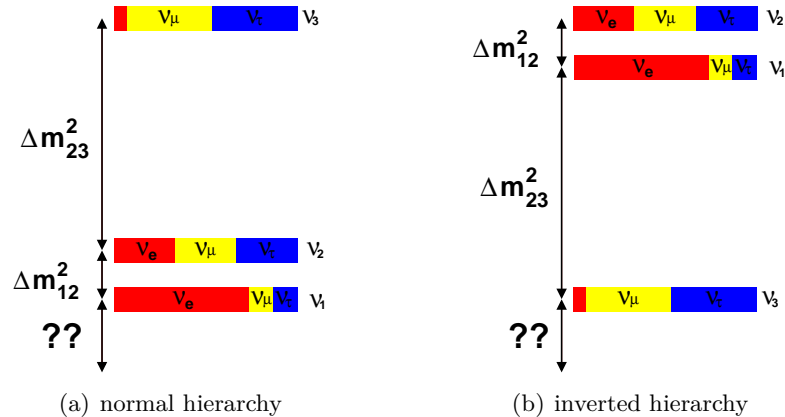


Figure 3.2. Neutrino mass hierarchies. The colored bands represent the contribution of each flavor to the mass eigenstate. The absolute mass scale is still unknown.

3.1.2 Neutrino masses

Even if the mass differences between neutrino states have been measured, the absolute values are still unknown. Limits on absolute neutrino masses come from cosmological constraints and from non oscillation experiments. Non oscillation experiments are mainly based on two methods. One method is the double beta decay and will be discussed later. The other method consists in the study of the endpoint of the beta decay spectrum, where the finite mass of the neutrino modifies the shape of the spectrum. The parameter that β -decay experiments measure is:

$$m_\beta^2 = \sum_{i=1}^3 |U_{ei}|^2 m_i^2. \quad (3.4)$$

Current best limits on m_β come from the Mainz [101] and Troitsk [102] tritium β -decay experiments ($m_\beta < 2.1$ eV). Next generation experiments plan to further constraint m_β in the sub-eV range, studying β -decay of tritium (KATRIN [103]) and ¹⁸⁷Re (MARE [104]).

Cosmological constraints on neutrino masses come from the observation of the Cosmic Microwave Background anisotropies and from the study of large scale structures. These observations are sensitive to the sum of the three neutrino masses. Limits range from few eV to few hundreds of meV, depending on the data being considered. However these constraints are less trustworthy, as they depend on cosmological models.

From the theoretical point of view, the neutrino is a massless particle in the Standard Model of particle physics, as there was no evidence for neutrino masses when this theory was formulated. Oscillation experiments have now changed this scenario, calling for an extension of the theory. The mass can be included as a Dirac mass term, as for all other fermions:

$$\mathcal{L}_{\text{mass}}^D = -m_D \bar{\nu}_R \nu_L + \text{H.c.} \quad (3.5)$$

where m_D is the Dirac mass that couple left-handed and right-handed neutrino. However, once the right-handed neutrino is introduced, due to the lack of electric charge, there is no reason not to include a Majorana mass term, where the neutrino is coupled to its charge conjugate:

$$\mathcal{L}_{\text{mass}}^{\text{M}} = \frac{1}{2} M_R \nu_R^T \mathcal{C}^\dagger \nu_R + \text{H.c.} \quad (3.6)$$

where M_R is the Majorana mass term and \mathcal{C} is the charge conjugation operator. The Majorana mass term for ν_L is not allowed by the symmetries of the Standard Model because it is not invariant under $\text{SU}(2)_L \times \text{U}(1)_Y$ transformations. On the other hand, the Majorana mass term for ν_R is allowed, being ν_R a singlet of $\text{SU}(3)_C \times \text{SU}(2)_L \times \text{U}(1)_Y$. Therefore a Dirac-Majorana mass term:

$$\mathcal{L}_{\text{mass}}^{\text{D+M}} = \mathcal{L}_{\text{mass}}^{\text{D}} + \mathcal{L}_{\text{mass}}^{\text{M}} \quad (3.7)$$

is allowed in the Standard Model. In order to understand the implications of the Dirac-Majorana mass term, it is useful to define the column matrix of left-handed chiral fields:

$$N_L = \begin{pmatrix} \nu_L \\ \nu_R^c \end{pmatrix} \quad (3.8)$$

so that $\mathcal{L}_{\text{mass}}^{\text{D+M}}$ can be rewritten as

$$\mathcal{L}_{\text{mass}}^{\text{D+M}} = \frac{1}{2} N_L^T \mathcal{C}^\dagger M N_L + \text{H.c.} \quad (3.9)$$

with

$$M = \begin{pmatrix} 0 & m_D \\ m_D & M_R \end{pmatrix}. \quad (3.10)$$

While both Majorana and Dirac mass terms are not excluded by any symmetry arguments, it is natural to ask the question why the neutrino is so much lighter than the other fermions. The See-saw mechanism provides a compelling mechanism to account for this discrepancy (for a detailed description see for example [105]). While the Dirac mass m_D , being generated by the Higgs mechanisms, is expected to be of the same order of magnitude of other fermions, there are no bounds for the Majorana mass M_R . In particular it can assume arbitrarily large values. If $M_R \gg m_D$ the two mass eigenstates of the Lagrangian (3.9) are:

$$\begin{aligned} \nu_1 &\simeq \nu_L, & m_1 &\simeq \frac{m_D^2}{M_R} \\ \nu_2 &\simeq \nu_R^c, & m_2 &\simeq M_R. \end{aligned} \quad (3.11)$$

If this condition is verified, the heavy neutrino ν_2 is predominantly ν_R^c and the light neutrino ν_1 is essentially the observed particle ν_L . Thus the introduction of the Majorana mass term in the Lagrangian leads to a natural explanation for the smallness of neutrino masses: the bigger is the mass of the unseen particle ν_R , the smaller is the mass of ν_L . Currently the only experimental method for determining the quantum nature of the neutrino is the search for neutrinoless double beta decay.

3.1.3 Neutrinoless Double Beta Decay (0νDBD)

Double Beta Decay (DBD) is a second-order weak process in which a nucleus changes its atomic number by two units:

$$(A, Z) \rightarrow (A, Z \pm 2) . \quad (3.12)$$

It occurs for some even-even nuclei for which the single beta decay is energetically forbidden, or suppressed by large change in angular momentum. Double beta decay accompanied by two neutrinos is allowed in the Standard Model (see figure 3.3(a)) and it was detected for the first time in ⁸²Se in 1987 [106]. Now, it has been observed on several other nuclei and the half-lives range from $\sim 10^{18}$ to $\sim 10^{22}$ years.

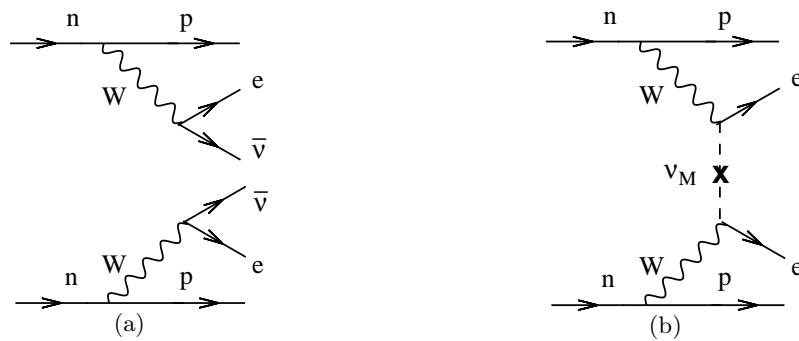


Figure 3.3. Double beta decay diagrams for the DBD mode (left) and the 0νDBD mode (right). The 0νDBD diagram assumes that the process is mediated by the exchange of a Majorana neutrino.

The DBD without emission of neutrinos (0νDBD) is instead forbidden in the Standard Model, since it violates the lepton number by two units. Neutrinoless double beta decay can proceed through many different mechanisms: almost any physics that violates the total lepton number can generate it [107].

The simplest way to obtain neutrinoless double beta decay is by the exchange of a massive Majorana neutrino (see figure 3.3(b)). However, no matter which particular mechanism holds, this decay would imply the existence of a Majorana neutrino mass term [108]. This is shown in figure 3.4: the 0νDBD decay can be inverted to produce a $\bar{\nu}_e$ going into a ν_e or, in other words, a Majorana mass term.

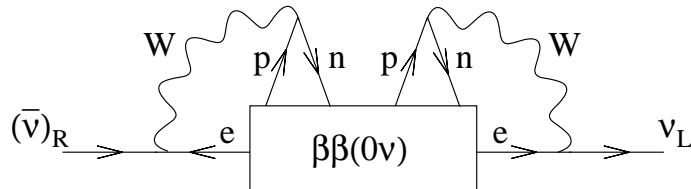


Figure 3.4. Conversion from $\bar{\nu}_e$ to ν_e by a 0νDBD interaction. This diagram proves that the existence of 0νDBD-decay would imply a Majorana mass for neutrino, no matter what is the mechanism that gives rise to the transition.

The rate of this process can be written as [109]

$$\left[T_{1/2}^{0\nu}\right]^{-1} = G_{0\nu} |M_{0\nu}|^2 \langle m_{\beta\beta} \rangle^2 \quad (3.13)$$

where $G_{0\nu}$ and $M_{0\nu}$ are respectively the phase space factor and the nuclear matrix element (NME) for the $0\nu\text{DBD}$ transition, and $m_{\beta\beta}$ is the effective Majorana mass:

$$m_{\beta\beta} = \left| \sum_{j=1}^3 U_{ej}^2 m_j \right| = \left| \sum_{j=1}^3 |U_{ej}|^2 e^{i\phi_j} m_j \right|. \quad (3.14)$$

In contrast to single beta decay, where m_β was a function of the three $|U_{ei}|^2$, $m_{\beta\beta}$ is a function of the U_{ei}^2 and is therefore sensitive to the two Majorana phases. Since the U_{ei} and the two squared mass differences are known from oscillation experiments, $m_{\beta\beta}$ can be written in terms of only three unknown parameters, the mass of the lightest neutrino and the two Majorana CP phases. The result is shown in figure 3.5, where the allowed values for $m_{\beta\beta}$ are plotted as a function of the lightest neutrino mass.

Apart for a controversial claim, later discussed, neutrinoless double beta decay has never been observed. Current experimental limits are reported in Tab. 3.2.

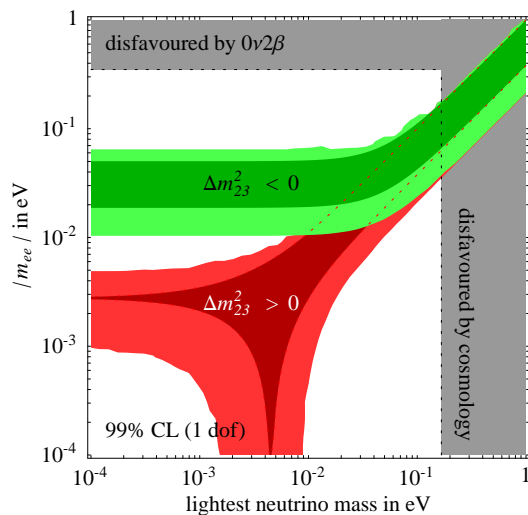


Figure 3.5. Allowed values for the effective Majorana mass as a function of the mass of the lightest neutrino. The green band represents the allowed value in the case of inverted neutrino mass hierarchy, while the red band is for the normal hierarchy case. The region where the green and the red bands overlap is known as “degenerate mass hierarchy”. The darker bands represent the allowed regions that would be obtained if the parameters from oscillation experiments were measured with infinite precision. The gray regions represent the parameter space that is excluded by current $0\nu\text{DBD}$ experiments and by cosmological observations. Figure taken from [105].

Table 3.2. Commonly studied double beta decay isotopes and best lower limits for the 0νDBD half lives. The claim of observation in ⁷⁶Ge will be discussed later.

Parent Isotope	$T_{1/2}^{0\nu}(y)$	Reference
⁴⁸ Ca	$> 1.4 \times 10^{22}$	[110]
⁷⁶ Ge	$> 1.9 \times 10^{25}$	[111]
⁷⁶ Ge	1.19×10^{25}	[112]
⁸² Se	$> 1 \times 10^{23}$	[113]
⁹⁶ Zr	$> 1.0 \times 10^{21}$	[114]
¹⁰⁰ Mo	$> 4.6 \times 10^{23}$	[113]
¹¹⁶ Cd	$> 1.7 \times 10^{23}$	[115]
¹³⁰ Te	$> 2.8 \times 10^{24}$	[116]
¹³⁶ Xe	$> 1.2 \times 10^{24}$	[117]
¹⁵⁰ Nd	$> 1.8 \times 10^{22}$	[118]

3.2 Experimental search for 0νDBD

The amount of kinetic energy released in double beta decay, called Q -value, is given by the difference between the mass of the parent nucleus and the mass of the daughter nucleus plus the mass of the two emitted electrons:

$$Q_{\beta\beta} = M_p - (M_d + 2m_e) . \quad (3.15)$$

In the double beta decay the two neutrinos carry away part of the energy, giving rise to a continuous spectrum of the sum energy of the two electrons. In the neutrinoless decay all the energy goes into the electrons, so that the signature is a monochromatic line in the energy spectrum (see figure 3.6).

The sensitivity of an experiment is defined as the half-life corresponding to the minimum number of signal events observable above background at a given statistical significance. For experiments in which the background counts scale as the total mass of the detector it can be expressed as [109]

$$S^{0\nu}(n_\sigma) = \frac{\ln 2}{n_\sigma} \epsilon N_a \frac{\eta}{A} \sqrt{\frac{M \cdot t}{b \cdot \Delta E}} , \quad (3.16)$$

where n_σ is the statistical significance, ϵ is the detection efficiency, N_a is the Avogadro number, η is the isotopic abundance of the studied nucleus, A is the atomic mass number, M is the total detector mass, t is the live time of the experiment, ΔE is the resolution and b is the background, expressed in counts/(keV · kg · years). To compare the discovery potential of experiments using different isotopes, it is convenient to define the nuclear factor of merit F_N :

$$F_N = m_e^2 G_{0\nu} |M_{0\nu}|^2 \quad (3.17)$$

where m_e is the electron mass and F_N has dimension of years⁻¹. Using equation (3.13) and replacing the half-life with the sensitivity, the Majorana mass that an experiment is able to measure can be expressed as:

$$m_{\beta\beta} = \frac{m_e}{\sqrt{S^{0\nu} \cdot F_N}} \quad (3.18)$$

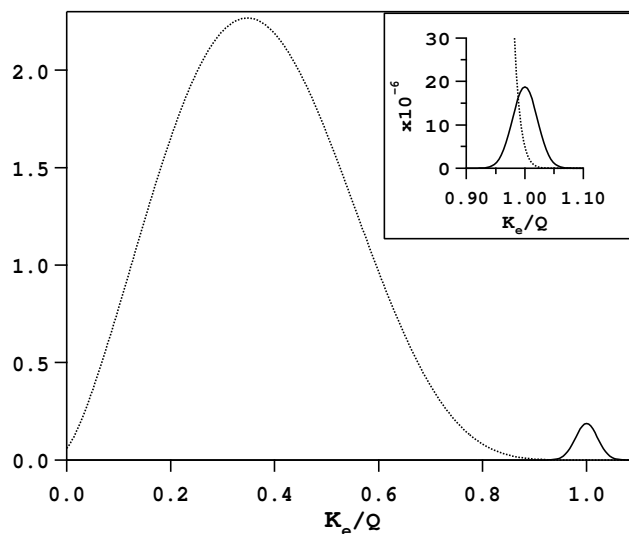


Figure 3.6. Illustration of the spectra of the sum of the electron kinetic energies K_e (Q is the endpoint) for the DBD (dotted curve) and the $0\nu\text{DBD}$ (solid curve). The spectra are convolved with an energy resolution of 5%. The small insert shows how a poor energy resolution can lead to the confusion of the $0\nu\text{DBD}$ peak with the tail of the DBD spectrum.

where the sensitivity accounts for the experimental features and the nuclear factor of merit account for the $0\nu\text{DBD}$ isotope. In Tab. 3.3 the nuclear factor of merit, the Q -value and the natural abundance of the most used $0\nu\text{DBD}$ candidates is reported. Isotopes with high Q -values are preferred for several reasons. First the background from natural radioactivity decreases with increasing Q . A marking point is represented by the 2615 keV line from ^{208}Tl , the γ -line from natural radioactivity with the highest energy. Isotopes with Q -values above this energy benefit from a much lower background level. Other reasons to prefer big Q -values are represented by the fact that the phase space factor that appears in the formula for the decay rate scales as $G_{0\nu} \sim Q^5$ [107], and that the fraction F of the DBD counts in the region of the $0\nu\text{DBD}$ peak scales as $F \sim 1/Q^5$ [120].

Table 3.3. Nuclear factor of merit, Q -value and natural abundance (η) for several double beta decay isotopes of experimental interest. The values of F_N are taken from [119].

Parent Isotope	$F_N [y^{-1}]$	$Q_{\beta\beta} [\text{keV}]$	$\eta [\%]$
^{48}Ca	$0.54 \cdot 10^{-13}$	4271	0.19
^{76}Ge	$0.73 \cdot 10^{-13}$	2039	7.4
^{82}Se	$1.7 \cdot 10^{-13}$	2995	8.7
^{100}Mo	$5.0 \cdot 10^{-13}$	3034	9.6
^{116}Cd	$1.3 \cdot 10^{-13}$	2902	7.5
^{130}Te	$4.2 \cdot 10^{-13}$	2527	34.1
^{136}Xe	$0.28 \cdot 10^{-13}$	2479	8.9
^{150}Nd	$57 \cdot 10^{-13}$	3367	5.6

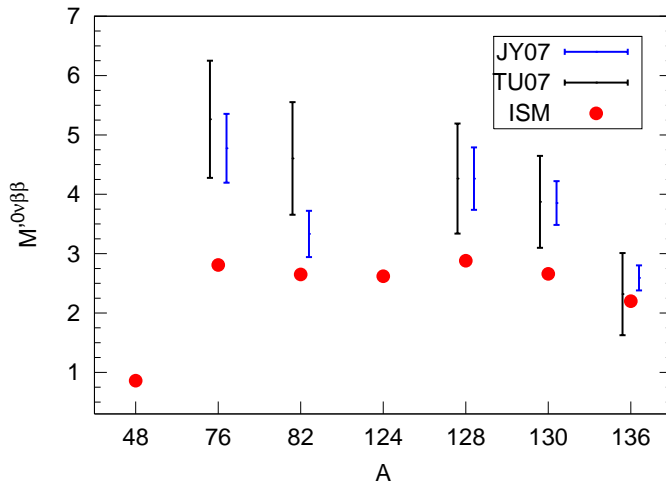


Figure 3.7. Nuclear matrix element calculations for several 0νDBD isotopes using QRPA (black and blue bars) and NSM (red dots). The bars represent the spread introduced in QRPA calculations by the different choices for the coupling constant g_A . Figure taken from [121].

Even if the observation of neutrinoless double beta decay of an isotope is enough to make the discovery, the confirmation and the comparison with different isotopes is needed. Different isotopes have different phase space factors and nuclear matrix elements (see equation 3.13), so these quantities must be known to combine and compare the results of different experiments. While the phase space factor can be evaluated exactly, NME represents the biggest source of theoretical uncertainty and cannot be determined experimentally, as it occurs only in the 0νDBD. Nuclear matrix elements depend on the structure of the parent and daughter nuclei, as well as the intermediate one. Since a many bodies problem must be solved, the calculation cannot be carried out analytically, but requires numerical computations in which several approximations are introduced. There are two basic approaches for the evaluation of nuclear matrix elements, the quasi-particle random phase approximation (QRPA) and the nuclear shell model (NSM). Fig. 3.7 shows the nuclear matrix element calculations for various 0νDBD isotopes using the two different techniques.

3.2.1 Past and present experiments

Past and running double beta decay experiments have typical sensitivities that allow to span the effective Majorana mass corresponding to the degenerate neutrino mass hierarchy pattern (see figure 3.5). There are mainly two experimental approaches. In the *source = detector* approach the DBD emitter is part of or constitute the detector. In this way particles are fully absorbed in the detector, allowing high detection efficiency (of order 90%) and high resolution (few keV). Nevertheless there is no sensitivity to the event topology and nature, reducing the background rejection capability. In the *source ≠ detector* approach the DBD emitter is passive and is surrounded by an active detector. Exploiting the typical signature of a two electrons event, the background rejection is very high. On the other hand the

resolution is poor (hundreds of keV) as well as the detection efficiency (of order 30%). Examples of the *source = detector* approach are the Heidelberg-Moscow and the CUORICINO experiments. An example of the *source \neq detector* approach is the NEMO 3 experiment.

The best half life limit on $0\nu\text{DBD}$ (a complete list is in Tab. 3.2) has been obtained so far in ^{76}Ge by the Heidelberg-Moscow collaboration, using High Purity Germanium semiconductors (HPGe) as detectors. Similar results were also achieved in the IGEX experiment [122]. The big advantage of semiconductor detectors is their excellent energy resolution (about 4 keV at 2 MeV). Even if these devices can only measure the sum energy of the two electrons emitted in the decay, some background reduction can be obtained by exploiting pulse shape analysis. The Heidelberg-Moscow experiment took data in the period 1999-2003 in the Laboratori Nazionali del Gran Sasso (LNGS) using five HPGe detectors. The total detector mass was 11 kg, enriched to about 86% in ^{76}Ge . A background of 0.12 counts/keV/kg/y was obtained around the Q-value of the decay, the best ever so far. With a statistics of $35.5 \text{ kg} \cdot \text{y}$ in ^{76}Ge the half life limit obtained by the Heidelberg-Moscow collaboration is $T_{1/2}^{0\nu} > 1.9 \times 10^{25} \text{y}$ at 90% C.L. [111]. Using NME calculations from [123] this corresponds to a limit for the effective Majorana mass of $m_{\beta\beta} < 0.35 \text{ eV}$. In 2001 a subgroup of the collaboration found a small peak at the expected position [124, 112] (see figure 3.8) and reported an evidence for neutrinoless double beta decay in ^{76}Ge with an half life in the range $0.7 \div 4.2 \times 10^{25} \text{y}$ (3σ). Using NME from [123], this result would convert into a value for $m_{\beta\beta}$ in the range $0.2 \div 0.6 \text{ eV}$. However, the discussion concerning the possible evidence is quite controversial, mainly because the understanding of the background in the region of the peak is not so clear.

Competitive limits on neutrinoless double beta decay come also from the Neutrino Ettore Majorana Observatory (NEMO 3 [125]). Being a tracking experiment, NEMO 3 is not only able to measure the total released energy, but also the energy of the single electrons, their angular distribution and the position where they are produced. NEMO 3 is located in the Frejus Underground Laboratory

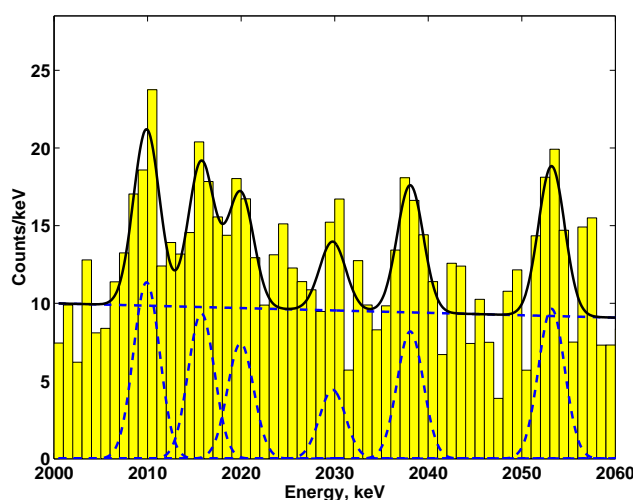


Figure 3.8. Energy spectrum measured by the Heidelberg-Moscow experiment around the Q-value of ^{76}Ge (2039 keV). Picture taken from [112].

(France) under a 4800 m w.e. rock shield. The detector has a cylindrical structure composed by 20 identical sectors. In each sector a thin foil 0νDBD source (30-60 g/cm²) is surrounded by a He-filled tracking detector consisting in drift cells operating in Geiger mode. A magnetic field facilitates identification of the background produced by electron-positron pairs. The tracking chambers are surrounded by plastic scintillators to measure the energy of the two electrons. Thanks to the easy way in which the source foils can be replaced in the detector, NEMO 3 can be used to study any kind of 0νDBD isotope. Its great background rejection capabilities make this detector an ideal tool to study the two neutrino double beta decay mode. At present seven isotopes have been investigated, ¹⁰⁰Mo, ⁸²Se, ¹¹⁶Cd, ¹⁵⁰Nd, ⁹⁶Zr, ¹³⁰Te and ⁴⁸Ca, but the source mass (about 10 kg) is fairly dominated by ¹⁰⁰Mo (about 7 kg) and ⁸²Se (about 1 kg). Figure 3.9 gives an idea of the background rejection capabilities of this experiment. It represents the measured DBD spectra for ¹⁰⁰Mo and ⁸²Se. The corresponding values for the 0νDBD half lives are $T_{1/2}^{2\nu} = [7.11 \pm 0.02(stat) \pm 0.54(syst)] \times 10^{18} y$ for ¹⁰⁰Mo and $[9.6 \pm 0.3(stat) \pm 1.0(syst)] \times 10^{19} y$ for ⁸²Se. Limits on the 0νDBD decay channel have also been obtained by NEMO 3: $T_{1/2}^{0\nu} > 4.6 \times 10^{23} y$ (¹⁰⁰Mo) and $T_{1/2}^{0\nu} > 1.0 \times 10^{23} y$ (⁸²Se). The corresponding upper limits for the effective Majorana mass range from 0.7 to 2.8 eV for ¹⁰⁰Mo and from 1.7 to 4.9 eV for ⁸²Se (see references in [113] for the NME used to obtain these limits).

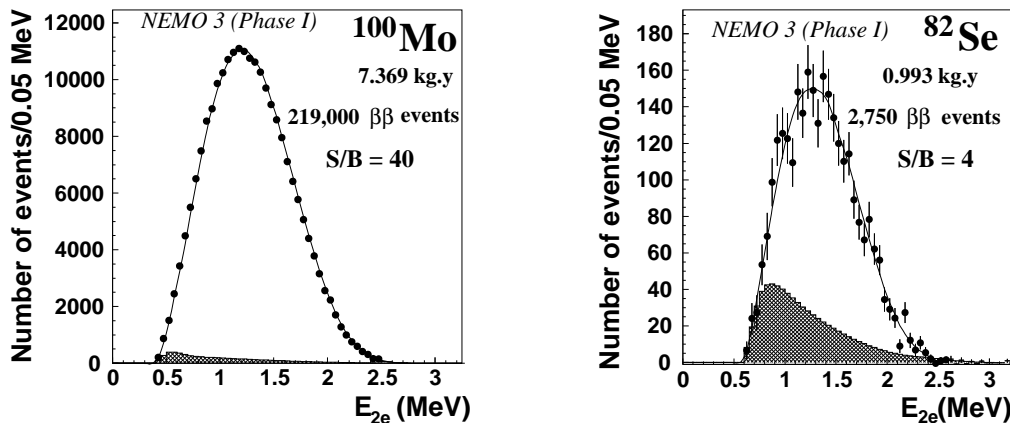


Figure 3.9. Two neutrino double beta decay spectra after background subtraction for ¹⁰⁰Mo (left) and ⁸²Se (right) measured by NEMO 3. The black dots represent the data, the solid line is the DBD spectrum expected from simulations and the shaded histogram is the subtracted background. Pictures taken from [113].

3.3 CUORE and its precursors

The use of bolometric detector for the search of 0νDBD was proposed by Fiorini and Niinikoski in 1984 [126]. Since more than twenty years, his research group has been developing cryogenic detectors of increasing mass. The successful operation of a 340 g Tellurium dioxide crystal [127] was followed by the construction of a detector array composed by 20 crystals, for a total mass of 6.8 kg of TeO₂ (MiDBD [128]).

A further mass increase was obtained with the recently completed CUORICINO

experiment [129, 130, 131]. Operated in the Laboratori Nazionali del Gran Sasso (LNGS) in the years 2003-2008, CUORICINO was composed by a tower of 62 TeO₂ bolometers, with a total mass of ~ 41 kg. At present the CUORICINO results represent one of the most competitive limits for the effective Majorana mass, comparable with the ones obtained with Germanium detectors.

The excellent performances obtained with CUORICINO demonstrates the feasibility of a ton scale bolometric experiment, CUORE [132, 133] aiming at the investigation of $m_{\beta\beta}$ in the inverted mass hierarchy range.

3.3.1 CUORICINO

CUORICINO was an array of 62 TeO₂ bolometers arranged in a tower of 13 floors (see Fig. 3.10(a)) hosted in a dilution refrigerator that allowed to operate the detectors at a temperature of ~ 8 mK. Eleven floors were made of four $5 \times 5 \times 5$ cm³ crystals each, while the two remaining floors were composed by nine $3 \times 3 \times 6$ cm³ crystals each (see respectively Fig. 3.10(b) and Fig. 3.10(c)).

The experiment was located in the Hall A of the LNGS, under a mountain that provides a ~ 3400 m.w.e. shield against cosmic rays: the muon flux is reduced to $\sim 3 \cdot 10^{-8} \mu \text{ cm}^{-2} \text{ s}^{-1}$ [134] and the neutron flux to $\sim 10^{-6} n \text{ cm}^{-2} \text{ s}^{-1}$ [135]. Several layers of low radioactivity lead and borated polyethylene were also used to shield the detectors and minimize the background.

CUORICINO took data for five years, collecting a statistics of 19.75 kg(¹³⁰Te)y. Data were analyzed assuming a Q-value of 2527.518 ± 0.013 keV [136]. The background rates in the $0\nu\text{DBD}$ region were 0.161 ± 0.005 counts/keV/kg/y for the $5 \times 5 \times 5$ cm³ crystals and 0.163 ± 0.014 counts/keV/kg/y for the small crystals. The energy resolution was evaluated to be about 6 keV and about 10 keV FWHM

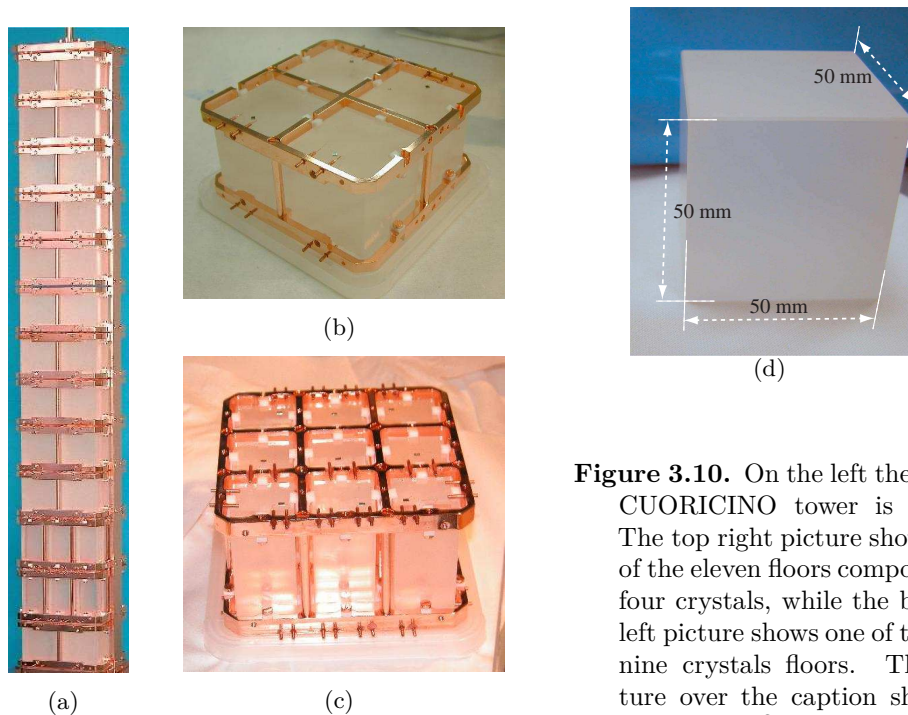


Figure 3.10. On the left the entire CUORICINO tower is shown. The top right picture shows one of the eleven floors composed by four crystals, while the bottom left picture shows one of the two nine crystals floors. The picture over the caption shows a $5 \times 5 \times 5$ cm³ TeO₂ crystal.

for the big and the small crystals respectively. The single-hit spectrum is shown in Fig. 3.11.

The experiment was able to set a lower limit of $2.8 \cdot 10^{24} \text{y}$ for the $0\nu\text{DBD}$ half life of ^{130}Te corresponding to $m_{\beta\beta} < 0.3 \div 0.7 \text{ eV}$, depending on the nuclear matrix element evaluation [121, 137, 138, 139].

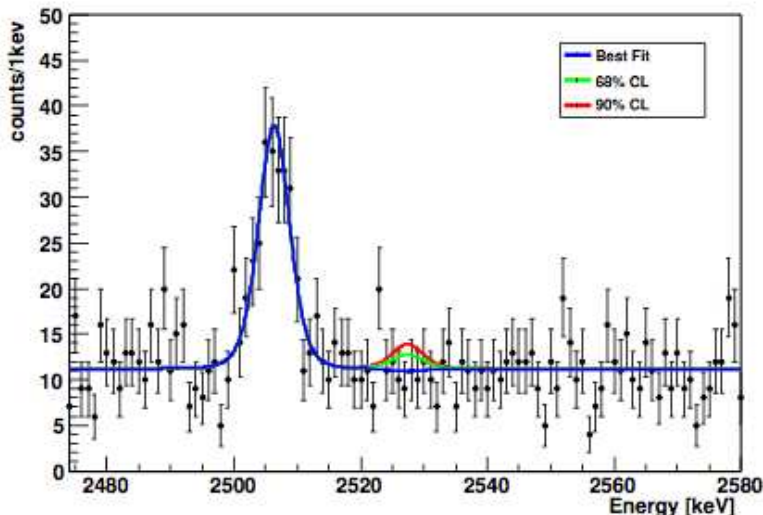


Figure 3.11. Single hit background spectrum of CUORICINO. The peak at 2505 keV is produced by the two gammas emitted in the beta decay of ^{60}Co . It is about 7σ away from the position where the $0\nu\text{DBD}$ peak is expected. The blue line represent the best fit to the number of $0\nu\text{DBD}$ events, the green line and the red line are respectively 68% and 90% C.L. bounds. Figure from [116].

3.3.2 CUORE

The CUORE experiment will search for $0\nu\text{DBD}$ in ^{130}Te using an array of 988 TeO_2 bolometers, with a total mass of $\sim 740 \text{ kg}$, corresponding to about $9.4 \cdot 10^{26}$ ^{130}Te nuclei. The bolometers will be arranged in a cylindrical structure organized into 19 towers. Each tower, very similar to CUORICINO, will be made 13 floors, each floor being composed by four crystals (see Fig. 3.12). The closely packed structure of the CUORE array will take great advantage from the high background rejection capability that can be obtained by operating the detectors in anti-coincidence. Since there is a small probability for the two $0\nu\text{DBD}$ electrons to escape from the crystal where they are produced, a simultaneous hit in more than one detector is an indication of a background event. In contrast to CUORICINO, most of the crystals will be completely surrounded by other detectors, thus allowing an easier identification of crystal surface contaminations.

Compared to CUORICINO, the detector mass will be increased by a factor of twenty and the background will be reduced by about the same amount. The data taking of CUORE is foreseen to start in 2013: after five years an half life sensitivity of the order of 10^{26} y is expected. Even if the mass increase will require much effort, mainly due to technological issues concerning the cryogenic apparatus, the biggest

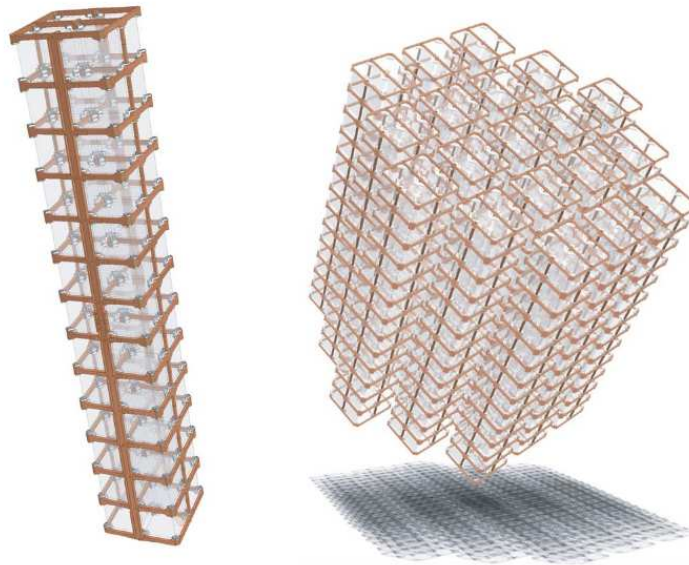


Figure 3.12. The CUORE detector array is roughly 19 times CUORICINO.

challenge will be the achievement of an adequately low background level. The goal of the CUORE collaboration is to reach a background of $\sim 10^{-2}$ counts/keV/kg/y in the $0\nu\text{DBD}$ region: this corresponds to observing less than 1 count per crystal over 10 years in an energy window of 10 keV centered at the Q-value of the decay. In the hoped case, CUORE will have half-life sensitivity of about $2.1 \cdot 10^{26}$ y in five years (see figure 3.13).

The detector will be hosted in the Hall A of LNGS, the same experimental hall of CUORICINO. The entire array, surrounded by a 6 cm thick lead shield, will be operated at about 10 mK in a $^3\text{He}/^4\text{He}$ dilution refrigerator (see Fig. 3.14). A further thickness of 25 cm of low activity lead will be positioned on top of the detector array in order to shield it from the materials in the dilution unit of the refrigerator and from the environmental radioactivity. A borated polyethylene shield will protect the detector from neutrons and an anti Radon air-tight cage will surround externally the cryostat.

CUORICINO was calibrated facing Thorium sources to the detector from the outside of the cryostat (as explained in Sec. 4.6). The greater amount of TeO_2 in CUORE makes this technique not usable. If the detector were exposed to an external source, the innermost bolometers would experience a much lower rate of calibration events than the outermost. Sources of different intensity could be used to calibrate at different times inner and outer bolometers. Given that this procedure should last at least a week, and given that the calibration is repeated every month, the live time of the experiment could be significantly reduced. An alternative option consists in inserting the sources between the towers, in the 10 mK environment. The system to lower and raise the sources is currently being developed, taking into account the radioactivity constraints and the time needed to thermalize the sources from 300 K to 10 mK, that even in this case could not be negligible.

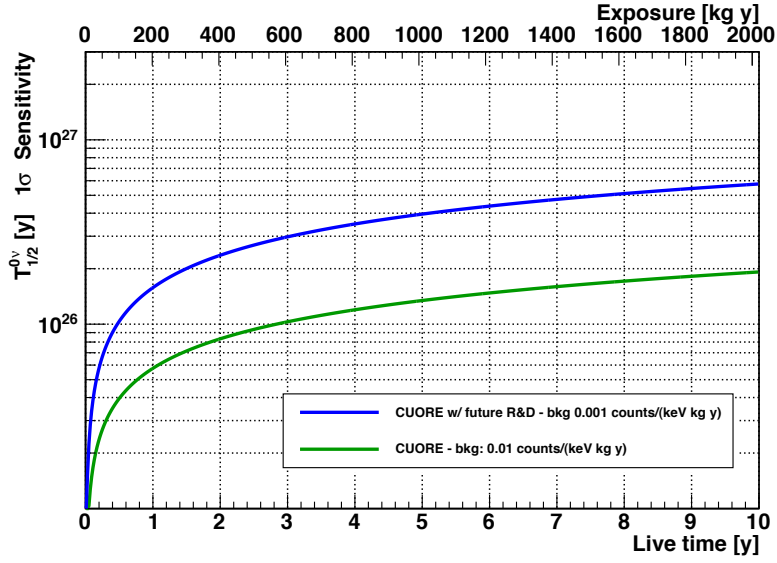


Figure 3.13. CUORE sensitivity to the $0\nu\text{DBD}$ half-life of ^{130}Te in two background scenarios, 0.01 counts/keV/kg/y and 0.001 counts/keV/kg/y.

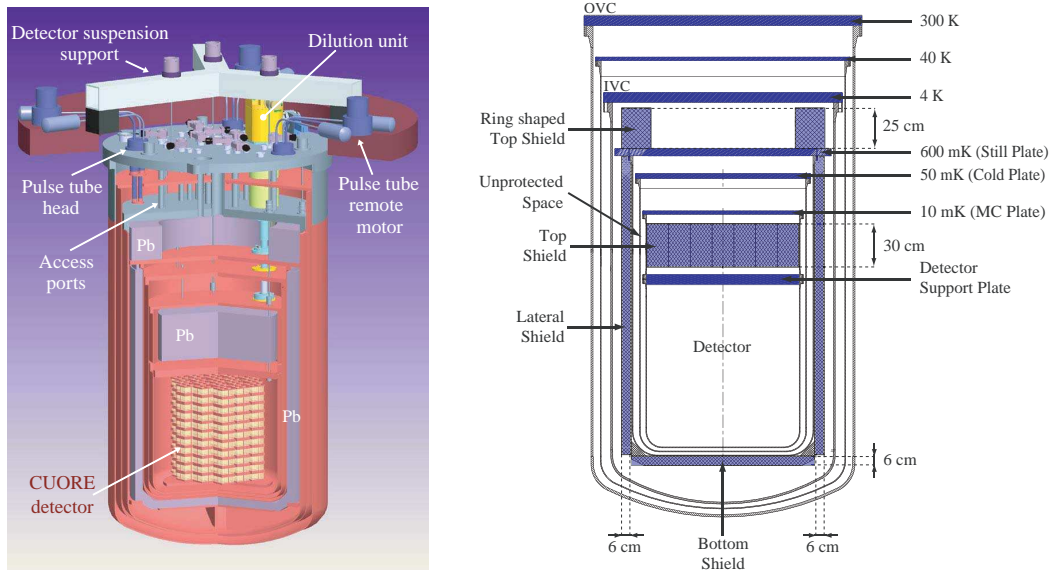


Figure 3.14. CUORE cryostat and internal shields.

3.3.3 On the road to CUORE: CUORE-0

CUORE-0 will be essentially a single column of CUORE to be installed and operated in the CUORICINO dilution refrigerator placed in the Hall A of the LNGS. Its construction started at the end of 2010, while the data-taking will start in 2011.

CUORE-0 will adopt all the procedures for the assembly foreseen for CUORE itself, which will be totally different from the ones adopted for CUORICINO. The main point is that all the handling and assembly operations will be performed without any contact with ambient air. A set of proper glove boxes will allow to build the detectors in a controlled nitrogen atmosphere and according to a rigid

protocol which will make the assembly procedure essentially operator independent. In particular, the very delicate operation of absorber-sensor coupling through bi-component epoxy (see Sec. 4.3) will be almost automated and realized through programmable robots, aiming at a better detector reproducibility. CUORE-0 will also represent by itself a powerful experiment to search $0\nu\text{DBD}$ of ^{130}Te .

The CUORE-0 motivations are manifold, and can be summarized as follows:

- test of the CUORE assembly chain and procedure,
- high statistics test of crucial components of the estimated CUORE background,
- test of the bolometric behavior of the detectors,
- test of the CUORE Data Acquisition,
- test of the CUORE analysis tools.

3.3.4 CUORE Crystals Validation Run 2

The path towards CUORE is not only CUORE-0. A lot of test runs were performed (and will be performed) in order to test all the parts of the final detector. In particular, the trigger developed and discussed in this thesis (see Ch. 5 and Ch. 6) has been tested on the data of a measurement that was done to check one of the first batches of CUORE crystals, the second CUORE Crystals Validation Run (CCVR2). The detector was an array of four crystals (like a CUORE single module, described in Sec. 4.3), representative of two different batches, as shown in Tab. (3.4). Each crystal was provided with two thermistors (instead of one) to be sure to have, at least, one “good” channel per crystal.

CCVR2 detector was hosted in a dilution refrigerator placed in the Hall C of the LNGS and took data during June 2009.

Table 3.4. CCVR2 crystals. Crystals were produced in China and then sent to LNGS by plane or by ship.

Crystal	Date of production (yyyy-mm-dd)	Date of arrival at LNGS (yyyy-mm-dd)	Transport	Tellurium Batch
007	2008-09-23	2008-12-01	air	010001
011	2008-09-23	2008-12-01	air	010001
076	2009-01-23	2009-05-12	sea	010003
096	2009-01-23	2009-05-12	sea	010003

Chapter 4

The bolometric technique

Bolometers are calorimeters operating at low temperature, in which the energy deposited by a particle is converted into phonons and is detected as a temperature variation. Usually particle detectors are sensitive to a single energy release mechanism. For example scintillators can measure the light emitted by atomic de-excitations, while ionization detectors are sensitive to the electron-ion pairs that are produced in them. In any case the main consequence is that only a small fraction of the total released energy can be detected in these devices. Due to statistical fluctuations, this results in an intrinsic limit in the energy resolution. In contrast bolometric detectors have a much smaller intrinsic energy resolution, as almost all the released energy is eventually converted into heat, which is the physical quantity that these devices can measure.

The first proposal to use bolometers as particle detectors dates back to more than 70 years ago [140]. Since then, these devices have been used in many research fields (X-ray spectroscopy, material contamination analysis, Dark Matter search and others) and actually represent one of the most promising approaches to the search of $0\nu\text{DBD}$.

In the following chapter we present the bolometers working principles and an overview of the various components of these detectors. We report also a basic description of the data acquisition and of the standard analysis chain.

4.1 Working principles

A bolometer is a calorimeter, essentially constituted by two components (Fig. 4.1): an energy absorber and a sensor that converts thermal excitations into a readable signal. The absorber must be coupled to a constant temperature bath by a weak thermal conductance, which acts as heat discharger. Denoting by C the heat capacity of the bolometer, the temperature variation induced by an energy release E can be written as

$$\Delta T = \frac{E}{C} \quad (4.1)$$

The accumulated heat flows then to the heat sink through the thermal link and the absorber returns to the base temperature with a time constant $\tau = C/G$, where G is the thermal conductance of the link:

$$\Delta T(t) = \frac{E}{C} \exp\left(-\frac{t}{\tau}\right). \quad (4.2)$$

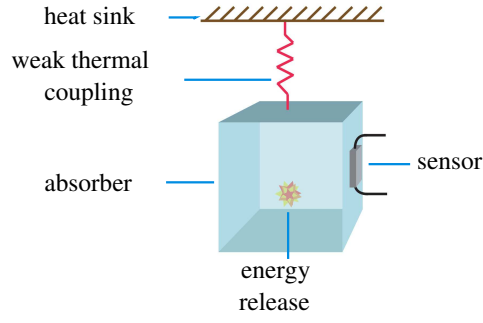


Figure 4.1. Schematic representation of a bolometric detector: an absorber is connected to a heat sink through a weak thermal coupling and a sensor for signal readout is attached to the absorber.

In order to obtain a measurable temperature rise, the heat capacity of the absorber must be very small: this is the main reason why bolometers need to be operated at cryogenic temperatures (of the order of $10 \div 100$ mK).

4.1.1 Energy absorber

The specific heat of a material at low temperature is given by the sum of two contributions, one coming from the thermal excitation of the lattice and the other related to the conduction electrons:

$$c(T) = c_l(T) + c_e(T). \quad (4.3)$$

The lattice specific heat is described by the Debye law:

$$c_l(T) = \frac{12}{5} \pi^4 N_a k_B \left(\frac{T}{\Theta_D} \right)^3 \quad T < \Theta_D \quad (4.4)$$

where N_a , k_B and Θ_D are the Avogadro number, the Boltzmann constant and the Debye temperature respectively. In metals the specific heat of the electrons is:

$$c_e(T) = \frac{ZR}{\Theta_D} \pi^2 \frac{T}{\Theta_F} \quad (4.5)$$

where Z , R and Θ_F are the number of conduction electrons, the gas constant and the Fermi temperature respectively. Given the different temperature dependence of c_l and c_e , the electron specific heat dominates at low temperatures. Dielectric and diamagnetic materials, lacking in electron contribution, have then low capacitance and are preferred.

In a very simplified model in which all the thermal phonons are detected, a rough estimate of the energy resolution can be derived. The thermodynamic equilibrium between the absorber and the heat sink is hold by a continuum exchange of phonons trough the conductance K . The fluctuation of the number of phonons in the absorber produces a temperature variation that in turns affects the energy resolution. The energy E in the absorber is

$$E = C(T) \cdot T \quad (4.6)$$

or, in terms of the energy of each phonon $\epsilon = k_B T$,

$$E = N \cdot \epsilon . \quad (4.7)$$

Assuming that the number of phonons obeys the Poisson statistics, the energy fluctuation is:

$$\Delta E = \Delta N \cdot \epsilon = \sqrt{k_B C(T) T^2} . \quad (4.8)$$

It should be stressed that, at least for CUORE bolometers, the thermodynamic fluctuations give a negligible contribution to the energy resolution. From the above expression, using typical values of CUORE bolometers ($C = 10^{-9}$ J/K, $T = 10$ mK), a resolution of ~ 10 eV is predicted, that is well below the measured resolution (few keV).

Upon the arrival of a particle, the energy release process that eventually lead to detectable thermal phonons can occur through interactions with the lattice (nuclear channel) or with the electrons in the absorber material (electronic channel) [141]. The nuclear channel is relevant for α and β particles, but not for electromagnetic radiation. When the thermalization process occurs via this channel there is the possibility that a fraction of the released energy remains trapped in structural defects of the absorber, thus causing a degradation in the energy resolution. The fraction of lost energy depends on the incident particle: it is negligible for α particles, but it can worsen the resolution to few hundreds eV for electrons or gammas with an energy of few MeV.

In the case of electronic channel the interacting particle produces electron-hole pairs in the absorber material. These charge carriers, initially produced near the interaction point, spread very quickly in the detector and interact with each other until a quasi-equilibrium condition is reached. Afterwards they undergo interactions with the lattice sites. In this step a large fraction of the initial energy is transferred to the lattice as vibrational excitations (phonons), but it is possible for part of the energy to leave the crystal or to be stored in stable or meta-stable states. Radiative recombinations of electron-hole pairs with the escape of the emitted photon, non radiative recombinations that take too much time compared to signal development, trapping of electrons and holes in impurity sites or lattice defects can cause a worsening of the energy resolution. Electron-hole pairs recombinations and scattering on lattice impurities produce high energy and low momentum phonons in the optical branch, which in turn decay in a very short time (of the order of 100 ps) in longitudinal acoustic branch (LA) phonons (Fig. 4.2). As the decay obeys to energy and momentum conservation, each phonon from the optical branch typically produces two LA phonons with opposite momentum and energy of the order of $k_B \Theta_D$. However this energy is still much higher than the average phonon energy in thermal equilibrium. The thermalization proceeds then through phonon-phonon interactions, scattering on impurities and on crystal surfaces. The first mechanism is possible thanks to the anharmonicity of the lattice potential, and leads to the production of phonons in the transverse acoustic branch. Since energy degradation through phonon-phonon interactions becomes less effective as long as the phonon energy is approaching the equilibrium temperature, in the last stage of thermalization the dominant process becomes scattering on impurities and crystal surfaces.

4.1.2 The choice of TeO₂

CUORE uses TeO₂ crystals as absorbers. The use of TeO₂ is motivated by various reasons, some of them related to the $0\nu\text{DBD}$ candidate isotope (^{130}Te) and others

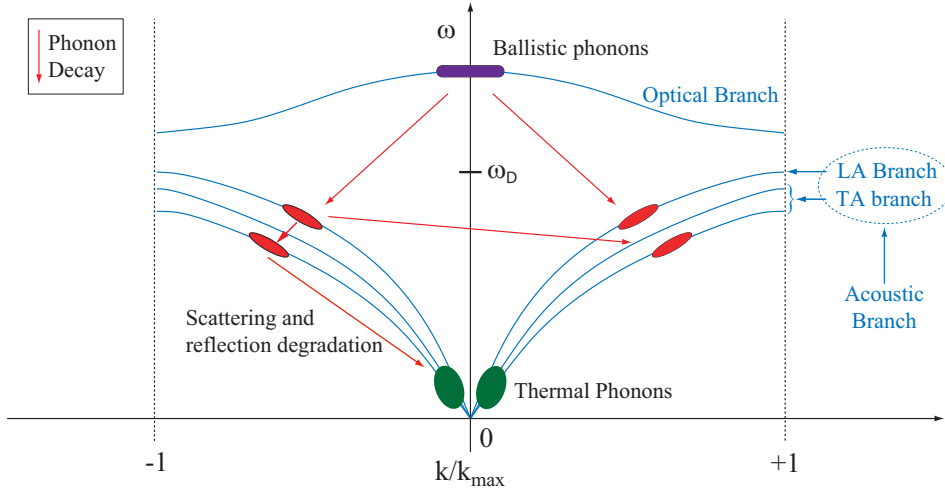
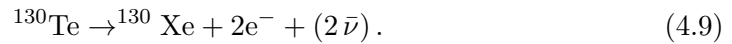


Figure 4.2. Mono-dimensional representation of the phonon dispersion curve.

related to the cryogenic properties of the material. Double beta decay of ^{130}Te occurs through the transition:



The most striking feature of ^{130}Te compared to other $0\nu\text{DBD}$ isotopes is the high natural abundance (see Sec. 3.2). Compared to other materials that usually need to be enriched, the abundance of ^{130}Te allows to build an experiment with natural Tellurium. This is an advantage both in terms of costs and material cleanliness, as enrichment procedures often introduce radioactive contaminations. The transition energy of ^{130}Te ($Q_{\beta\beta} = 2527.518 \pm 0.013 \text{ keV}$ [136]) is not very high. It has been shown in Sec 3.2 that experiments using isotopes with Q -values above 2615 keV are affected by a much lower radioactivity background. However, this transition energy happens to be situated between the peak and the Compton edge of the 2615 keV line of ^{208}Tl which leaves a clean window to look for the signal.

The possibility to use pure tellurium crystals as absorbers was taken into account but it was ruled out mainly because of the poor mechanical properties at low temperatures. Stresses caused by the thermal contractions revealed to produce excessive damages on pure Te crystals. TeO_2 has instead a good mechanical behavior, and has a higher Debye temperature, implying lower specific heat and thus a higher sensitivity to thermal pulses.

4.1.3 The thermal sensor

The phonon sensor is usually a thermistor, a resistive device with a steep dependence of the resistance on the temperature. There are basically two types of thermistors, Transition Edge Sensors (TES) and Semiconductor Thermistors (ST). TES are superconducting films kept at the critical temperature, they have a rather fast response ($\sim \mu\text{s}$) but can only work in a narrow range of temperatures. On the other hand ST have a slower response ($\sim \text{ms}$) but can be used in a wider range of temperatures. A parameter characterizing the sensor is the logarithmic sensitivity

η :

$$\eta = \left| \frac{d \log R(T)}{d \log T} \right|. \quad (4.10)$$

The above expression implies that (apart signs):

$$\frac{dR}{R} = \eta \frac{dT}{T} \quad (4.11)$$

where it is evident that the larger is η the higher is the response of the device. Typical values of η are 10 for ST and 100 for TES. Despite the lower sensitivity, ST have been preferred for CUORE bolometers because of their wider range of operating temperature. In the following, the operating principles of semiconductor thermistor will be presented.

Semiconductors are covalent solids that behave as insulators because the valence band is full and the conduction band is empty, nevertheless the energy gap between valence and conduction band is less than 2 eV. The conduction can then happen only with an activation energy greater than the energy gap. Since at room temperature $kT \simeq 0.025$ eV, the conduction can only happen at higher temperatures. If instead the semiconductor lattice has impurities (extrinsic or doped semiconductors), then new energy levels are introduced slightly above the valence band or below the conduction band, depending on the type of atoms inserted. With this technique the conduction can also happen at lower temperatures.

The dopant concentration determines the behavior of the solid and there is a critical concentration that characterizes the transition from metal to insulator. The region near this concentration is named metal-insulator transition region (MIT) [142], where the material resistivity exhibits a dependence on the temperature.

At temperatures lower than 10 K the conduction is dominated by the migration of the charge carries between impurity sites. In this situation electrons are not localized and the conduction happens when an electron jumps from a donor site to another, without using the conduction band (*hopping mechanism*). This migration is due to the tunnelling through the potential barrier separating the two dopant sites and it is activated by phonons (see figure 4.3). At even lower temperature, the energy of the phonons that are responsible for the conduction mechanism is low and charge carriers migrate also to far impurity sites with free energy levels that are close to the Fermi energy. In this conduction regime, called Variable Range Hopping [143] (VRH), the concentration of minority charge carriers determines the density of states close to the Fermi level. The MIT is set not only varying the concentration of dopant but also varying the ratio of acceptor and donor concentrations. In the VRH conduction regime the resistivity dependence on temperature is described by the law:

$$\rho(T) = \rho_0 \exp \left(\frac{T_0}{T} \right)^\gamma \quad (4.12)$$

where ρ_0 , T_0 depend on the doping concentration and $\gamma = 1/2$.

The expression of the logarithmic sensitivity can be easily derived from the above equation using Eq. 4.10:

$$\eta = \gamma \left(\frac{T_0}{T} \right)^\gamma. \quad (4.13)$$

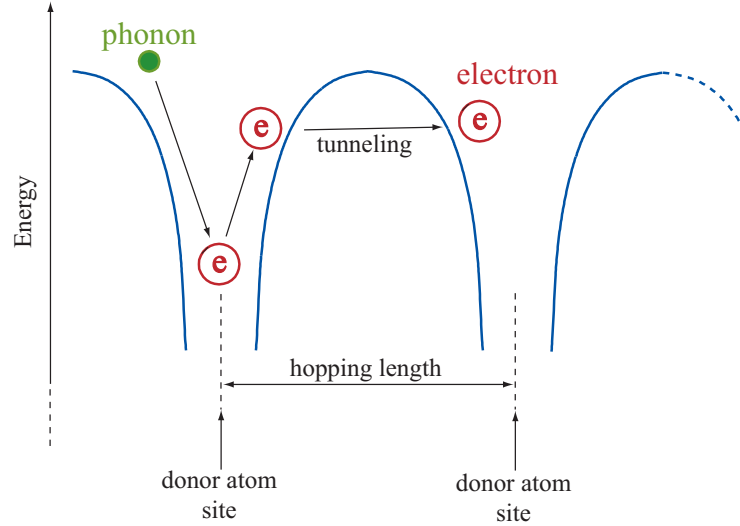


Figure 4.3. Schematic representation of the hopping conduction mechanism.

4.1.4 NTD-Ge thermistors

The thermal sensor used in CUORICINO and CUORE bolometers is a Neutron Transmutation Doped (NTD) germanium thermistor operating in the Variable Range Hopping regime [144]. Melt-doped Ge crystals cannot achieve the necessary uniformity due to the effect of dopant segregation. The only technique available for producing uniform doping is NTD: Ge wafers are bombarded with thermal neutron beams that, inducing nuclear reactions, create donor (As and Se) and acceptor (Ga) impurities. The natural abundances of germanium are such that this doping technique allows to obtain the right dopant concentration, which determines the sensor performances. Wafers are then cut into pieces, each of them is a thermistor and its resistance can be expressed as:

$$R = R_0 \exp\left(\frac{T_0}{T}\right)^\gamma \quad (4.14)$$

where R_0 depends on the geometry and is roughly $R_0 = \rho_0 l/S$, being l and S the length and the section of the piece respectively. The parameters R_0 , T_0 and γ are determined experimentally. The measurement is made coupling the sensor to a low temperature heat sink using an high conductivity epoxy, so that the electrothermal feedback is negligible. The heat sink temperature is then varied (15 – 50 mK) while a steady current flows through the thermistor. Using a calibrated thermometer the parameters can be extracted from a fit to the $R(T)$ characteristic. Typical parameters of CUORE NTD's are:

$$R_0 = 1.15 \, \Omega, \quad T_0 = 3.35 \, \text{K} \quad \text{and} \quad \gamma = 1/2 \quad (4.15)$$

Using these values we can calculate the static resistance (R_S) at the working temperature $T_S = 10 \, \text{mK}$ to be approximately $100 \, \text{M}\Omega$.

4.2 Detector operation

In order to convert the resistance variation into a readable voltage signal, the sensor is polarized by the simple circuit shown in Fig. 4.4(a). A bias current I_B is produced by a voltage generator closed on a load resistance that is put in series with the thermistor. The load resistance R_L is set much bigger than the sensor resistance $R(T)$, so that the bias current can be assumed to be constant. In these conditions a voltage drop $V(T) = I \cdot R(T)$ appears across the thermistor, causing a power dissipation $P = I \cdot V$ on it. This, in turn, produces an increase of the sensor temperature and therefore its resistance is decreased. There is therefore an equilibrium condition when the power dissipated on the sensor equals the heat dissipation toward the thermal bath. Denoting by T_0 the detector base temperature and by G the thermal conductance versus the bath, the equilibrium temperature of the sensor is given by the expression

$$T_{bol} = T_0 + \frac{P}{G}. \quad (4.16)$$

The dependence of the sensor resistance on the dissipated power is depicted in Fig. 4.4(b). Because of the dependence of the resistance on the bias current, the characteristic $I - V$ curve of the detectors deviates from linearity, giving rise to the non-ohmic behavior represented in Fig. 4.5(a). For small values of the bias current the temperature rise produced by power dissipation can be neglected and the $I - V$ curve is almost linear. For bigger values of I_B the slope of the $I - V$ curve starts to increase, until an inversion point is reached, where a further increase of the bias current causes a decrease of the sensor voltage. As represented in Fig. 4.5(a) the working point of the detector can be found by the intersection of the load curve with the load line imposed by the bias circuit: $I_B = (V_B + V_{bol})/R_L$, where V_B is the bias voltage. It is chosen to maximize the signal to noise ratio. As represented in Fig. 4.5(b) this usually corresponds to a bias current at halfway between the end linear range and the inversion point.

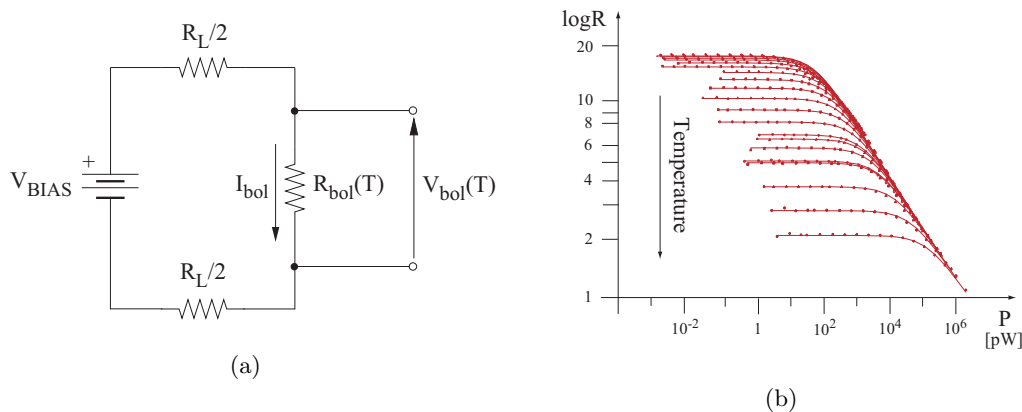


Figure 4.4. Left: electric scheme of the bias circuit used for thermistor readout. Right: dependence of the resistance on the power dissipation for various values of the base temperature. Curves with lower resistance at $P=0$ correspond to higher base temperatures.

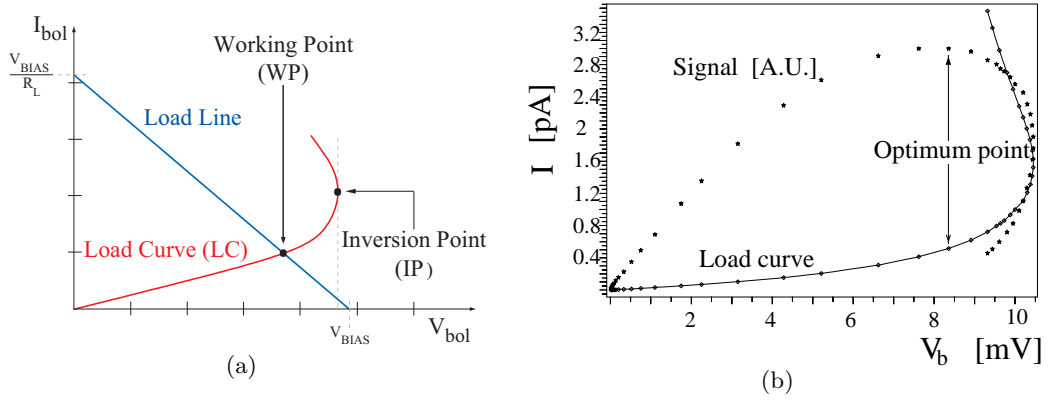


Figure 4.5. Load curve of a semiconductor thermistor. On the left picture the working point is determined by intersection of the sensor characteristic curve with the bias circuit load line. On the right the curve is shown together with the corresponding signal amplitude.

The signal amplitude produced by an energy release E can be estimated as follows. In static conditions the voltage over the sensor is given by

$$V_{bol} = V_B \frac{R_{bol}}{R_L + R_{bol}}. \quad (4.17)$$

The voltage pulse produced by an energy release can be written as

$$\Delta V_{bol} = V_B \frac{R_L}{(R_L + R_{bol})^2} \simeq \frac{E}{CT_{bol}} \eta \sqrt{PR_{bol}} \quad (4.18)$$

where Eq. (4.1) and Eq. (4.10) have been used. This expression vanishes both for $P \rightarrow 0$ and $P \rightarrow \infty$ because the resistance vanishes at high temperatures. A typical pulse produced by a particle interacting in a bolometers is represented in Fig. 4.6.

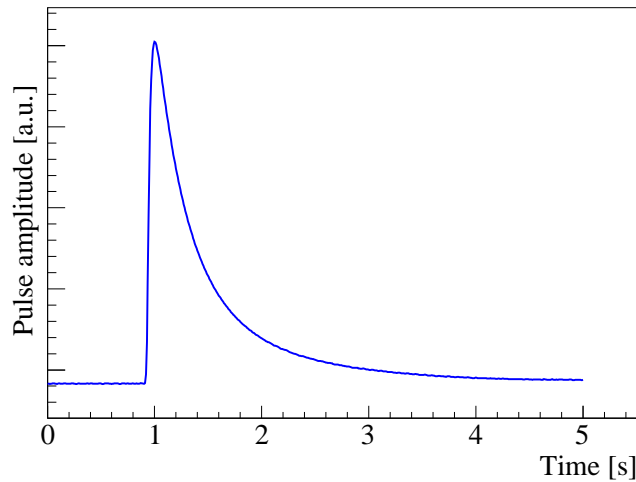


Figure 4.6. Typical pulse shape produced by a particle interacting in a bolometric detector.

Using some numbers relative to the CUORE bolometers, it is possible to have an idea of the magnitude of the produced signal. A typical value for the absorber heat capacity is $C \simeq 10^{-9}$ J/K at 10 mK, thus an energy release of 1 MeV would result in a temperature rise of ~ 0.1 mK. Since the typical voltage drop across the sensor is of few mV in static conditions, the pulse height produced by the energy release of 1 MeV is given by $\Delta V/V \sim \Delta R/R \sim \eta \Delta T/T \sim 100 \mu V$.

4.3 The single module

CUORICINO, CUORE-0 and CUORE detectors have a modular structure, where the basic element is represented by a single floor (see Fig. 3.10). The design of the single module must satisfy stringent requirements concerning mechanical properties, thermal performances and radioactivity constraints. Thermal coupling between the crystals and the heat sink, as well as the ones with the NTD sensors, must guarantee a good performance of the detector. At the same time the geometry of the various parts of the single module must be properly designed, preventing the differential thermal contractions from breaking the crystals or leaving them too loose. All these requirements have to be met by using only those materials that were measured to have low enough radioactive contaminations. A detail of a CUORICINO single module, that in first approximation represents a single CUORE module, is shown in Fig. 4.7. It is composed by four $5 \times 5 \times 5$ cm³ crystals enclosed in a pair of oxygen-free high thermal conductivity (OFHC) copper frames which serve both as mechanical supports and thermal bath for the detectors. The two frames are connected to each other by four small columns, also made of copper. The crystals are connected to the copper frames by small Teflon supports that represent the weak thermal conductance versus the heat sink and compensate the different thermal contractions of TeO₂ and copper.

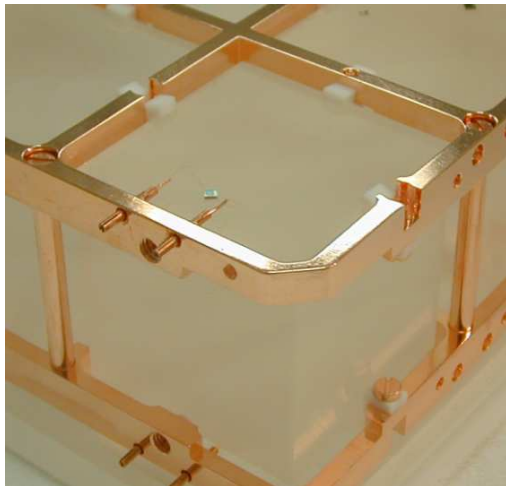


Figure 4.7. Detail of the CUORICINO single module. The crystal is held by OFHC copper frames which also represent the thermal bath for the detectors. In the picture the Teflon holders and the NTD sensor are also visible.

The NTD sensors are attached to the crystals using Araldit Rapid, Ciba Geigy epoxy glue. Since a flat glue deposition would cause the sensor to detach from the crystal surface because of differential thermal contractions, the glue is deposited in nine separate spots, with a diameter of 0.7 mm each (Fig. 4.8). The thermal conductance of the glue spots was measured experimentally and the phenomenological

relation revealed to be $G \simeq 2.6 \times 10^{-4} T^3$ W/K/spot [145], where T is in K. The same gluing technique is used to apply on each detector the Si resistor used to feed the crystal with heater pulses (see Sec. 4.6). In CUORICINO and CCVR runs this operation was performed manually: using a dedicated tool composed by an array of 9 pins, the glue spots were deposited on the NTD surfaces and afterwards the sensors were coupled to the crystals using a spacer to obtain the $50 \mu\text{m}$ gap. However, since this procedure revealed to be time consuming and not appropriate to deal with 1000 crystals, an automatic tool will be employed for the gluing of the CUORE-0 and CUORE bolometers. Besides being faster and more reliable, the new approach will give the possibility to glue the sensors after the entire tower has been assembled. This feature will allow to easily recover possible broken wiring connections and unsuccessful gluings without dismounting the whole tower. Electrical connections for both the NTD sensor and the Si resistor are made with two $50 \mu\text{m}$ diameter gold wires, bonded to metalized surface of the two chips. The wires are crimped on the opposite side into copper pins that pass through the mechanical structure of the single module (see Fig. 4.7).

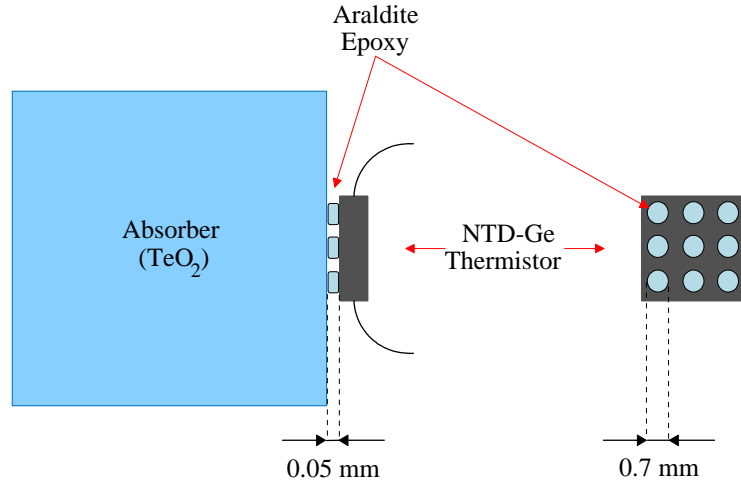


Figure 4.8. Sensor gluing on the TeO_2 crystals. The glue is deposited on the sensor in nine separate spots in order to avoid excessive stress caused by differential thermal contractions between the crystals, the NTD and the glue itself.

4.4 Signal readout

The electrical connection of the bolometric signal from 10 mK to room temperature is divided in two parts. After coming out from the single module, the signal runs along the tower over a twisted pair of wires, until it reaches the mixing chamber. From this point on, the signal is delivered over a pair of twisted coaxial cables: passing through several thermalization stages these wires reach the exterior of the cryostat. These wires are made of constantan, an electric conductor that has the rare property of not conducting heat. The cryostat is finally plugged to the front-end electronic boards through a set of Fisher connectors. The analog part of the readout system performs mainly three operations: thermistor biasing, signal ampli-

fication and signal filtering. The front-end boards contain the biasing circuit and the amplification stages, and their parameters are remotely programmable [146]. As stated in section 4.2, the load resistors must be large compared to the sensor resistance; since the typical thermistor resistance R_{bol} is of order $100\text{ M}\Omega$ at 10 mK , their value is $27\text{ G}\Omega$ each. The bias voltage V_B can be set in the range $0 \div 10\text{ V}$ and for a typical bias $V_B = 5\text{ V}$ the output voltage of the thermistor when no energy is released in the crystal is:

$$V_{bol} = V_B \frac{R_{bol}}{R_{bol} + R_L} \simeq 10\text{ mV}. \quad (4.19)$$

where R_L represent the series of the two load resistors. The signal observed when particles impinge on the detector leads to a voltage variation of about $200\text{ }\mu\text{V}/\text{MeV}$ that in turn is amplified. The gain (G) of the amplifier is then adjusted to fit the energy region of interest into the ADC range with G ranging between 450 and 10000 V/V . The drift current of the amplifier generates an offset voltage that summed to $V_{bol} \cdot G$ can shift the signal out of the ADC range. To correct for this effect an additional offset is added to the output signal.

After the amplification and the offset correction the signal goes through an anti-aliasing 6-pole Bessel Filter with an attenuation of 120 dB/decade and a programmable cutoff ranging between 8 and 20 Hz . Finally the signal is acquired by an ADC (range $[-10.5, 10.5]\text{ V}$, 18 bits) with a typical sampling period of 8 ms (125 Hz). Given the low event rate, it was possible to implement a software trigger. When a trigger is found the signal is recorded in a window of ~ 4 seconds. In order to have an estimate of the bolometer temperature at the time of the pulse, about one second of baseline before the trigger is recorded, leading the total window length to ~ 5 seconds. Selected events are then written to disk for offline processing.

4.5 Detector noise

The thermodynamic fluctuations of the crystal described in section 4.1.1 represent the ultimate noise source because in practical applications they give a negligible contribution compared to the noise coming from the electronics and the cryogenic apparatus. In this section the principal noise sources will be presented. Every resistance R working at temperature T generates a white noise due to the fluctuations of the charge carriers. For load resistors the spectral density can be expressed as:

$$\Delta V_L^2 = 4kT_{R_L} R_L \quad (4.20)$$

that on the output voltage of the bolometer becomes:

$$\Delta V_{bol}^2 = \frac{\Delta V_L^2}{(R_L^2)} \left(\frac{R_{bol} R_L}{R_{bol} + R_L} \right)^2 \simeq 4kT \frac{R_{bol}^2}{R_L}. \quad (4.21)$$

Using the detector typical parameters the above equation translates into a noise of order 300 eV rms . The preamplifier noise is of three types: *series*, generated by the JFET resistances, having a value around 10 eV rms , *series 1/f* that amounts to 15 eV rms and *parallel shot*, that at room temperature amounts to 130 eV rms .

The dominant noise contribution comes from the vibrations of the cryogenic apparatus. These vibrations are transmitted to crystals and wires producing two

different types of noise. The crystal vibrations generate an energy dissipation that in turn changes the temperature. These temperature instabilities have a frequency spectrum similar to the signal one, and then they are the most dangerous source of noise. The wires vibrations change the wire-wire capacitance and the wire-ground capacitance, generating the so called *microphonic* noise.

Quantifying the amount of vibrational noise is difficult, and it strictly depends on the cryogenic setup and on the detector assembly. These vibrations are anyway reduced hanging the detector to the cryostat by means of a spring and mechanically decoupling the cryostat from the outer environment.

4.6 First level analysis

Standard CUORICINO and CUORE data analyses proceed through two steps. First level analysis aims at determining the energy and several pulse shape parameters associated to each raw pulse waveform recorded by the data acquisition system. Starting from these quantities, second level analysis allows to extract the physical informations that are relevant for the scientific goals of the experiment. In this section the first level analysis procedures will be discussed. For a more detailed description of the whole analysis chain, see [147].

The first operation to be performed in offline analysis is the association of an amplitude to each recorded waveform. Since thermal pulses are superimposed to stochastic noise, a simple maximum-minimum algorithm would not give optimal results. Instead the optimum filter (OF) technique is used. Based on the approach described in [148], this algorithm has proven to provide the best estimate of the pulse amplitude and, as a consequence, the best energy resolution. This filter and the issues related to that will be discussed in the next chapter.

After the pulse amplitude has been evaluated using the OF technique, gain instability corrections must be applied to data. In fact, thermal drifts induce variations in the response of the detectors. In order to avoid this kind of instabilities, the tower is maintained at a constant temperature by a feedback stabilization circuit, fed by the signal of a thermometer that is attached on the mechanical structure of the detector [149]. However, fine gain drift corrections are mandatory. Thermal instabilities are hence corrected by exploiting the fixed energy thermal pulses that are injected every few minutes in the crystals [150]. These stabilization signals are generated by dissipating an electrical pulse of fixed energy on a Si resistor attached to each energy absorber. They have a time duration much shorter than the typical thermal response of the detector, and the produced signals have a shape that is almost indistinguishable from the ones produced by particle interactions. These signals, usually called heater pulses, are flagged by the data acquisition system. A typical trend for the reference pulse amplitude as a function of the detector baseline (which is in turn a function of the detector base temperature) before and after gain instability corrections is shown in Fig. 4.9. The relation $\Delta V(V_{base})$ between the heater pulse amplitude and the baseline value is found by a fit on the left plot in the figure. The gain correction factor is then obtained as

$$\alpha(V_{base}) = \frac{\Delta V^{ref}}{\Delta V(V_{base})} \quad (4.22)$$

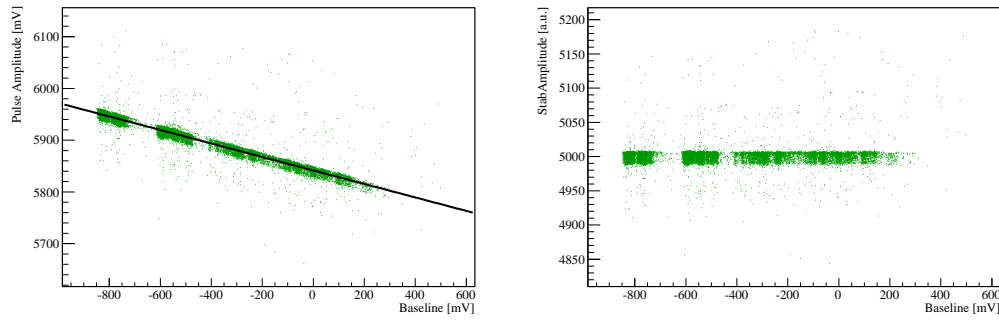


Figure 4.9. Heater pulse amplitude as a function of the detector baseline before (left) and after (right) gain instability corrections. Stabilized heater amplitudes are usually reported to the nominal amplitude of 5000. This arbitrary scaling factor is eliminated when pulse amplitudes are converted into energy values.

where $\Delta V^{ref} \equiv \Delta V(V_{base}^{ref})$ and V_{base}^{ref} can be arbitrary chosen. Assuming that the gain correction factor is the same for all energies, it can be used to adjust the amplitudes of all pulses.

The final step of first level analysis is the conversion of the stabilized amplitudes into the corresponding energy values. Detector energy calibration is performed about once per month by inserting a ^{232}Th source in proximity of the detector, between the cryostat and the external lead shields. Pulse amplitude spectra (Fig. 4.10) from calibration measurements show several γ peaks that are not visible in standard background measurements, because of the low radioactivity content of the detector materials. A polynomial fit is applied to these peaks to obtain a $E(\Delta V)$ conversion curve that is then applied to background measurements to obtain the corresponding energy spectra. Background measurements between two consecutive calibrations are usually grouped into a data set. A check is performed to ensure that the energy conversion curves $E(\Delta V)$ obtained from the two calibrations performed before and after each data set are compatible with each other.

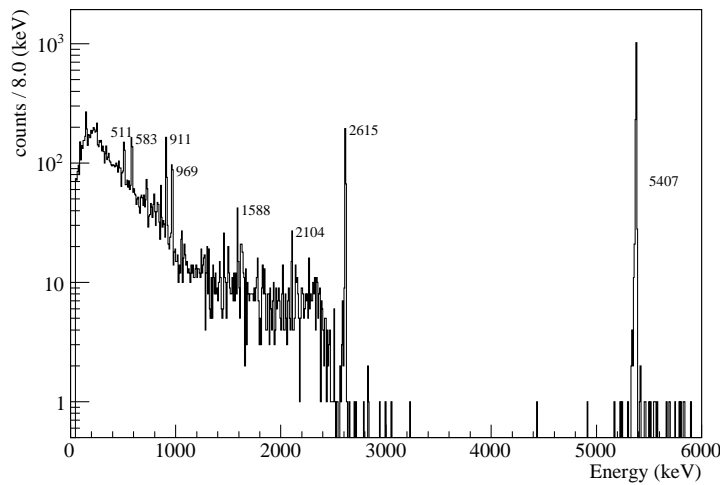


Figure 4.10. Typical energy spectra obtained in a few days calibration in a CCVR run.

Chapter 5

A new trigger for CUORE low energy analyses

The Optimum Filter algorithm proved to be a powerful amplitude and pulse shape estimator in high energy analyses. Its application to data maximizes the signal to noise ratio, increasing the resolution. Fake signals, pile-up's, and spikes are easily discarded by pulse shape parameters based on this filter. The trigger we developed is based on the Optimum Filter, that is applied to the continuous flow of the data. In this section the mathematical expression of the filter is reviewed and the method we use to filter the data is described. Finally the Optimum Trigger and the pulse shape algorithms will be developed, tuning their features on the characteristics of the filtered data. As anticipated in Sec. 3.3.4, the Optimum Trigger and the other algorithms developed were tested on the CCVR2 detector.

5.1 Optimum Filter algorithm

The Optimum Filter algorithm allows to estimate the amplitude A of a signal maximizing the signal to noise ratio. The filter expression will be derived making the following assumptions:

- The detected signal $y(t)$ can be parametrized as

$$y(t) = A s(t) + n(t) \quad (5.1)$$

where $s(t)$ is the time evolution of the signal, A is the signal amplitude, and $n(t)$ is the noise of the apparatus.

- The shape of $s(t)$ is independent of A and known.
- The noise $n(t)$ is stationary and its power spectrum, $N(\omega)$, is known. The power spectrum is defined as

$$N(\omega) = \langle n(\omega)n(\omega^*) \rangle \quad (5.2)$$

where $n(\omega)$ is the Fourier transform of $n(t)$ and $\langle \rangle$ denotes the expectation value.

In the following we will first derive the filter for the case of the white noise, and then for the general case of any form of noise power spectrum. The derivation will be made for sampled data so that Eq. (5.1) can be rewritten as:

$$y_i = A s_i + n_i \quad (5.3)$$

where i is the sample index.

5.1.1 White Noise case

A white noise power spectrum corresponds to Gaussian and uncorrelated fluctuations in the time domain. We want to find the filter that, as a function of the displacement j , maximizes the likelihood

$$L_j(y_i|A_j) = \prod_i \frac{1}{\sqrt{2\pi}\sigma} \exp \left[-\frac{(y_i - A_j s_{i-j})^2}{2\sigma^2} \right] \quad (5.4)$$

where σ is the noise rms and the product extends over the length of y_i . For each shift j we have to maximize $L_j(y_i|A_j)$:

$$\frac{d}{dA_j} L_j(y_i|A_j) \propto \sum_i (y_i - A_j s_{i-j}) s_{i-j} = 0 \quad (5.5)$$

that leads to:

$$\hat{A}_j = \frac{\sum_i y_i s_{i-j}}{\sum_i s_{i-j}^2} = \frac{\sum_i y_i s_{i-j}}{\sum_l s_l^2}. \quad (5.6)$$

The filtered signal y'_i corresponds to \hat{A}_i . Equation (5.6) can be rewritten in terms of the convolution

$$y'_i = y_i \otimes K_i \quad (5.7)$$

where

$$K_i = \frac{s_{-i}}{\sum_l s_l^2} \quad (5.8)$$

is the “kernel” of the filter. The filter leaves the amplitude of the pure signal, s , unmodified and the noise rms is reduced to:

$$\sigma'^2 = \sigma^2 / \sum_l s_l^2. \quad (5.9)$$

From Eq. 5.6 it turns out that the filtered amplitude of the pure signal, s , is maximum and equal to 1 when $j = 0$. Filtered signals will be delayed by $-i_M$, where $-i_M$ is the maximum position of s . To align the maxima of the original signal and of the filtered one, the filter kernel K_i can be shifted by $-i_M$.

The convolution in Eq. 5.7 can be expressed in the frequency domain as:

$$y'(\omega_k) = y(\omega_k) \cdot K(\omega_k) \quad (5.10)$$

that including the maxima alignment becomes

$$y'(\omega_k) = y(\omega_k) \cdot K(\omega_k) e^{-j\omega_k i_M}. \quad (5.11)$$

From the above expression we obtain the transfer function of the filter:

$$H(\omega_k) = K(\omega_k) e^{-j\omega_k i_M} = \frac{1}{E_s} s^*(\omega_k) e^{-j\omega_k i_M} \quad (5.12)$$

where we defined the energy of the signal s as $E_s = \sum_l s_l^2$.

5.1.2 Generalized case

When the noise is not white we cannot use directly the filter developed in the previous section, because the noise is correlated and the elements of the product in Eq. (5.4) are not independent. However if we apply to the noise the filter

$$W(\omega_k) = \frac{1}{n(\omega_k)} \quad (5.13)$$

the noise will be “whitened”, Eq. (5.4) becomes valid, and the filter in Eq. 5.12 can be applied. The filter W has to be applied to the y signals, that contain the pure signals and the noise. The shape of the signal is then modified into $s(\omega_k)/n(\omega_k)$, and the transfer function in Eq. 5.12 becomes

$$H(\omega_k) = h \frac{s^*(\omega_k)}{n^*(\omega_k)} e^{-j\omega_i M} \frac{1}{n(\omega_k)} = h \frac{s^*(\omega_k)}{N(\omega_k)} e^{-j\omega_i M} \quad (5.14)$$

where h is a constant factor that leaves unmodified the amplitude of s at the filter output:

$$h = 1 / \sum_k \frac{|s(\omega_k)|^2}{N(\omega_k)}. \quad (5.15)$$

The noise power spectrum at the filter output will be:

$$N'(\omega_k) = h^2 \frac{|s(\omega_k)|^2}{N(\omega_k)} \quad (5.16)$$

and the rms:

$$\sigma'^2 = \sum_k N'(\omega_k) = h \quad (5.17)$$

If the input noise power spectrum is white,

$$N(\omega_k) = \sigma^2 \cdot M \quad (5.18)$$

where M is the window length, Eq. 5.17 reduces to

$$\sigma'^2 = \sigma^2 \frac{M}{\sum_k |s(\omega_k)|^2}. \quad (5.19)$$

Using the Parseval identity the above equation is equal to Eq. 5.9.

5.1.3 The DFT convolution wraparound

The application of the Optimum Filter defined in Eq. (5.14) relies on the discrete convolution theorem, that we implicitly used to derive Eq. 5.10 from Eq. 5.7. The discrete convolution theorem is this: if a signal s_i is periodic with period M , then its discrete convolution with a kernel H_i of finite duration M is a member of the discrete transform pair:

$$\sum_{j=0}^{M-1} s_{i-j} H_j \iff s(\omega_k) \cdot H(\omega_k). \quad (5.20)$$

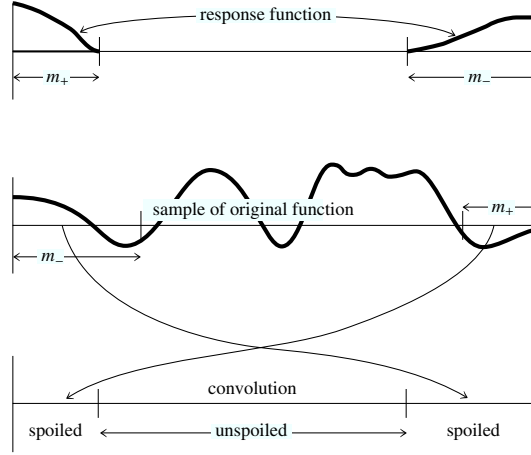


Figure 5.1. The wraparound problem in convolving finite segments of a function. Not only must the response function be viewed as cyclic but so must the sampled original function. Therefore a portion at each end of the original function is erroneously wrapped around by convolution with the response function. Picture taken from [151].

We have to satisfy two conditions to filter the data. First the signal s_i has to be periodic, second the length of the filter H_i should be equal to that of s_i . The second condition is easy to satisfy, padding the response function with zeros. The first is due to the fact that Discrete Fourier Transform (DFT) algorithms operate on finite length data samples, and assume that the window to be filtered is periodic (the DFT frequency spectrum is the spectrum of an infinite repetition of the input window). If the input data are not periodic the convolution will falsely pollute the left side of the window with data from the right side and vice-versa, and the size of the unspoiled part will be equal to the number of zeros in the response function (see Fig. 5.1).

To satisfy these conditions we built the transfer function following these steps:

1. Build the Optimum Filter transfer function $H(\omega_k)$ of length M using the signal s_i and the noise power spectrum $N(\omega_k)$, both of length M .
2. Transform $H(\omega_k)$ in the time domain using DFT, obtaining the kernel H_i of length M .
3. Insert M zeros in the middle of H_i , obtaining the kernel H_i^d of length $2M$.
4. Smooth H_i^d in proximity of the zero insertion, obtaining the smoothed kernel H_i^{ds} .
5. Transform H_i^{ds} in the frequency domain, obtaining the final transfer function $H^{ds}(\omega_k)$, of length $2M$.

The smoothing of H_i^d is needed to avoid the Gibbs phenomenon [152]: if H_i^d is not zero where the zeros will be inserted, a discontinuity will be created, introducing fake oscillations in its DFT. When filtering a data sample of length $2M$, the first and the last $M/2$ samples will be spoiled, while the M middle samples will be correctly filtered (see Fig. 5.2).

The continuous data flow is processed filtering windows of length $2M$ overlapped by M and taking the M middle samples of each window as output (see Fig. 5.3).

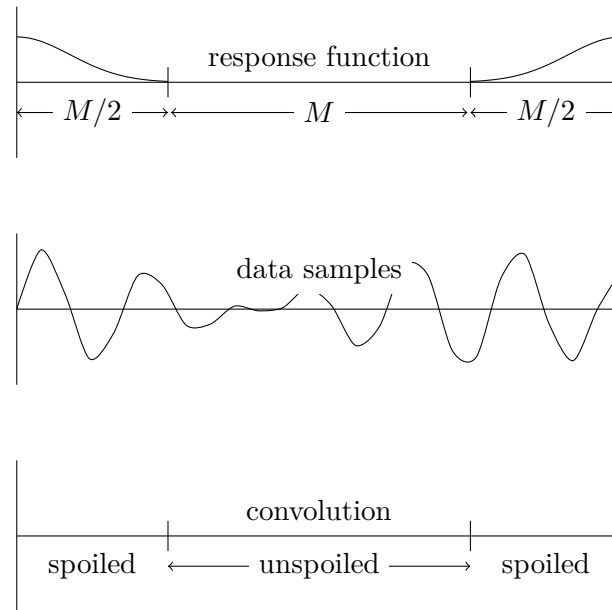


Figure 5.2. Padding of the filter kernel. To avoid the DFT wraparound problem the original kernel is padded in the middle with a number of zeros equal to its length. In this way the product of the response function DFT and of the data samples DFT produces a correct convolution in correspondence of the response function zeros.

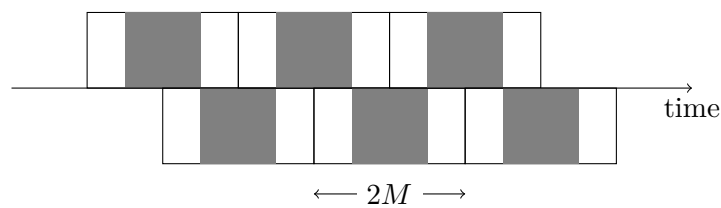


Figure 5.3. Filtering of the continuous data flow. Each window has size $2M$ (white rectangle), and the M middle samples are correctly filtered (gray rectangle). The windows are overlapped by M , such that middle samples of each window are concatenated.

5.1.4 Filter implementation

We built the transfer function $H^{ds}(\omega_k)$ using as s_i and $N(\omega_k)$ the average pulse and the noise power spectrum of the official CCVR2 data analysis (see appendix A), that are shown in Fig. 5.4. The kernel H_i and the zero-padded version are shown in Fig. 5.5. As stated in the previous section, the connection between the kernel and the zeros should be smooth to avoid oscillations in the frequency domain. This correction has been implemented applying a cosine smoothing to the edges of the kernel. The first half of H_i^d has been transformed as

$$H_i^{ds} = H_i^d \quad i < M/2 - L \quad (5.21)$$

$$H_i^{ds} = \frac{H_i^d}{2} \left[1 + \cos \left(\frac{\pi}{L} (i + 1 - (M/2 - L)) \right) \right] \quad M/2 - L \leq i < M/2 \quad (5.22)$$

$$H_i^{ds} = H_i^d = 0 \quad i < M \quad (5.23)$$

where L is the half-period of the cosine and $2M$ is the length of H_i^d . The right half of H_i^d has been transformed with the same function, but mirrored. The effect of the smoothing, using $L = 30$, is shown in Fig. 5.6. Transforming H_i^{ds} into the frequency domain, the transfer function $H^{ps}(\omega_k)$ can be applied to the data.

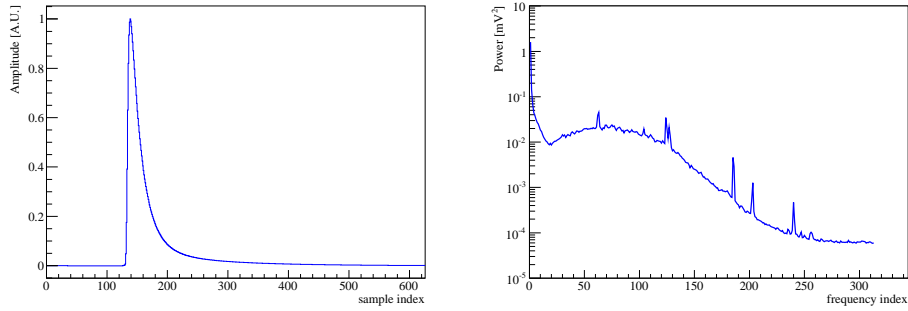


Figure 5.4. Average pulse (left) and noise power spectrum (right) of the official CCVR2 data analysis, channel 3. The length of the acquisition window is 626 samples, corresponding to 5.008 s.

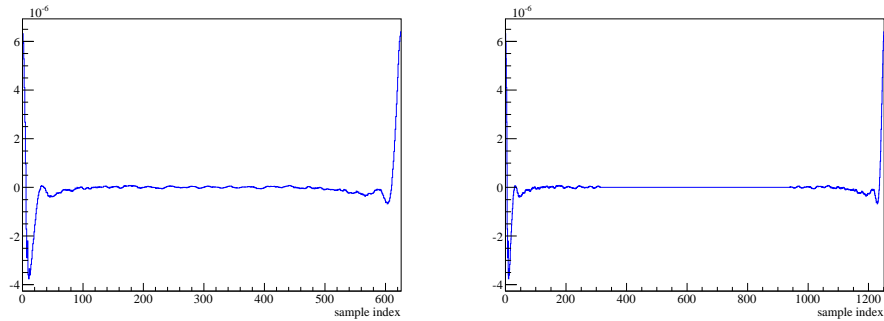


Figure 5.5. Kernel H_i of the Optimum Filter of channel 3, original (left) and zero-padded (right).

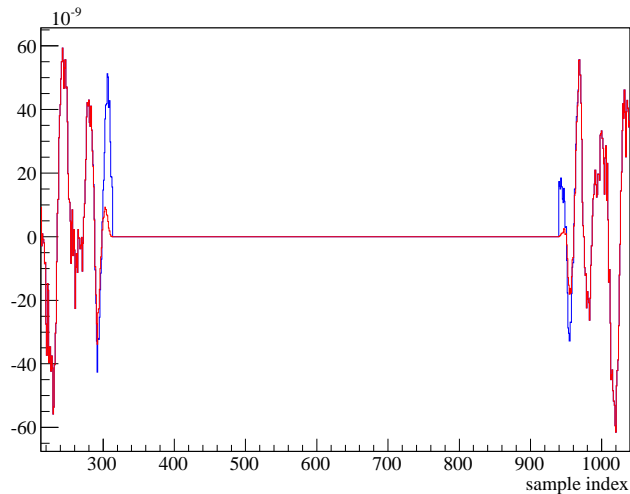


Figure 5.6. Smoothing of the kernel H_i^d with a half-period cosine function. Original (blue) and smoothed (red) kernels of channel 3.

To check the response to the signal, the filter has been applied to the average pulse. Since it is M samples long and the filter is $2M$ samples long, the average pulse has been enlarged for this purpose. In the left part, $M/2$ zeros has been added. In the right part, an exponential decay $M/2$ samples long has been added. The parameters of the exponential decay have been estimated from the tail of the pulse, such that the added samples represent an ideal extension of the pulse. The filtered average pulse is shown in Fig. 5.7. It is shorter than the original, has an almost symmetric shape and zero baseline. These features have been used to implement the trigger algorithm described in the next sections.

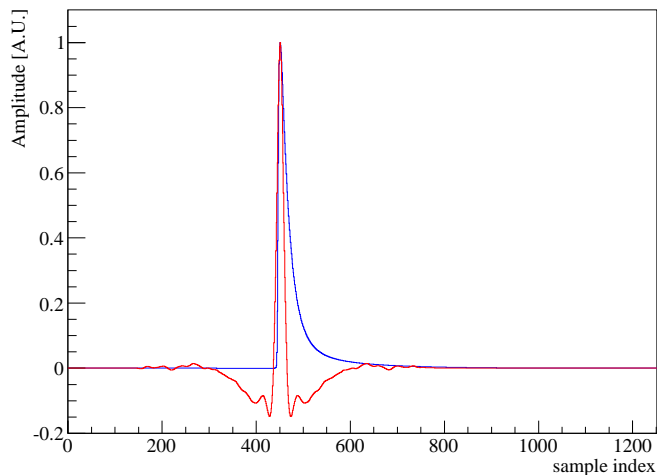


Figure 5.7. Original (blue) and filtered (red) average pulse of channel 3.

5.2 Optimum Trigger

The CUORE DAQ system saves on disk both the triggered data and the continuous output of the DAQ boards. The continuous data can be re-processed with user-defined configurations, saving a new set of triggered data. We implemented the Optimum Filtering technique in CUORE DAQ, and we added a new trigger tuned on the characteristics of the filtered signal and noise.

Some slices of the filtered data are shown in Fig. 5.8 and exhibit the following features:

1. The noise fluctuations are reduced.
2. The low-frequency components of the baseline are suppressed.
3. The baseline has zero mean.
4. The filter is sensitive to the shape of the expected signal and different shapes are highly suppressed.

Signals are triggered requiring that the data samples exceed a positive threshold, and a new trigger is possible when the data samples return below threshold, or after that a local maximum is found. Local maxima are searched within a moving window

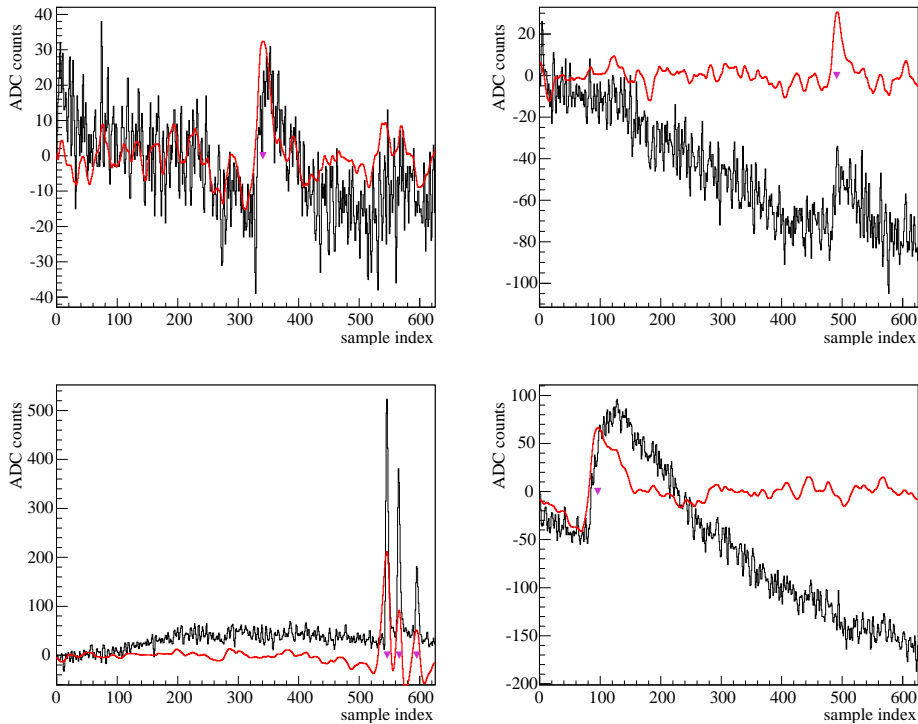


Figure 5.8. Windows with signals, channel 3. The original data (black) has been shifted such that the first sample has zero amplitude, the filtered data (red) are not modified. Top left and top right: 3 keV pulses; bottom left: spikes; bottom right: “triangolone”. The Optimum Filter removes the baseline drifts, and suppress signals with different shape.

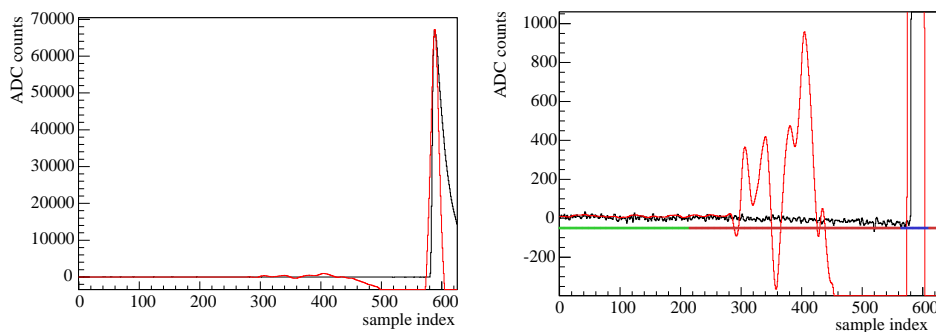


Figure 5.9. Filtering of a high amplitude pulse (5407 keV α on channel 3). When a high energy pulse occurs (left) the side lobes of the filtered signal exceed the threshold, and fake signals could be triggered. To avoid this, the region corresponding to the lobes are vetoed, and no fake trigger is saved. In the right picture: the left lobe of the pulse, the trigger allowed region (green), the vetoed region (red) and the high energy signal region (blue).

that opens when the data exceed the threshold. The window length is fixed and it moves until a local maximum is found. In this way pile-up's are triggered until they are separated by at least the window width. The threshold θ is defined in terms of number of sigma of the filtered noise, that is known a priori (see Eq. 5.17). The width of the window is set upon the filtered average pulse, defined as its full width half maximum (see Fig. 5.7).

When a local maximum is found the trigger fires. Its position is then shifted back with respect to the maximum position, so that it lies in the middle of the rise of the pulse. This operation is needed since in the data analysis the trigger is expected to lie before the maximum of a signal. The size of the shift back is fixed and it is estimated as the time difference between the middle of the rise and the maximum of the non-filtered average pulse. The triangles in Fig. 5.8 show the found triggers and their positions, using a 4.5σ threshold.

The Optimum Filter dramatically simplifies the implementation of trigger algorithms, nevertheless there is a drawback. When high energy pulses are triggered, a set of secondary pulses is seen (see Fig. 5.9). This is due to the fact that the filtered pulse has two symmetric lobes above zero, that would be marked as signal by the trigger. This problem has been solved as follows. The amplitude above zero of the side lobes is a constant fraction α of the amplitude of the main lobe, and can be estimated from the filtered average pulse. When a signal with amplitude $A > \theta/\alpha$ is triggered, the data samples corresponding to the expected positions of the side lobes are vetoed, and no trigger is allowed (see Fig. 5.9). This phenomenon is an important source of inefficiency in CCVR runs, since the ^{210}Po contaminations are high and the amount of vetoed time is dominated by the rate of the 5407 keV α line. When crystals are sufficiently aged (*e.g.* CUORICINO), the background rate is so low that the vetoed time is negligible.

5.3 Pulse Shape

As previously stated, the Optimum Filter is sensitive to pulses having the same shape of the signal. When a pulse with different shape occurs, its filtered amplitude is suppressed and the filtered shape also is different from the expectation. To suppress fake signals we implemented a pulse shape indicator in the trigger code. This indicator is not used to determine the presence of a signal, but is used in the data analysis.

The algorithm is relatively simple. A triggered pulse is fitted using a cubic spline of the filtered average pulse, and the χ^2/ndf of the fit is used as shape indicator. The cubic spline is needed to have a continuous function, and to fit fractional time delays. The fitted parameters are the amplitude and the position of the pulse, while the baseline is fixed at zero. Since the Optimum Filter is already a fit of the data samples, this fit only serves to remove the digitization effects and to estimate the χ^2 . Before fitting, the maxima of the fit function and of the triggered pulse are aligned. The pulse position is then varied in the range $[-1, 1]$ samples, that is the maximum shift due to the digitization. The amplitude is varied in the range $[A, A(1 + \epsilon)]$, where A is the amplitude of the filtered signal and ϵ is the maximum allowed spread in amplitude due to the digitization. This parameter is estimated from the filtered average pulse, computing the amplitude difference between the maximum (that has unitary amplitude) and the amplitude of the point right after. A set of fits is shown in Fig. 5.10 for pulses of different energies and shapes. The fit range L corresponds to four Filtered Average Pulse Width (FAPW).

Finally, the shape indicator is computed as:

$$\chi_{OT}^2 = \sum_{i=0}^{L-1} \frac{(y_i - f_i)^2}{\sigma_L^2(L-2)} \quad (5.24)$$

where y is the filtered signal, f is the estimated fit function, and σ_L is the amount of noise expected in a window of length L . The error of each point, in fact, is not the average error of the entire filtered window in Eq. 5.17, but it is lower since low frequencies are not seen in a smaller window:

$$\sigma_L^2 = \sum_{k=M/L}^{M-M/L} h^2 \frac{|s(\omega_k)|^2}{N(\omega_k)}. \quad (5.25)$$

It must be noticed that, even if Eq. (5.24) has the form of a χ^2 it does not follow a true χ^2 distribution. The expected value is still 1, but the variance is not $2/(L-2)$ since the errors are correlated at the filter output.

The trigger and the pulse shape algorithms that we developed take advantage of the informations that can be extracted from the Optimum Filter theory. All the parameters are fixed and automatically calculated at the DAQ start. In Tab. 5.1 the relevant trigger and pulse shape parameters for all CCVR2 channels are reported.

Compared to traditional algorithms this trigger is more powerful but requires the knowledge of average pulse and noise power spectrum of each channel. It cannot be used at the beginning of the data taking, since at least a long measurement is needed to estimate the average pulse and the noise power spectrum. After this first ‘‘calibration’’, it can be used as standard trigger, without the continuous data reprocessing.

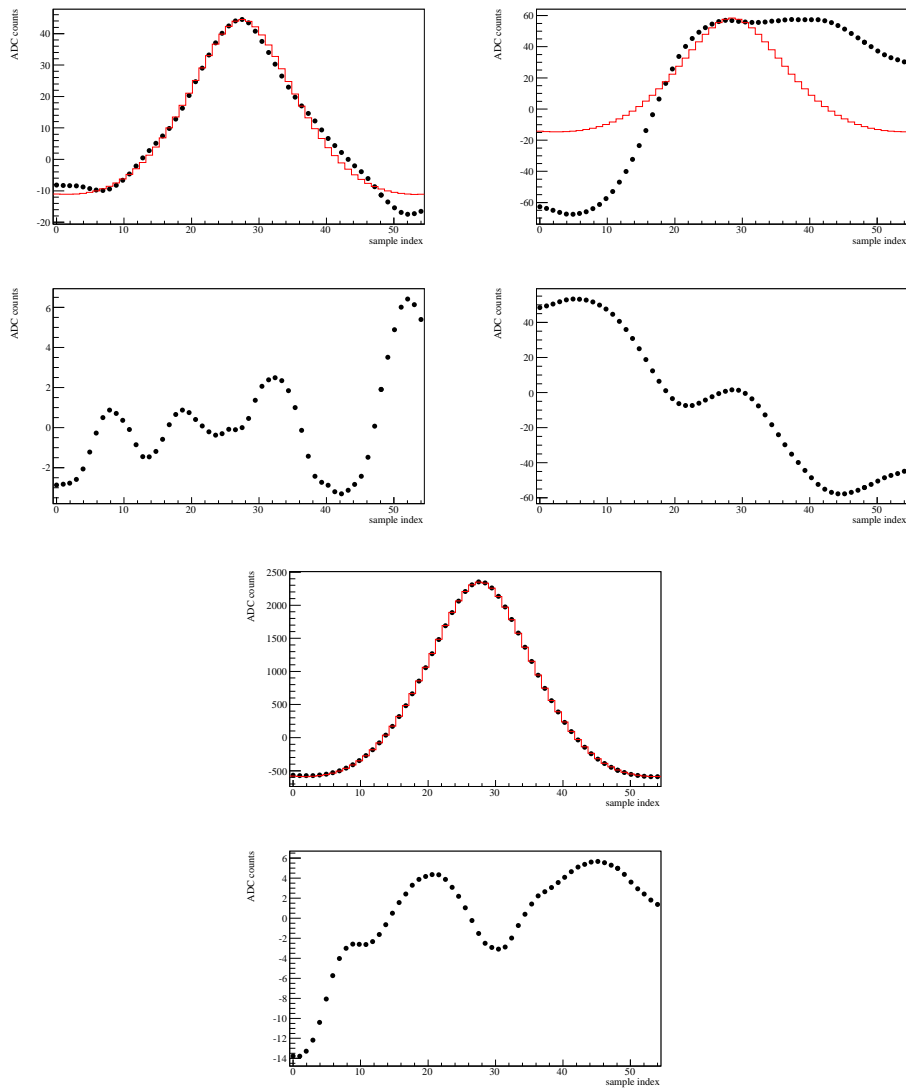


Figure 5.10. Fits of different pulses of channel 3, data and residuals in black, fit function in red. Top left: an event in the 3-4 keV region, $\chi^2_{OT} = 0.5$. Top right: another event in the 3-4 keV region, $\chi^2_{OT} = 132$. Bottom: a 200 keV event, $\chi^2_{OT} = 2.3$.

Table 5.1. Trigger and χ^2_{OT} parameters for the CCVR2 channels

channel	σ_{OF} [keV]	Threshold (number of sigma)	FAPW (samples)	Total Veto Length (seconds)	Fit length (samples)
1	1.72	4.5	12	4.016	48
2	1.65	4.5	16	5.776	64
3	0.34	4.5	14	5.424	56
4	0.52	4	18	6.096	72
5	0.99	2.5	22	5.456	88
6	0.41	3.5	20	7.232	80
7	0.44	4.5	16	5.360	64
8	0.45	4.5	18	4.960	72

5.4 Trigger efficiency

The trigger described in the previous section has been designed to lower the threshold of the CUORE bolometers down to the few keV region. In analyses studying higher energy spectra the trigger efficiency can be evaluated on the single, high energy, heater line, and can be extended to the entire range of interest. At very low energies the situation is different. The noise could significantly lower the pulse amplitude such that the trigger does not fire. Noise pulses and pile-up's could move the estimated energy out of the Gaussian resolution. Moreover the dead time introduced by the trigger veto reduces the detection capability. All these effects can be collected in a unique efficiency parameter, that is the probability of detecting an event and estimating its correct energy. In this section the detection efficiencies are evaluated, using a N-pulses run (see below) and Montecarlo simulations of the bolometer response.

5.4.1 Low Energy Scan with Heater Pulses

An energy scan with the external heater was performed at the end of CCVR2 run, with sequences of 19 pulses from the keV region up to few MeV (see spectrum in Fig. 5.11). The time interval between two consecutive heater pulses was 25 s, and the pulses were flagged by the DAQ. This so-called 'N-Pulses' run lasted 2 days. A dedicated calibration with external ^{232}Th source was then performed. It lasted 2 days.

Continuous raw data were reprocessed offline with the Optimum Trigger and were analyzed using the data-analysis chain described in section 6.1, focusing the attention on the region below 100 keV. Comparing the trigger output with the DAQ heater flag, each pulse was considered detected if:

1. The trigger fired on a data sample in a time window that goes from 20 samples before the flag to 30 samples after.
2. The energy obtained from the Optimum Filter amplitude is compatible with the energy expected for the specific heater pulse.

In order to verify this last condition, single channel energy spectra of events related to each particular heater amplitude were considered. In each spectrum there was a single peak and some outliers in which Optimum Trigger failed to assign the correct amplitude, due to noise fluctuations or pile-up phenomena. Using the Optimum Filter theoretical resolution, all the events not included in a 2FWHM energy window, centered in the mean energy of the peak, estimated by means of a Gaussian fit, were flagged as not triggered. The detection efficiency was estimated as the ratio of the events within this energy window and the total number of fired heater pulses at that energy. The measured efficiency as a function of energy for channel 3 is shown in Fig. 5.12, where it can be seen that it increases with energy, and quickly becomes constant and equal to about 90%. This 10% efficiency loss, that appears also using the CCVR2 standard trigger (see Appendix D), is compatible with the dead time due to the ^{210}Po α line rate.

Particle events have different shape of heater events. Since the optimum filter is built using the signal shape, the heater amplitude estimation is biased. The amount

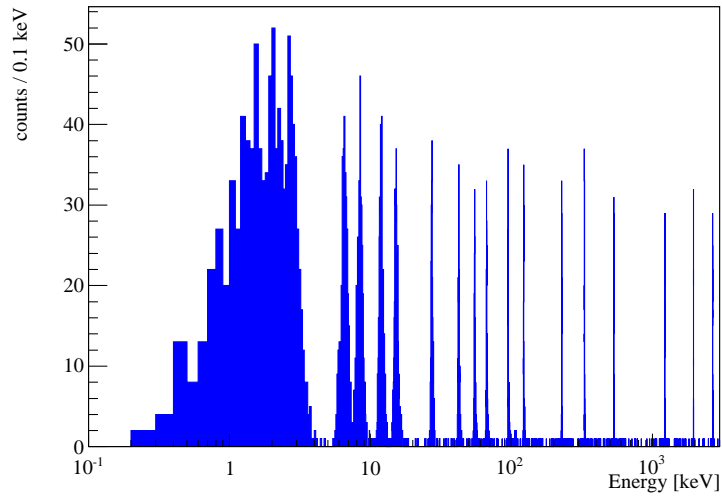


Figure 5.11. Energy spectrum of the N-Pulses run, channel 3.

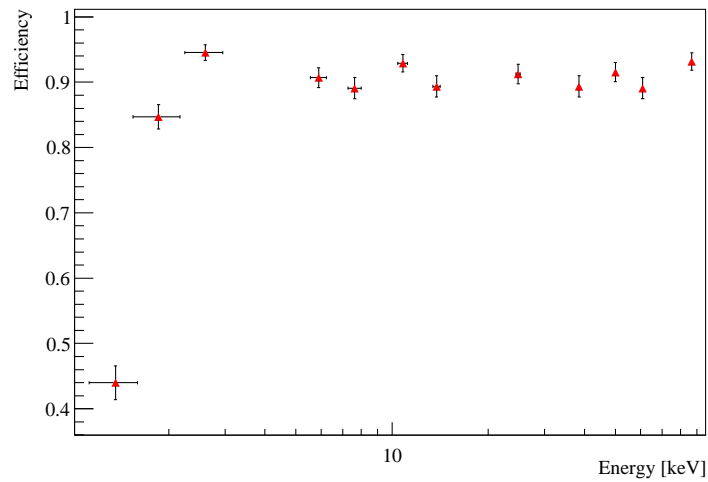


Figure 5.12. Optimum Trigger efficiency on CCVR2 channel 3 computed on N-Pulses measurement. The efficiency increases with energy, quickly reaching a constant value.

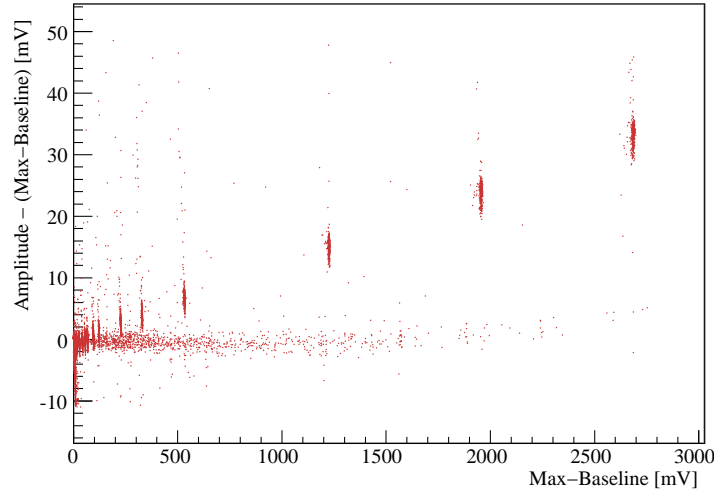


Figure 5.13. Amplitude estimation bias on heater events. The bias of the optimum filter amplitude is evaluated with respect to the unbiased estimator Maximum-Baseline.

of this bias can be quantified comparing the optimum filter amplitude with an estimator that is not sensitive to the signal shape, for example (Maximum-Baseline). The plot in Fig. 5.13 shows that the amplitude bias is constant and amounts to $\sim 1\%$. Given that the optimum filter resolution is of order $1 \text{ keV } \sigma$ (see Tab 5.1), the bias has negligible effect in the low energy region, and heater pulses behaves like particle pulses.

In the next section we validate the efficiency estimation with the heater using simulations, that also allow to infer the efficiency on the two crystals without pulser.

5.4.2 Montecarlo evaluation and validation

Two dedicated Montecarlo runs were performed, using the method described in [153]:

1. A run with simulated heater pulses, generated with a flat spectrum between 1 keV and 50 keV , intended to validate the Montecarlo. The time interval between two consecutive heater pulses was 25 s , like in the N-Pulses measurement. Only the four channels with heater have been simulated.
2. A run with simulated particle pulses, generated with a flat spectrum between 1 keV and 50 keV , intended to evaluate the particle efficiencies. The time interval between two consecutive pulses was 25 s , like in the N-Pulses measurement. All the eight CCVR2 channels have been simulated.

Both Montecarlo runs included simulated noise, generated from Noise Power Spectrum of N-Pulses measurement, and particle events background, randomly generated from the CCVR2 energy spectrum and the measured event rate.

Simulated data were processed with the Optimum Trigger and then analyzed in the same way of the N-Pulses measurement. It's important to underline that results in the lowest energy region are not truthful, because of a bias of the Optimum Trigger Amplitude (Fig. 5.14). In each channel, this region was not considered in the final

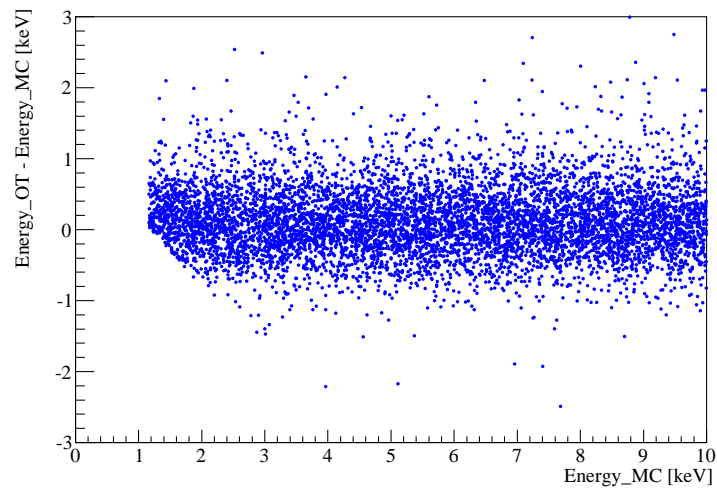


Figure 5.14. Difference between measured and true energy as a function of the true energy, simulation of channel 3.

Below 3 keV the distribution is not symmetric around zero, because negative noise fluctuations push the pulse amplitude below the threshold. Therefore, in this region the energy is biased and related data are discarded.

efficiency evaluation (see Tab. 5.2).

The simulations of heater pulses were compatible on all the four channels, validating the Montecarlo (see Fig. 5.15). The efficiencies on Montecarlo particles are shown in Fig. 5.16. The pattern is very similar to that of heater pulses, demonstrating that the Optimum Trigger acts in the same way on particle and on heater events. This feature is common to all four channels. Optimum Trigger efficiencies were then evaluated on the four channels without heater using the Montecarlo. For each

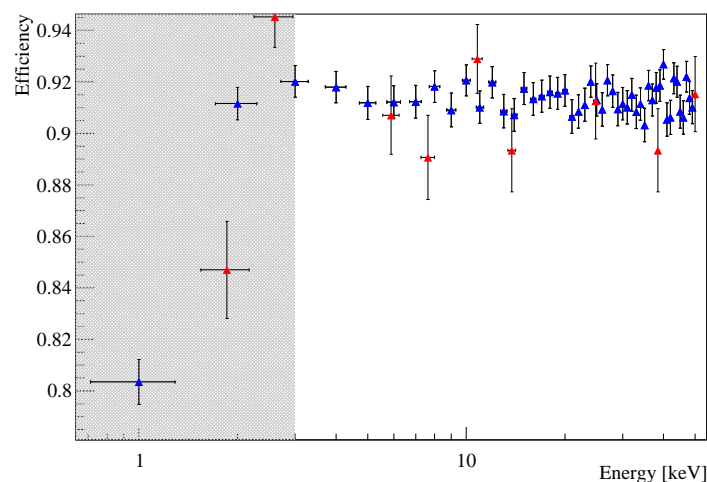


Figure 5.15. Optimum Trigger efficiency on CCVR2 channel 3: N-Pulses data in red, MC heater in blue. The gray region is discarded due to amplitude estimator bias.

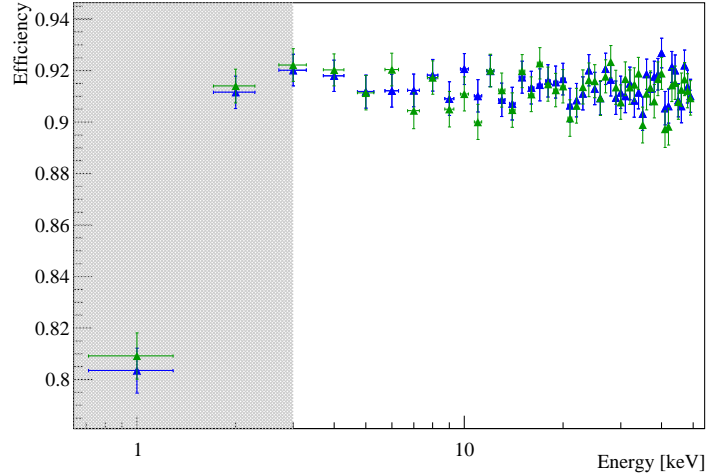


Figure 5.16. Optimum Trigger efficiency on CCVR2 channel 3: MC particle in green, MC heater in blue. The gray region is discarded due to amplitude estimator bias.

channel we evaluated the biased amplitude region, that should be considered as the effective threshold, and the plateau efficiency, computed as the weighted average of each point in the plateau. Final results are summarized in Tab. 5.2.

The data above the biased region will be taken into account for the data analysis, using the efficiencies estimated on the Montecarlo. However it must be noticed that estimations have been made on the N-pulses run. This run has conditions similar to the background runs, but in principle not equal. In the future, efficiency should be constantly monitored with a set of low energy pulses, to ensure that it is correctly evaluated on each background run.

Table 5.2. Optimum Trigger efficiencies in CCVR2.

Channel	Effective threshold [keV]	Efficiency (plateau)
1	9.0	0.8749 ± 0.0015
2	10.0	0.8778 ± 0.0015
3	3.0	0.9129 ± 0.0010
4	3.5	0.9126 ± 0.0010
5	5.0	0.8362 ± 0.0013
6	2.5	0.8248 ± 0.0013
7	2.5	0.8279 ± 0.0015
8	3.0	0.8578 ± 0.0014

Chapter 6

Application and results

CCVR2 data were processed with the Optimum Trigger and analyzed as described in the following.

In particular, in the first section we focus on the issues related to the calibration of the low energy region and on the efficiency of the pulse shape cuts. Checks of the trigger veto and coincidence performances are also reported.

In the last sections we describe the data analysis of the low energy region, focusing our interest on a radiation line revealed at 4.7 keV and on the Dark Matter detection perspectives in CUORE.

6.1 CCVR2 Analysis

The CCVR2 detector took data for a total live time of 19.4 days, excluding calibration measurements performed in the middle of the data taking (see Tab. 6.1). All the continuous data collected have been triggered and analyzed using DIANA, the CUORE official analysis framework.

The first-level analysis is similar to the CUORICINO one [147] (introduced in Sec. 4.6) with some exceptions, *e.g.* the amplitude estimated by the trigger was used, in place of the one estimated by the offline Optimum Filter. In the following,

Table 6.1. List of CCVR2 measurements.

Measurement	Type	Live time [days]
600049	Background	1.999732
600050	Background	1.952705
600051	Background	1.908343
600052	Background	1.827832
600053	Calibration	1.091061
600054	Calibration	0.712308
600055	Background	2.161419
600056	Background	3.781555
600057	Background	0.272316
600058	Background	2.801862
600059	Background	2.681497

after a brief description of the CCVR2 features, we focus on the most delicate aspects of the performed analysis.

6.1.1 CCVR2 setup

CCVR2 was composed by four $5 \times 5 \times 5$ cm³ crystals. Two thermistors were glued on each crystal. The values of the bias voltage (V_B), amplifier gain (G) and Bessel cutoff frequencies (f_B) of each bolometer are reported in Tab. (6.2) together with the measured thermistor resistance R_{bol} . The ADC sampling frequency and the duration of the acquisition window were set to 125 Hz, 5.008 s respectively for all channels.

Table 6.2. Parameters of the CCVR2 bolometers.

Channel	Crystal	V_B (mV)	G	f_B (Hz)	R_{bol} (M Ω)
1	076	10884	5030	16	27.6
2	076	20362	5030	12	11.7
3	011	15479	6026	20	45.1
4	011	12853	1942	12	69.3
5	096	28909	10009	16	17.8
6	096	10884	4133	12	78.6
7	007	10884	2540	12	60.7
8	007	8082	2540	12	133.6

Two external heaters were glued, one on crystal 011 and one on crystal 096. The other two crystals have no heater. This forced to perform the gain stabilization on the 5.4 MeV α line. This radioactive contribution is due to ^{210}Po that decays with an half life of about 138 days. In Tab. 6.3 the measured CCVR2 ^{210}Po amounts are reported. ^{210}Po high rate is the main cause of inefficiency of the Optimum Trigger since each high energy pulse has a corresponding dead time due to the veto. ^{210}Po contaminations are particularly abundant in “young” crystals like CCVR2 ones, while they are negligible in “older” crystals. This is why the CUORE crystals are grown several years before their use for rare decays’ search.

Table 6.3. ^{210}Po contamination of the CCVR2 crystals at the beginning of data taking.

Channel	Contamination [Bq/kg]
1	0.00945 ± 0.00010
2	0.00918 ± 0.00009
3	0.01357 ± 0.00011
4	0.01340 ± 0.00011
5	0.02732 ± 0.00016
6	0.02867 ± 0.00017
7	0.01168 ± 0.00010
8	0.01169 ± 0.00010

Table 6.4. Standard calibration peaks. Double peaks are considered as a combination of two Gaussians. Energy listed in [64].

Energy [keV]	Source
2614.533	^{208}Tl
2103.533	^{208}Tl single escape
1592.533 + 1588.19	^{208}Tl double escape + ^{228}Ac
968.971 + 964.766	^{228}Ac
911.204	^{228}Ac
583.191	^{208}Tl
511.0 + 510.77	annihilation γ + ^{208}Tl

6.1.2 Calibration

The standard analysis uses a third-order polynomial function as calibration function:

$$E = c_0 + c_1 A + c_2 A^2 + c_3 A^3, \quad (6.1)$$

where A is the estimated pulse amplitude and E the relative energy.

In this analysis we used the same function, but the c_0 coefficient was fixed to zero to remove any offset at zero energy. The coefficients were estimated using the lines from the ^{232}Th source (see Tab. 6.4, well visible in the two calibration runs (see Fig. 6.1)).

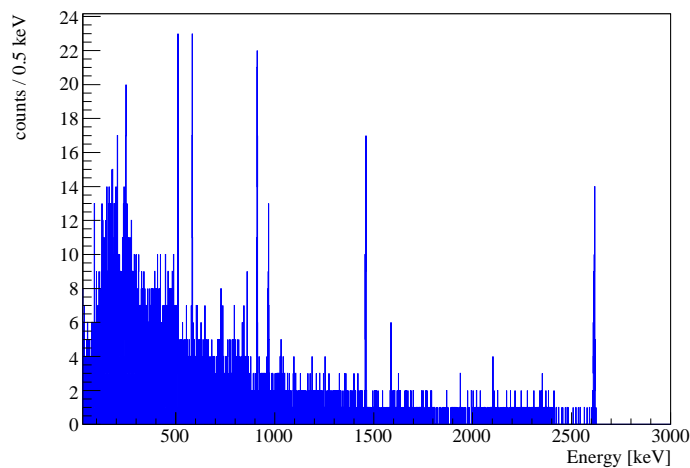


Figure 6.1. CCVR2 channel 3. Energy spectrum of the calibration runs 600053 and 600054.

The standard function and the one with $c_0 = 0$ produce similar results at high energies. The comparison of the residuals on the calibration peaks are shown in Fig. 6.2.

At lower energies the behavior of the two functions has been estimated on the γ lines generated by metastable Te isotopes, summing the data of all background

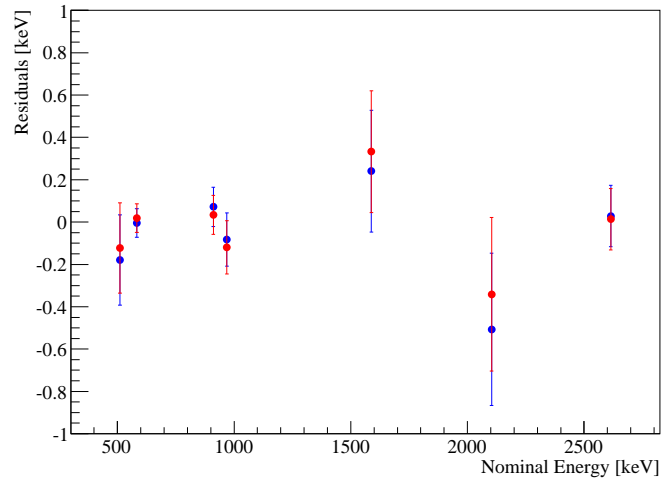


Figure 6.2. CCVR2 channel 3. Residuals on the 7 ²³²Th lines used for the calibration function estimation. Standard function is in red, the one with $c_0 = 0$ is in blue.

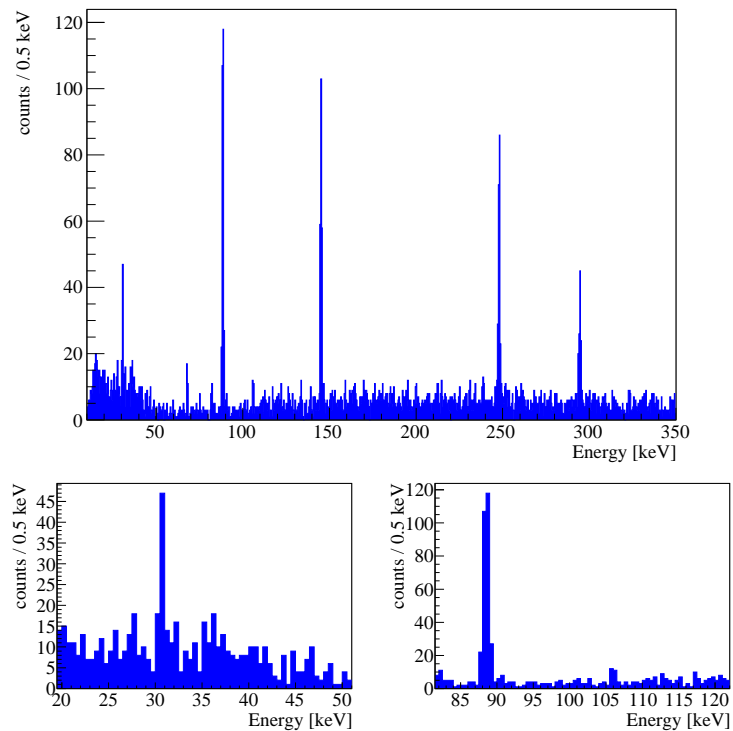
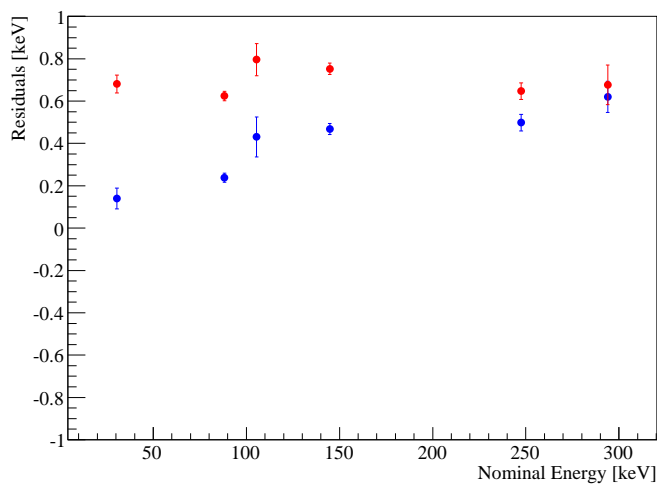


Figure 6.3. CCVR2 channel 3 background spectrum. The two spectra on the bottom represent the spectrum zoomed near two low activity peaks.

Table 6.5. Most prominent gamma lines of the metastable Te isotopes.

Energy [keV]	Source
30.4912	Sb X-Ray
88.26 ± 0.08	^{127m}Te
105.50 ± 0.05	^{129m}Te
144.780 ± 0.025	^{125m}Te
247.5 ± 0.2	^{123m}Te
293.98 ± 0.04	^{121m}Te

**Figure 6.4.** CCVR2 channel 3. Residuals on the low energy lines reported in Tab. 6.5. Standard function is in red, the one with $c_0 = 0$ is in blue.

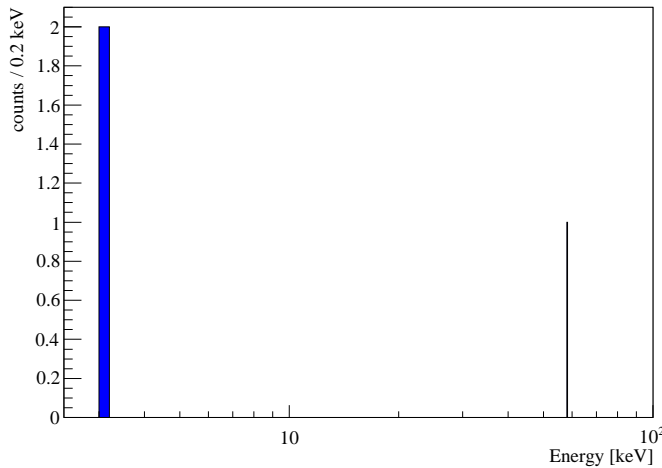
runs (see Fig. 6.3). The calibration residuals were computed on the most prominent lines (see Tab. 6.5 and Fig. 6.3), and show that the function with $c_0 = 0$ has smaller residuals at low energy, which approach zero for $E \rightarrow 0$. The standard function residuals, instead, approach a constant value, that is the c_0 coefficient estimated from the fit from the high energy peaks (see Fig. 6.4). Therefore, even if the two functions have comparable performances in the MeV region, the standard one has larger residuals in the low energy region. The function with $c_0 = 0$ has been chosen as calibration function, nevertheless there is a clear trend in the four lowest points at low energies. To estimate the residual at each energy in the range $[0,150]$ keV a linear fit of the four points in the range has been performed, and the parameters are reported in Tab. 6.6.

The correctness of the calibration at energies lower than 30 keV can be checked looking at events generated by ^{40}K contaminations in the crystals bulk. In the electron capture decay of this isotope a 3.190 keV X-ray and a 1461 keV γ are emitted. The γ can escape the crystal and hit another crystal, giving a double hit event. The X line could be seen by looking at “multiplicity two” events in which there is an

Table 6.6. Linear fit parameters of the residuals of the calibration function with $c_0 = 0$.

Channel	Intercept keV	Slope
1	-0.431 ± 0.074	0.00289 ± 0.00067
2	0.09 ± 0.17	0.0010 ± 0.0014
3	-0.024 ± 0.048	0.00336 ± 0.00045
4	0.161 ± 0.057	0.00057 ± 0.00052
5	-0.033 ± 0.088	0.00202 ± 0.00064
6	-0.065 ± 0.035	0.00210 ± 0.00026
7	-0.010 ± 0.059	0.00105 ± 0.00057
8	-0.062 ± 0.073	0.00133 ± 0.00071

energy release around the γ line in one crystal. The single crystal energy spectrum of all channels, requiring that in another crystal there is an energy release within [1451,1471] keV, is shown in Fig. 6.5.

**Figure 6.5.** Energy spectrum in background runs of low energy events in coincidence with events in another crystal with energy around 1461 keV. All four crystals are used to evaluate the coincidence, without applying the pulse shape cuts. The two events at low energy correspond to the 3.190 keV X ray emitted in the ^{40}Ar de-excitation.

Two events are visible in the X region, and, as reported in Tab. 6.7, have the expected energy and a 8 ms time delay (corresponding 1 sampling period). A third event at 58 keV is visible, but in this case the time delay is 32 ms, and could be due to an accidental coincidence.

6.1.3 Cuts efficiency

Signal events of each channel were selected using the χ_{OT}^2 variable, described in section 5.3. This variable has a quite complex dependence on energy as it can be seen in Fig. 6.6. It increases with energy, then decreases to a minimum and then increases again. The minimum is at the average energy of the events used to build

Table 6.7. Events in coincidence with [1451,1471] keV events in a different crystal.

channel	E keV	E_{corr} keV	χ_{OT}^2	channel coincident	E coincident keV	Δt ms
6	3.04	3.10	1.23	1	1456	8
7	3.18	3.19	0.77	6	1462	8
6	58.08	58.02	0.97	3	1457	32

the average pulse (that was made with calibration events in the [1,3] MeV region). At higher energy the shape of the signal becomes significantly different from the average pulse, and the χ_{OT}^2 increases. At lower energy it decreases, since it becomes less sensitive to the shape and the noise contribution becomes dominant. In the region below ~ 60 keV the distribution is flat, allowing simple box cuts.

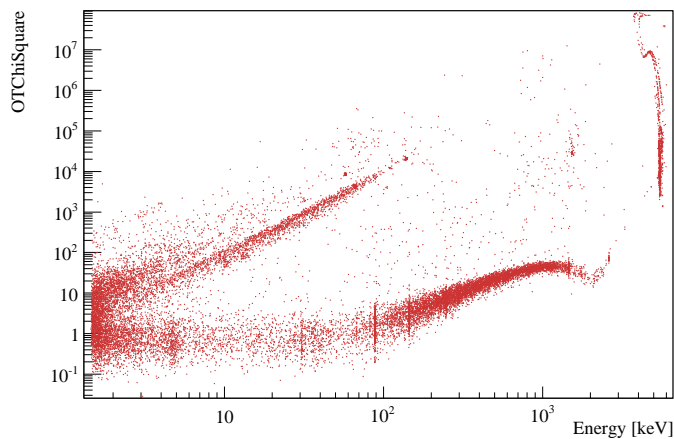


Figure 6.6. CCVR2 channel 3. χ_{OT}^2 distribution in all background measurements. The band at low χ_{OT}^2 is populated by signal events. At higher values there are triggered mechanic vibrations, electronic spikes and pile-up's.

The cut efficiency was evaluated on the 30.49 keV line, that is the known radioactive peak with the lowest energy, using all CCVR2 statistics. A series of fits has been performed selecting the events below a fixed χ_{OT}^2 value. For each χ_{OT}^2 value the spectra of cut accepted events and cut rejected events were simultaneously fitted with a Gaussian, representative of the signal, plus a first-order polynomial function, representative of the background (Fig. 6.7). The signal efficiency was evaluated as

$$\epsilon_S = \frac{S_A}{S_A + S_R} \quad (6.2)$$

where S_A and S_R are the number of events in the fitted Gaussian peak in the “accepted” spectrum and in the “rejected” spectrum respectively (Fig. 6.8). The background efficiency was evaluated as

$$\epsilon_B = \frac{B_A}{B_A + B_R} \quad (6.3)$$

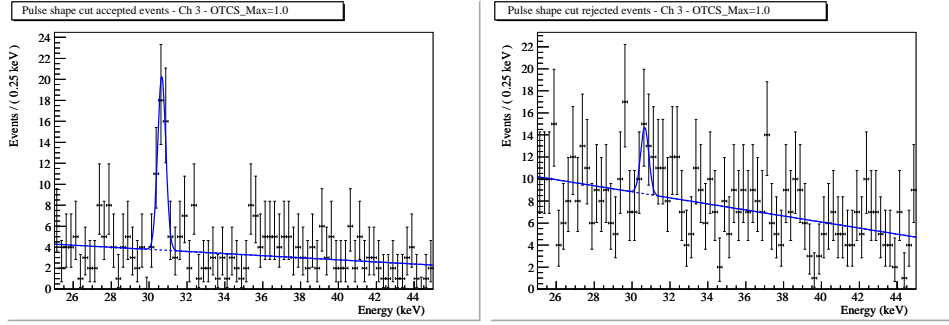


Figure 6.7. CCVR2 channel 3. Fit at the 30.49 keV line in accepted events (left) and rejected events (right). Event selection was done imposing $\chi_{OT}^2 < 1.0$.

where B_A and B_R are the number of events in the fitted background in the “accepted” spectrum and in the “rejected” spectrum respectively (Fig. 6.8). Both these efficiencies were evaluated directly in the fit. Finally for each cut on χ_{OT}^2 the

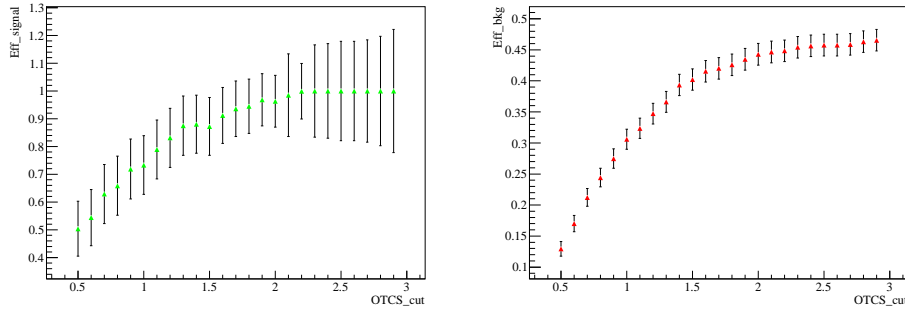


Figure 6.8. CCVR2 channel 3. Cut efficiency on signal (left) and on background (right) events.

statistical significance, S , was calculated (see Fig. 6.9):

$$S = \frac{\epsilon_S}{\sqrt{\epsilon_B}}. \quad (6.4)$$

Since the significance is almost constant, the optimal cut was chosen among those with maximum efficiency on the signal, requiring a background efficiency as little as possible. Used cuts are summarized in Tab. 6.8 for all CCVR2 channels.

6.1.4 Time correlation check

As said in section 5.2, when an high energy pulse is filtered a set of secondary pulses is seen. The veto system allows to discard these pulses, that could generate peaks in the low energy spectrum. We checked that this effect, and any other time correlation within pulses, are correctly handled by our trigger algorithm. We rejected all the events that are followed or anticipated by another event in the same channel within 10.016 s, length of the full filtered window. The resulting spectrum should differ from the original one for a fixed percentage, not depending on the energy. In Fig. 6.10 the two spectra and their ratio are reported, where it can be seen that no fake structure is generated by the trigger.

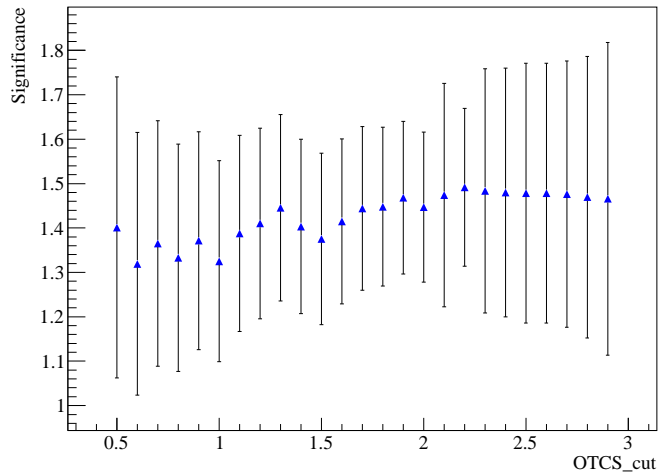


Figure 6.9. CCVR2 channel 3. Statistical significance as a function of the cut on χ_{OT}^2 .

Table 6.8. Cuts chosen on χ_{OT}^2 for all CCVR2 channels.

Channel	OTChiSquare Maximum	Signal Efficiency	Background Efficiency	Statistical Significance
1	2.9	0.68 ± 0.11	0.218 ± 0.014	1.45 ± 0.27
2	2.6	1.00 ± 0.12	0.567 ± 0.017	1.33 ± 0.18
3	2.2	1.00 ± 0.15	0.451 ± 0.017	1.49 ± 0.25
4	4.2	0.94 ± 0.10	0.574 ± 0.019	1.28 ± 0.16
5	2.4	1.00 ± 0.17	0.544 ± 0.018	1.36 ± 0.25
6	3.1	1.00 ± 0.19	0.390 ± 0.016	1.59 ± 0.34
7	1.8	1.00 ± 0.34	0.487 ± 0.015	1.43 ± 0.50
8	4.5	0.91 ± 0.10	0.530 ± 0.016	1.26 ± 0.15

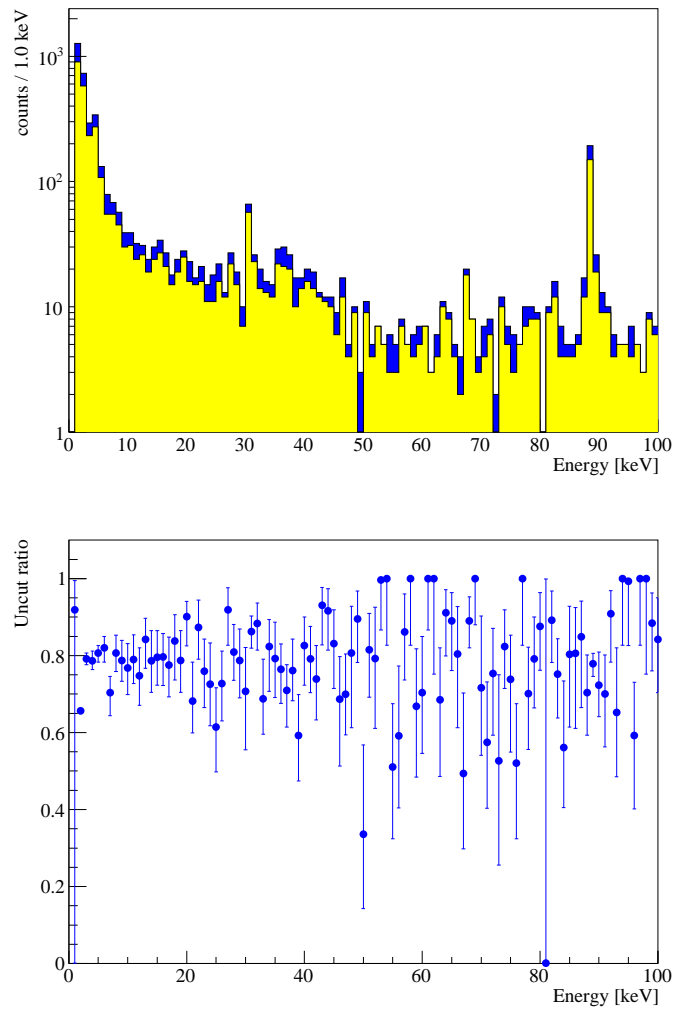


Figure 6.10. CCVR2 channel 3, $\chi_{OT}^2 < 2$. Top: Spectrum without time cuts in blue, while in yellow the spectrum excluding events with another pulse within 10.016 s. Bottom: ratio between the two spectra, the distribution is flat, even if limited by the low statistics.

6.1.5 Coincidences check

In order to improve the significance of the data samples, an anti-coincidence cut was imposed to the events, *i.e.* we required that, given a selected event, there was no detected energy in all the remaining bolometers within a time window $\Delta t = 150$ ms. The efficiency of the combination of this cut with the pulse shape one was estimated by fitting the 30.49 keV line as in section 6.1.3. Comparing results with the ones in Tab. 6.8, we obtained a loss of statistical significance as can be seen, for example, in channel 3 (Fig. 6.11 and Tab. 6.9). In order to understand this variation, one

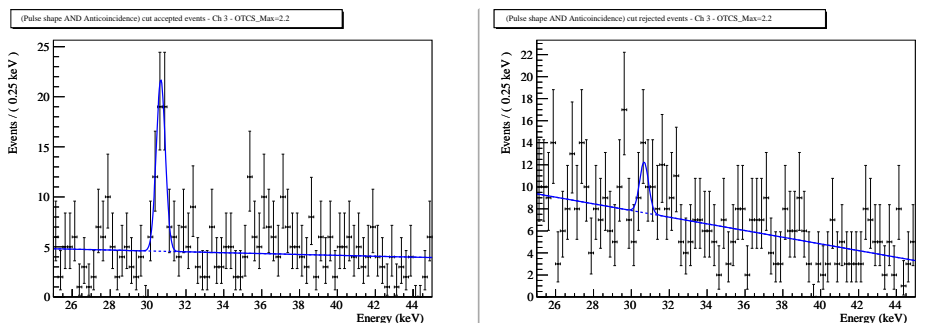


Figure 6.11. CCVR2 channel 3. Fit at the 30.49 keV line in cut accepted events (left) and cut rejected events (right). Event selection was done imposing anti-coincidence and $\chi_{OT}^2 < 2.2$.

Table 6.9. CCVR2 channel 3 cuts efficiency.

Cuts	Signal Efficiency	Background Efficiency	Statistical Significance
$\chi_{OT}^2 < 2.2$	1.00 ± 0.15	0.451 ± 0.017	1.49 ± 0.25
$\chi_{OT}^2 < 2.2 + AC$	0.79 ± 0.10	0.409 ± 0.017	1.24 ± 0.18

must consider two effects in competition. On one hand, signal efficiency decreases because some of the 30.49 keV events are produced after a metastable Te decay, and the emitted γ can hit another crystal. There is no reason to cut these events. On the other hand, background efficiency decreases of about 4%. Such variation can be associated to the random coincidences of the single channel with the whole detector, whose probability can be evaluated as

$$P_c = 2 \frac{N_{TOT}}{T} \Delta t = 0.033 \quad (6.5)$$

where $N_{TOT} \simeq 184000$ is the total number of events of the three remaining bolometers and $T = 19.4$ d is the total detector exposure. In conclusion, the anti-coincidence cut seems to lower the statistics without improving the signal significance. No anti-coincidence cuts were applied in the analyses reported in the following chapter, even though we are looking for single-hit events.

6.1.6 First Level Analysis Results

The Optimum Trigger and the pulse shape algorithm allow to lower the energy threshold down to the few keV region and to reject bad signals. The energy spectra of the four crystals in the region between the threshold and 25 keV are shown in figure 6.12, where the best among the two thermistors in terms of resolution and threshold has been selected.

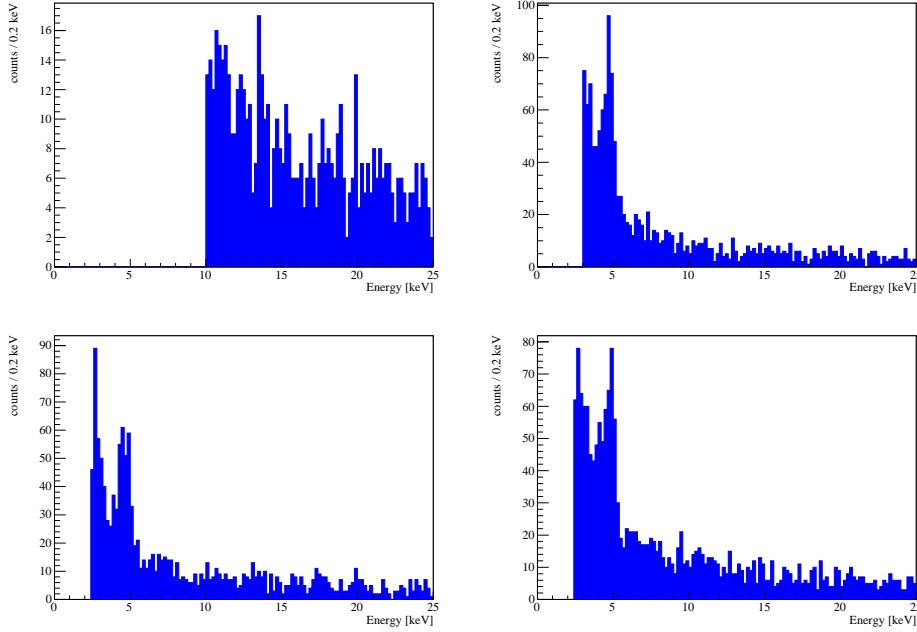


Figure 6.12. Low energy spectra of channels 2 (top left), 3 (top right), 6 (bottom left) and 7 (bottom right). Full CCVR2 statistics (19.4 days) with pulse shape cut applied.

6.2 A first Optimum Trigger application: ^{123}Te L line

An evident peak appears at about 4.7 keV in channels with the lowest thresholds. This line could be ascribed to the L x-ray emitted after the ^{123}Te EC decay in ^{123}Sb (see details in the next section), and the measurement of its intensity would lead to the measurement of the decay half-life for the first time. In order to determine this intensity, one must take into account a known resonant background. At 4.7 keV, in fact, there is also the L line of other Sb isotopes, decay products of several metastable Te isotopes. This contribution has been estimated by a Montecarlo simulation using GEANT4. Using the simple geometry of CCVR2, 100000 decays were simulated for the following isotopes: ^{121}Te , ^{121m}Te , ^{123m}Te , ^{125m}Te , ^{127m}Te and ^{129m}Te . All these isotopes have lifetimes going from several days up to few months, with well visible characteristic lines (also discussed in section 6.1.2). The simulated decay spectra were so normalized using the intensities of these lines, evaluated by fitting each peak in the CCVR2 single channel spectrum with a Gaussian plus a first-order polynomial. The final metastable contribution for each channel was estimated as the integral of the obtained simulated spectrum (Fig. 6.13) in a region

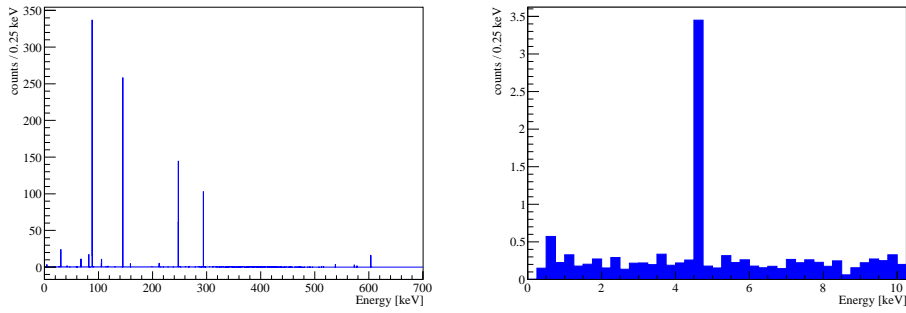


Figure 6.13. Simulated metastable Te isotopes spectrum in CCVR2 channel 3. Left: the whole spectrum. Right: spectrum below 10 keV, showing the presence of the 4.7 keV line plus a flat background.

2 FWHM wide, according to channel resolution, centered in 4.7 keV, excluding flat background events.

To estimate the intensity and the effective energy of the line from the data, a separate fit for each channel was performed, using a fit function constituted by a Gaussian plus two exponential decays to reproduce background. The pulse shape cut was set as in Tab. 6.8 and the related efficiencies were recomputed, since the statistics is much greater than the Sb K line at 30 keV. The obtained number of events (N_p) was then corrected according to previously estimated trigger efficiencies (ϵ_{OT}) and metastable contributions (N_m), according to the equation

$$N_s = \frac{N_p}{\epsilon_{OT}} - N_m. \quad (6.6)$$

Best fits are shown in Fig. 6.14. In Tab. 6.10 we report the summary of the parameters of each channel, including the energy estimated from the fit, the energy corrected for the calibration residual at 4.7 keV (E_{corr}), the trigger efficiency (ϵ_{OT}), the pulse shape cut efficiency (ϵ_{χ^2}), the estimated value of N_m and N_s . The error on N_s does not include the error on the trigger efficiency.

Table 6.10. Best fit results for 4.7 keV line.

Ch	E [keV]	E_{corr} [keV]	FWHM [keV]	ϵ_{OT}	ϵ_{χ^2}	N_m	N_s
3	4.735 ± 0.034	4.74 ± 0.28	0.56 ± 0.11	0.91	1.00 ± 0.09	3.3	163 ± 29
6	4.593 ± 0.049	4.65 ± 0.28	0.94 ± 0.12	0.82	1.00 ± 0.03	18.0	187 ± 26
7	4.764 ± 0.054	4.76 ± 0.38	0.69 ± 0.12	0.83	0.97 ± 0.13	7.6	136 ± 33

We projected the profile negative log-likelihood over N_{sig} for each channel and then summed the three functions to obtain the comprehensive profile negative log-likelihood (see Fig. 6.15). The estimated value of the number of signal events is $N_{sig} = 167 \pm 19$ counts/crystal. From this we evaluate the intensity per day and per kg of TeO_2 as:

$$I = 11.5 \pm 1.3 \text{ counts/day/kg} \quad (6.7)$$

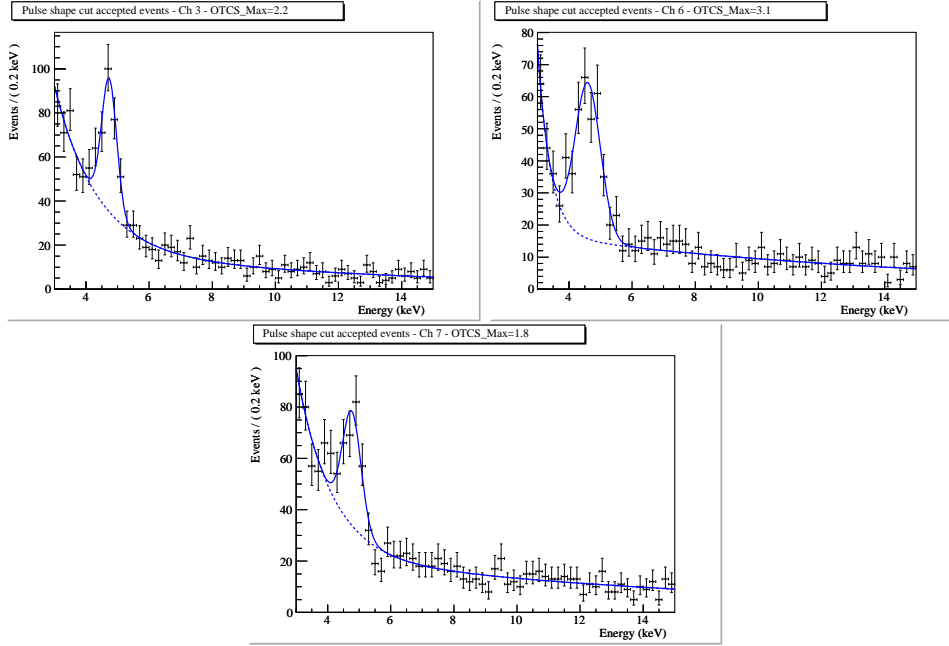


Figure 6.14. Best fits at 4.7 keV line on channel 3 (top left), channel 6 (top right) and channel 7 (bottom).

where we set the crystal mass to 750 g, and we used the total livetime of 19.4 days.

The trigger efficiencies have been evaluated at the end of the run, via the N-pulses measurement (see Sec. 5.4). However they could be different in the background runs analyzed here, because the working conditions are in principle different (temperature, noise, ^{210}Po intensity, etc...). Unfortunately there are no methods to check the efficiency in time, so we just checked that the rate of the 4.7 keV peak is constant and we assumed the rate fluctuation as systematic error on the trigger efficiency. In Fig. 6.16 the peak rate in time is reported, where it can be seen that it can be assumed constant and its fluctuations amount to $3.3/28.7 = 11\%$.

6.2.1 The ^{123}Te decay

The ^{123}Te isotope has a natural abundance in Tellurium of 0.89% (see Tab. 2.1), and decays via electron capture in ^{123}Sb with a Q-value of 53.3 ± 0.2 keV, although this decay has never been observed. In the decay, a monochromatic neutrino and a X-ray are emitted. Unlike in other isotopes, the K -electron capture is suppressed and the decay proceeds through L and M capture [154]. The branching fractions have been predicted in the proportion 1:400:150, meaning that for a K decay, 400 and 150 decays occur through L and M emission respectively. Two positive evidences in the K emission show a discrepancy by six orders of magnitude, namely $(1.24 \pm 0.10) \cdot 10^{13}$ y and $(2.4 \pm 0.9) \cdot 10^{19}$ y, and recently a limit of $3.2 \cdot 10^{16}$ y at 95% confidence level has been set [155]. One of the main problems of the past measurements was associated with the fact that observations relied on the outside detection of K X-rays following the deexcitation of ^{123}Sb . This line is at 26.1 keV, very close to the Te K X-ray line at 27.3 keV which might be excited by other processes such as cosmic

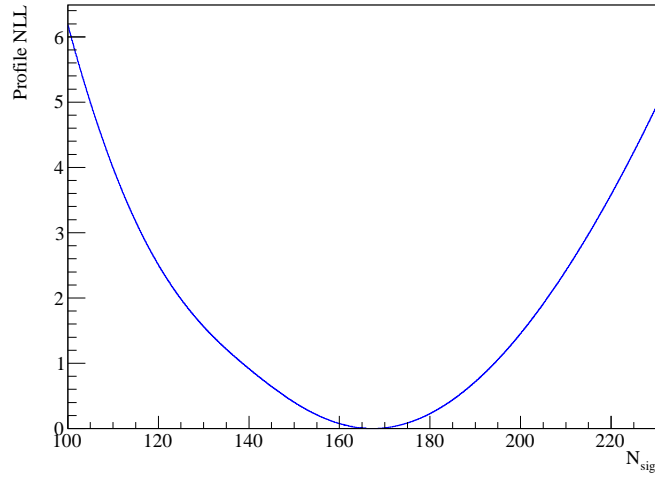


Figure 6.15. Profile negative log-likelihood projected over the number of signal events in a single CCVR2 crystal in 19.4 days.

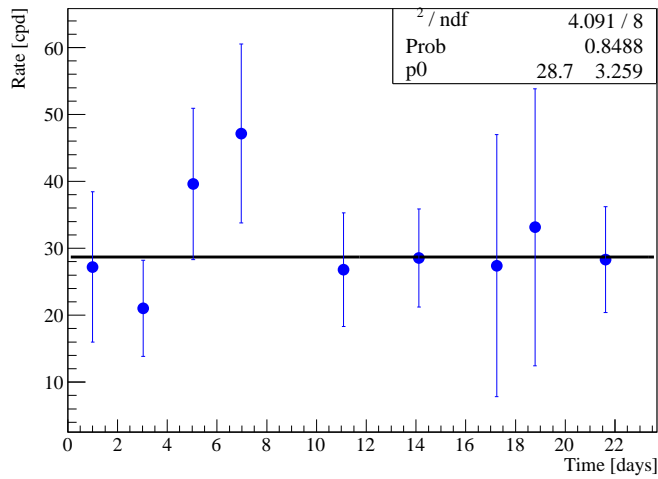


Figure 6.16. Rate of the 4.7 keV peak versus time, all 3 channels. The error on the average is assumed as systematic error on the trigger efficiency.

rays and radioactive background. The L decay has a cleaner signature. As seen in the previous section, the background arising from other Te isotopes is suppressed, since in these decays the K emission is favoured. The energy averaged over the three channels, that is 4.72 ± 0.18 keV, is compatible with the 4.6983 keV energy of the $L1$ line of Sb. Therefore under the hypothesis that this line comes from the ^{123}Te decay, we evaluate the half life as

$$T_{1/2}^L = \frac{\ln(2) N_A n \alpha}{I} = (5.7 \pm 0.6 \text{ (stat.)} \pm 0.6 \text{ (syst.)}) \cdot 10^{18} \text{ y} \quad (6.8)$$

where N_A is the Avogadro number, n is the number of TeO_2 moles in one kg, α is the isotopic abundance and I is the intensity in Eq. 6.7.

6.3 Dark Matter limits from direct detection

As already stated, low energy spectra can be also used to obtain WIMP Dark Matter limits. This is usually done making the conservative assumption that all the events in the continuum are nuclear recoils due to WIMP elastic scattering with TeO_2 nuclei. The energy spectrum of this process can be obtained as explained in Sec. 2.2. Several fits were performed on the three best CCVR2 channels (3, 6, 7), using a fit function composed by:

- The differential rate of elastic nuclear recoils in TeO_2 (Eq. 2.26) with $\rho_W = 0.3 \text{ GeV/cm}^3$, $v_0 = 220 \text{ km/s}$ and $v_{esc} = 600 \text{ km/s}$
- An exponential function, used to approximate non-WIMP background
- A gaussian function centered at 4.7 keV

Each channel was fitted in the energy range going from 3 keV up to 25 keV, changing only the value of WIMP mass M_χ (Fig. 6.17). The only free parameter in the WIMP recoil function was the nucleon-WIMP scattering cross section σ_0 . It is important to underline that σ_0 appears in the function as a simple normalization factor, meaning that, fixed a particular value of M_χ , the shape of the function is fixed. The exponential function previously quoted was hence used to fit the spectrum in the regions in which the WIMP recoil contribution is negligible. An

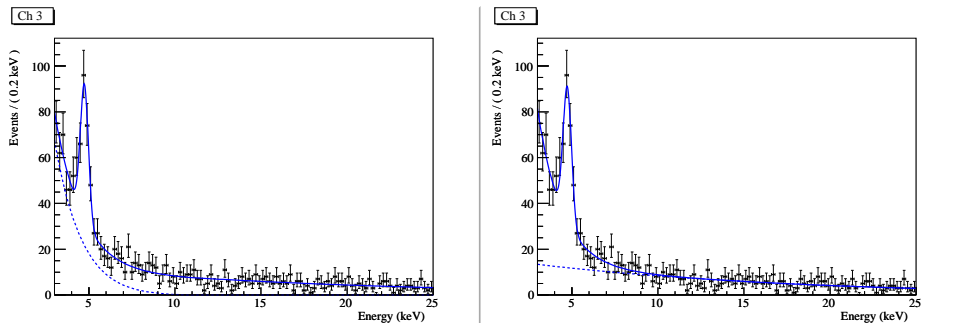


Figure 6.17. Fit of CCVR2 channel 3 for two different values of M_χ ($M_\chi = 5 \text{ GeV}$ in the left plot, $M_\chi = 100 \text{ GeV}$ in the right one). The dashed line represent the fitted Dark Matter component.

upper limit at 97.5% C.L. on the nucleon-WIMP cross section was obtained as

$$\sigma_0 < (\sigma_{FIT} + 2\sigma_\sigma) \quad (6.9)$$

and plotted in Fig. 6.18. There σ_σ is the combination of the statistical error of the fit and of the systematic errors on the trigger efficiency and on the pulse shape cut.

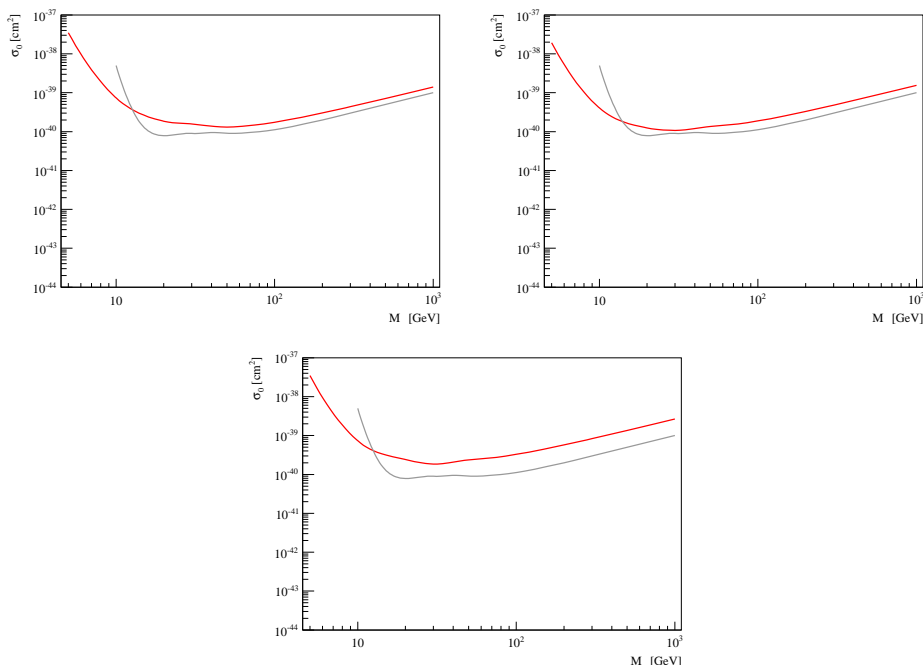


Figure 6.18. CCVR2 exclusion plots (in red) on channel 3 (top left), channel 6 (top right) and channel 7 (bottom). In gray are reported MIBETA results [156].

The obtained limits are slightly different among the three channels: this difference, however, is due for the most part to the different background rate of the bolometer, not to the use of a limited statistics. Considering this, we conclude that combining the three results is meaningless and the best bolometer can be chosen as the final result. In Fig. 6.19 is shown the exclusion plot obtained in CCVR2 channel 6, compared with the limits obtained by other experiments. For high values of M_χ , nuclear recoil spectrum is almost flat. Cross section limits derive from the rate in the continuum at tens of keV, since at lower energies the pedestal is dominant. For low values of M_χ , the expected spectrum is particularly enhanced at low energies, with negligible effects as far as the energy increases. In this particular case Optimum Trigger becomes very important, since it makes accessible this few keV region. At high M_χ , our result is very similar to the MIBETA one [156], a past experiment using TeO_2 , since the result is constrained by the background rate in a region that was accessible also in the past. Nevertheless, our result is better at low M_χ , since it is related to an energy region that was previously unexplored.

6.4 Annual modulation in CUORE

CCVR2 lasted less than one month, making hopeless an annual modulation search, but CUORE will take data for several years. So it is possible to forecast CUORE

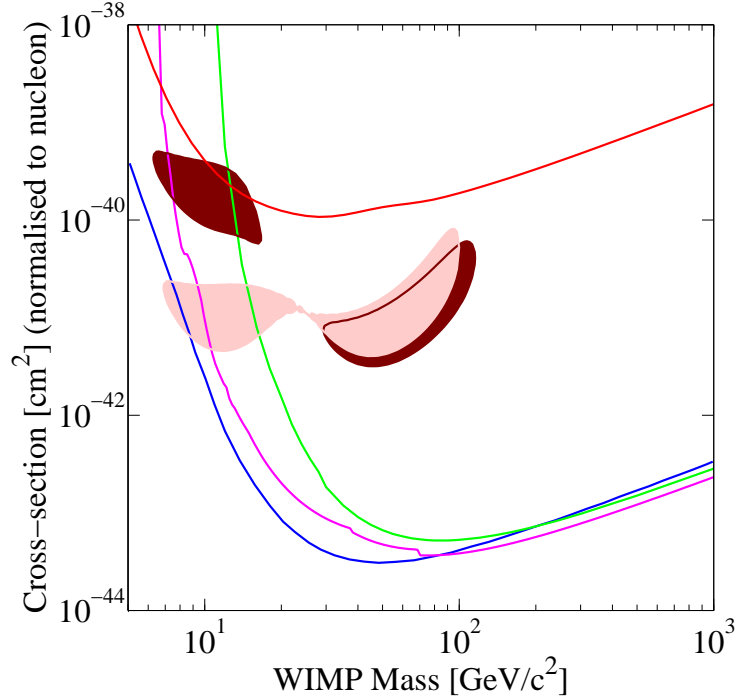


Figure 6.19. CCVR2 result (in red) compared with the actual limits on WIMP-nucleon elastic scattering cross section. DAMA/LIBRA 3σ evidence with ion channeling in dark red and without ion channeling in pink [157], Edelweiss II in green [85], XENON100 in blue [158], CDMS in magenta [86].

capability in WIMP annual modulation detection. Correcting v_E in Eq. 2.26 as explained in section 2.2.1, the differential recoil rate becomes sensitive to time. In Fig. 6.20 the expected modulation amplitude for different values of M_χ is shown. We estimated the CUORE sensitivity with toy Montecarlo. The background measured in the three CCVR2 crystals, corrected with the trigger efficiencies, was fitted and the fit function was assumed as the CUORE background (see Fig. 6.21). For each value of M_χ the value of σ_0 is scanned performing N toys, until the asymmetry is detectable 90% of the times. A set of $N = 200$ toy corresponds to fixed values of (M_χ, σ_0) , and each toy is made as follows:

1. Generate background plus asymmetry expected in three months across June the second.
2. For five times (corresponding to five years of data taking) spectra are generated and then summed.
3. Repeat the two points above setting the expected asymmetry across December the second.
4. Subtract the December spectrum from the June one, obtaining the asymmetry distribution.
5. Fit the distribution with a $y = 0$ line and then with the correct asymmetry function.

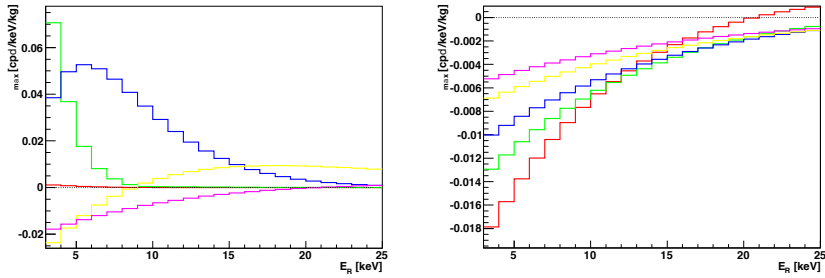


Figure 6.20. Amplitude (Max-Min) of the differential rate modulation for $\sigma_0 = 10^{-41} \text{ cm}^2$ and various WIMP masses. Left: 5 GeV in red, 10 GeV in green, 20 GeV in blue, 50 GeV in yellow and 100 GeV in magenta. Right: 100 GeV in red, 150 GeV in green, 200 GeV in blue, 300 GeV in yellow and 400 GeV in magenta.

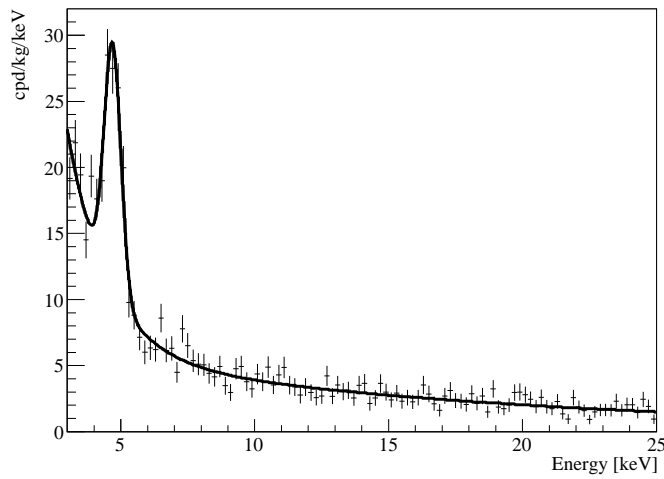


Figure 6.21. CCVR2 background spectrum in cpd/kg/keV, fitted with a Gaussian plus two exponential decays. The fit function is representative of the future CUORE background.

6. If $P(\text{asymmetry}) > P(y = 0)$ the asymmetry is considered detectable (P is the fit probability).

If in $M/N = 90\%$ toys the asymmetry is detectable, the value of σ_0 corresponds to the 90% CL sensitivity at the wimp mass M_χ . If M/N differs from 90%, the set of N toys is repeated changing σ_0 until the desired CL is reached. An example of a toy with $M_\chi = 10$ GeV and $\sigma_0 = 10^{-41}$ cm² is shown in Fig 6.22. The scan on

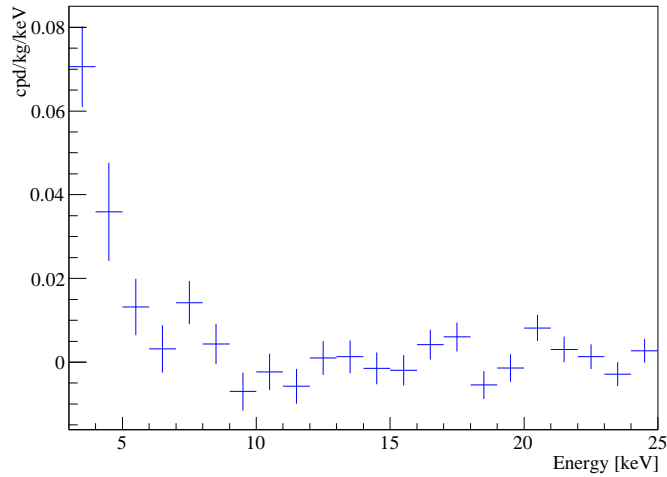


Figure 6.22. Simulated modulation (3 months across June 2nd minus 3 months across December 2nd) in cpd/kg/keV for 5 years of CUORE exposure. WIMP mass and cross section values are $M_\chi = 10$ GeV and $\sigma_0 = 10^{-41}$ cm².

M_χ included the masses (5, 7.5, 10, 16, 20, 30, 50, 75, 100, 127.6, 200, 300, 500, 750, 1000) GeV, and the obtained sensitivity is shown in Fig. 6.23. In the plot the sensitivity of CUORE-0 in 3 years of data taking is also shown.

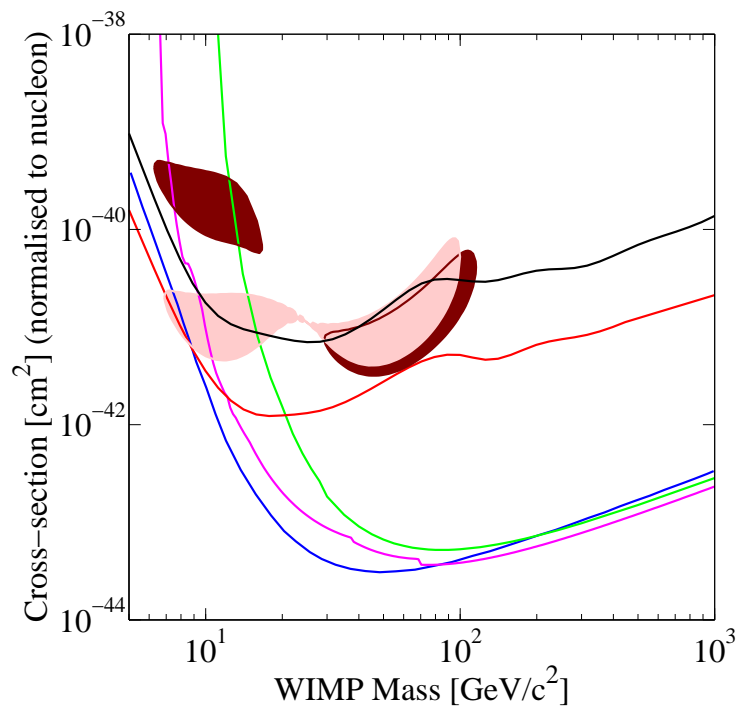


Figure 6.23. CUORE-5y (in red) and CUORE-0-3y (in black) sensitivities compared with the actual limits on WIMP-nucleon elastic scattering cross section. DAMA/LIBRA 3σ evidence with ion channeling in dark red and without ion channeling in pink [157], Edelweiss II in green [85], XENON100 in blue [158], CDMS in magenta [86].

Conclusions

In this Ph.D. work we developed a new trigger for the CUORE experiment that is sensitive to the signal shape. This trigger, based on the Optimum Filter algorithm, was tested on the four CUORE-like crystals of the second CUORE Crystals Validation Run (CCVR2), using a total exposure of $44 \text{ kg} \cdot \text{d}$.

The application to these data pushed the energy threshold from tens of keV down to the few keV region, an energy range that has never been available before in TeO_2 bolometers. The detection efficiency has been evaluated by means of a dedicated run with external heaters and validated using Montecarlo, resulting in excess of 80%.

We also developed a pulse shape algorithm to reject fake events induced by electronics and mechanic vibrations, which populate the few keV region. Its application allows to cut a significative amount of noise events, maintaining the signal efficiency close to 100%.

Analyzing the Optimum Triggered data, we observed a peak centered at about 4.7 keV in the energy spectra of the bolometers with the lowest threshold. Under the hypothesis that this line comes from the ^{123}Te decay, we evaluated for the first time its half-life as $(5.7 \pm 0.6 \text{ (stat.)} \pm 0.6 \text{ (syst.)}) \cdot 10^{18} \text{ y}$.

We also estimated a limit on Dark Matter interactions, that is similar to the one obtained in the past by MIBETA.

Finally we estimated the sensitivity of CUORE and CUORE-0 to a Dark Matter modulation signal by means of toy Montecarlo, under the assumption that the background of the bolometers of these experiments will be the same of the CCVR2 ones. The resulting sensitivity plot shows that CUORE will be able to test the DAMA claim. This will be extremely important because, even if DAMA allowed region has been already excluded by several experiments, none of them was sensitive to the annual modulation effect. In this framework, CUORE could be the first experiment to look for modulation with a different experimental setup, providing a crucial cross-check of this controversial observation.

Acknowledgments

Prima di tutto, vorrei ringraziare il prof. Fernando Ferroni per la grande fiducia che mi ha sempre dimostrato. Durante questi anni, nonostante i suoi numerosi impegni, è sempre stato estremamente disponibile e mi ha saputo guidare, alternando il bastone e la carota, fino al traguardo del dottorato. Mille grazie!

Then I wish to thank prof. Gabriel Chardin for his precious suggestions and valuable questions that have broadened my mind and improved the quality of my work. La terza persona che va sul podio non può essere che Marco... o meglio, Farco! In tutte le fasi della mia tesi lui ha svolto un ruolo fondamentale come guida, come consulente e come compare. E la cosa più bella è che accanto a lui non finisco mai di imparare e, soprattutto, di divertirmi. Grazie davvero.

Se dovessi fare l'elenco di tutti i motivi per cui dovrei ringraziare Fabio, avrei bisogno di scrivere altre due tesi. Ma, più di ogni altra cosa, lo ringrazio per la sua amicizia. Ringrazio Claudia per avermi aiutato ad orientarmi nella foresta dei picchi radioattivi con competenza, disponibilità e simpatia. Poi vabbe'... quando ci saranno gli shift di CUORE0 dovremo fare due conti!

Grazie a Riccardo, che sa sempre darmi il suggerimento giusto quando credo di essere in un vicolo cieco, e a Silvio, che ha sempre trovato un attimo di tempo per parlare con me di fisica e non solo.

Un sentito grazie va all'implacabile Sergio per il suo fondamentale ruolo di pazientissimo maestro di DAQ... e per essere il mio compagno di doppio a ping pong!

I'd like also to thank the CUORE collaboration for all the support to my thesis work. In particular, I wish to thank Yuri, Chiara, Ioan, Carlo, Paolo, Stefano, Seth, Cecilia, Luca and Lucia for their questions and their answers.

Nella mia lista non possono mancare Carlo, Lorenzo, Nicola, Riccardo, Valeria, Francesco, Erica, Nadejda, Francesco, Silvia... e il sempre benvenuto simbiante Paoletto perché rendono la Baita un luogo di lavoro straordinariamente divertente. Colgo anche l'occasione per ringraziare i ragazzi dei gruppi ATLAS e CMS di Roma per essere così scarsi a calcetto.

Un ringraziamento particolare va a Erminia e Silvia che mi hanno aiutato a destreggiarmi nella cosmologia teorica e sperimentale.

Vorrei poi ringraziare tutti i miei amici, vicini e lontani, per essermi stati accanto in questi tre anni di dottorato. Nei momenti più felici così come in quelli più tristi non mi sono mai sentito solo. Grazie di cuore.

Una menzione speciale va a Chiara per aver condiviso con me un pezzetto di vita e aver sopportato la mia testardaggine.

Grazie alla mia famiglia che mi dà l'esempio e non si abbatte mai.

Dulcis in fundo, desidero ringraziare Michela per essere arrivata nel momento giusto e avermi cambiato la vita.

Appendix A

Average Pulse and Noise Power Spectrum evaluation

An approximate representation of the ideal pulse for each channel is obtained from a pointwise average in the time domain over many high energy pulses. In order to select these pulses, we define a certain number of selection criteria, based on physical quantities, that characterize a ideal particle pulse. A filter selects the events matching these criteria and uses only these events to calculate the average pulse. The average pulses for CCVR2 dataset, for example, were calculated according to the following selection criteria:

- There must be only one pulse in the acquisition window, in order to prevent pile-up.
- The energy of the event must be between 1000 and 3000 keV.
- The module of the baseline slope must be lower than 13.07 keV/s, because the baseline is expected to be flat in absence of signal.
- The rise time of the pulse, defined as the time interval in which the signal rises from 10% up to 90% of the pulse height, must be lower than 100 ms.
- The decay time of the pulse, defined as the time interval in which the signal decreases after its maximum from 90% down to 30% of the pulse height, must be between 0.08 s and 0.9 s. Decay time and rise time selections avoid the inclusion of high amplitude noise pulses.

In computing the average, the pulses are shifted so that they are aligned by the following procedure. First, the position of the maximum value of the raw signal, t_M , is identified. Then, the signal is differentiated; since bolometric signals have very flat tails, their derivative can be considered in first approximation as a continuous periodic function of the acquired window. The alignment is then performed by cyclicly shifting the derivative so that t_M falls at a chosen reference point and by integrating.

The average noise power spectrum for each channel is obtained by averaging the power spectrum of many noise samples that are acquired by a random trigger. Not all the triggered noise samples are used, since two cuts are applied:

- The module of the baseline slope must be lower than 13.07 keV/s, since the noise is supposed to be flat around the baseline.
- The acquired window must contain no pulses, avoiding the inclusion in the noise power spectrum of frequencies that are typical for signal events. Including them would make the following optimum filter algorithm less precise.

Appendix B

Comparison of χ_{OT}^2 with TVL and TVR

Two shape parameters have been designed for CUORE high energy analyses, the Test Value Left (TVL), and the Test Value Right (TVR). Their expression is:

$$\text{TVL} = \frac{1000}{A \cdot w_l} \sqrt{\sum_{i=i_M-w_l}^{i_M} (y_i - A s_i)^2} \quad (\text{B.1})$$

$$\text{TVR} = \frac{1000}{A \cdot w_r} \sqrt{\sum_{i=i_M}^{i_M+w_r} (y_i - A s_i)^2} \quad (\text{B.2})$$

where A is the amplitude of the pulse as measured by the optimum filter, i_M is the maximum position of the pulse, y_i is the filtered pulse, s_i is the filtered average pulse scaled to unitary amplitude and aligned to the filtered pulse, and $w_{l,r}$ are the left and right width at half maximum of the average pulse. The maximum of the average pulse is aligned with the maximum of the filtered pulse, fractional delays are handled with a linear interpolation of the data samples.

The parameter χ_{OT}^2 described in Sec. 5.3 is similar, with these differences:

- The parameter is unique, and is computed including both the left and the right part of the pulse.
- The average pulse is splined to avoid digitization effects. This should give better performances than the linear interpolation in TVL and TVR, in particular at high energies.
- A minimization is performed, varying the amplitude A and the alignment between the pulse and the splined average pulse. This should give better performances at high energies.
- We do not divide by A , in order to have a shape parameter that does not depend on energy. The χ^2 , in fact, does not depend on the amplitude if the pulse shape remains constant with energy, since the noise is always the same. This removes the dependence at low energies, where the shape change is negligible with respect to the noise.

- The normalization constant is computed using the noise, such that the average χ_{OT}^2 at low energies is 1 on all channels, allowing easy cuts.

The distribution of TVL and TVR on channel 3 background runs is shown in Fig. B.1, to be compared with the χ_{OT}^2 distribution in Fig. 6.6. All parameters behave very well at high energy, separating the signal from non-physical pulses. In the region below 100 keV the χ_{OT}^2 distribution of the signal is flat, allowing the same cut to be used down to zero energy. Moreover the average value in this region is 1 on all channels and the same cut can be applied to different channels. Therefore our parameter is already “linearized” at low energy and does not require additional linearization steps like other shape parameters. The low energy distribution of TVL

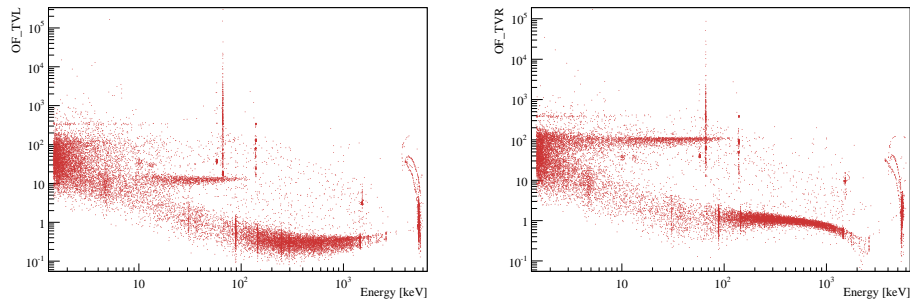


Figure B.1. TVL (left) and TVR (right) distribution on ch3. Background runs of CCVR2.

and TVR is shown in Fig. B.2, where the events with $\chi_{OT}^2 < 2.2$ are shown in blue.

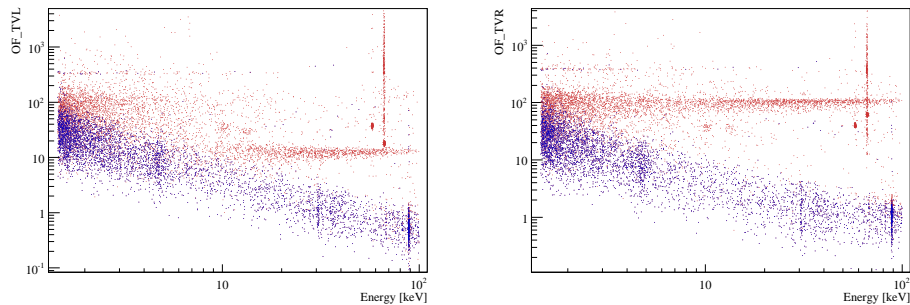


Figure B.2. TVL (left) and TVR (right) low energy distribution on ch3. All events in red, events with $\chi_{OT}^2 < 2.2$ in blue. Background runs of CCVR2.

Appendix C

Optimum Trigger Efficiencies in CCVR2 run

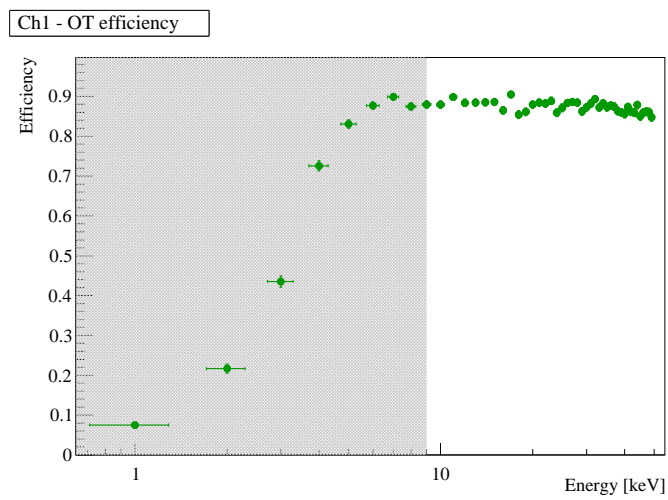


Figure C.1. Optimum Trigger efficiency on CCVR2 channel 1: MC particle in green. The region in gray is discarded due to amplitude estimator bias.

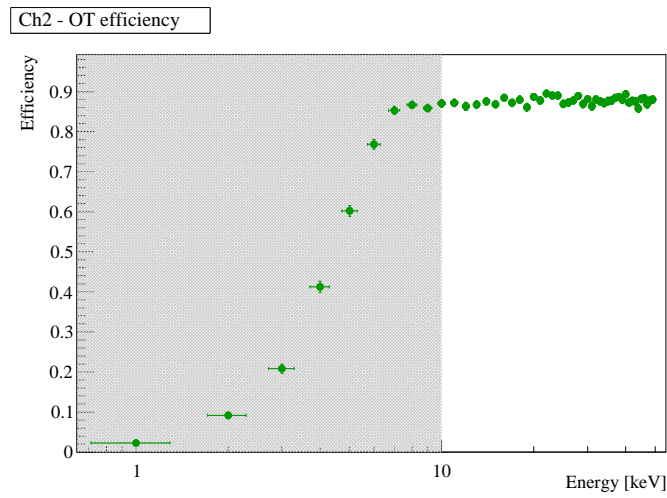


Figure C.2. Optimum Trigger efficiency on CCVR2 channel 2: MC particle in green. The region in gray is discarded due to amplitude estimator bias.

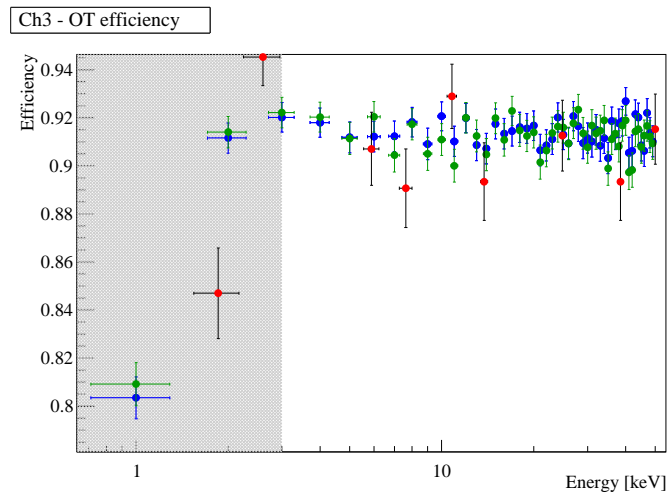


Figure C.3. Optimum Trigger efficiency on CCVR2 channel 3: N-Pulses data in red, MC particle in green, MC heater in blue. The region in gray is discarded due to amplitude estimator bias.

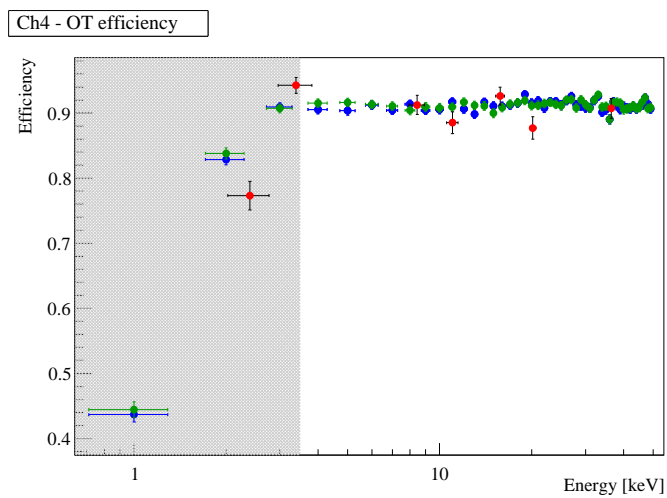


Figure C.4. Optimum Trigger efficiency on CCVR2 channel 4: N-Pulses data in red, MC particle in green, MC heater in blue. The region in gray is discarded due to amplitude estimator bias.

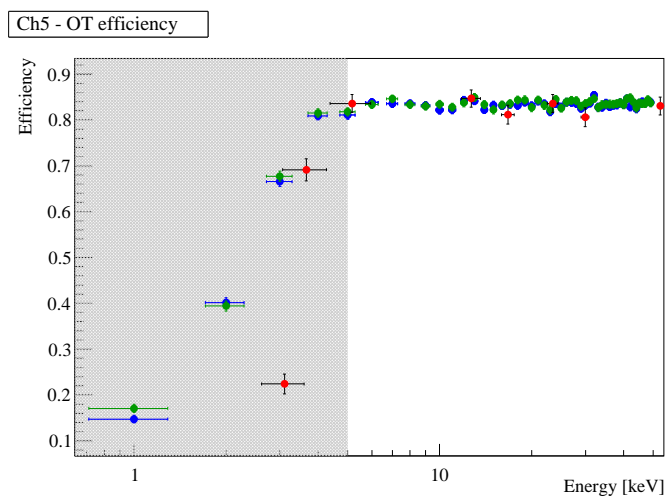


Figure C.5. Optimum Trigger efficiency on CCVR2 channel 5: N-Pulses data in red, MC particle in green, MC heater in blue. The region in gray is discarded due to amplitude estimator bias.

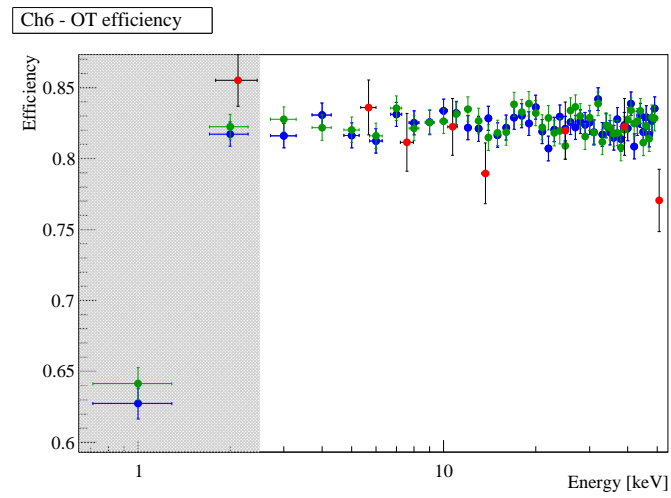


Figure C.6. Optimum Trigger efficiency on CCVR2 channel 1: N-Pulses data in red, MC particle in green, MC heater in blue. The region in gray is discarded due to amplitude estimator bias.

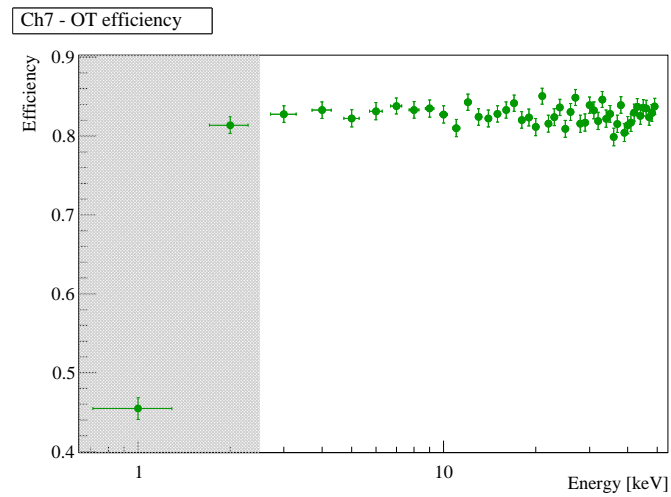


Figure C.7. Optimum Trigger efficiency on CCVR2 channel 7: MC particle in green. The region in gray is discarded due to amplitude estimator bias.

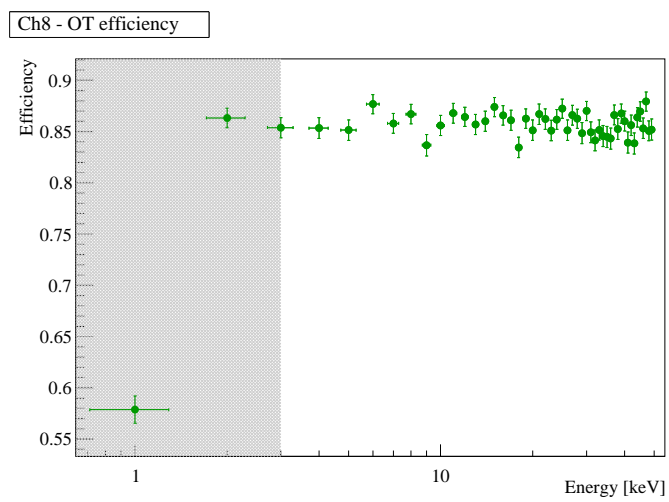


Figure C.8. Optimum Trigger efficiency on CCVR2 channel 8: MC particle in green. The region in gray is discarded due to amplitude estimator bias.

Appendix D

Comparison with standard trigger on N-Pulses measurement

The N-Pulses measurement was also processed with the CUORE standard trigger. As can be seen in the following plots, both the triggers obtain the same efficiencies on the plateau but Optimum Trigger thresholds are about one order of magnitude lower.

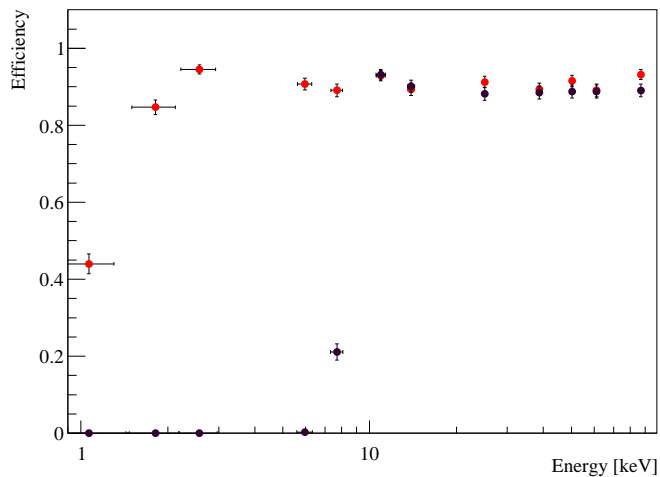


Figure D.1. Optimum Trigger (red) and standard trigger (dark) efficiency on CCVR2 channel 3.

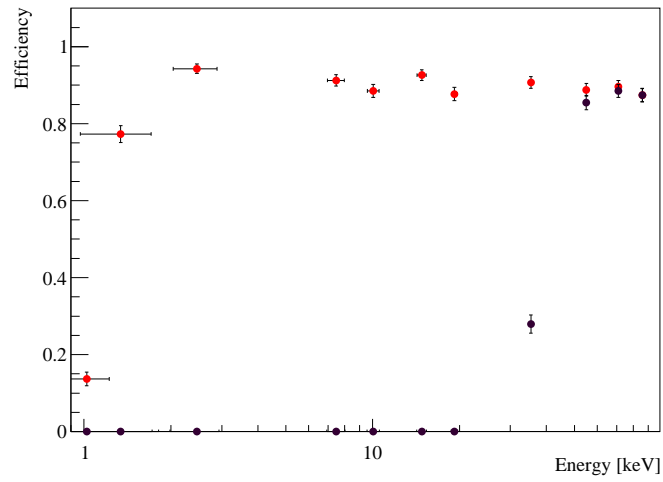


Figure D.2. Optimum Trigger (red) and standard trigger (dark) efficiency on CCVR2 channel 4.

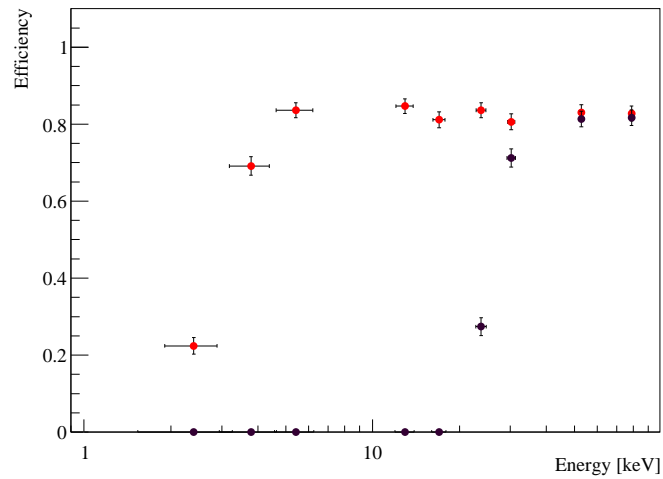


Figure D.3. Optimum Trigger (red) and standard trigger (dark) efficiency on CCVR2 channel 5.

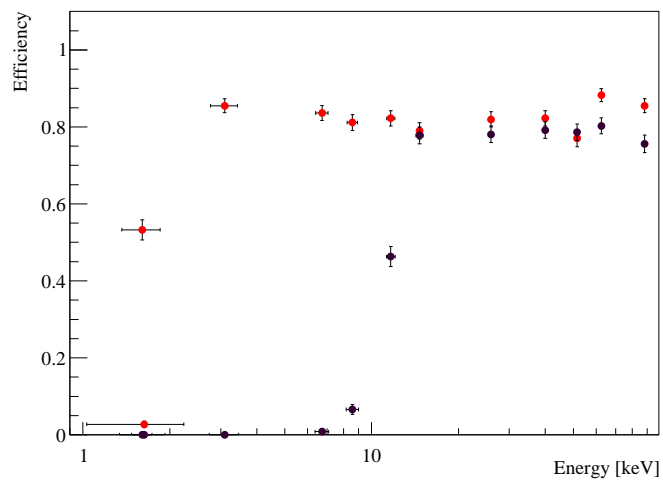


Figure D.4. Optimum Trigger (red) and standard trigger (dark) efficiency on CCVR2 channel 6.

Bibliography

- [1] F. Zwicky, “Republication of: The redshift of extragalactic nebulae,” *General Relativity and Gravitation*, vol. 41, pp. 207–224, Jan 2009.
- [2] B. Ryden, *Introduction to cosmology*. Addison-Wesley, 2003.
- [3] V. C. Rubin and W. K. Ford, Jr., “Rotation of the Andromeda Nebula from a Spectroscopic Survey of Emission Regions,” *The Astrophysical Journal*, vol. 159, p. 379, Feb. 1970.
- [4] K. G. Begeman, A. H. Broeils, and R. H. Sanders, “Extended rotation curves of spiral galaxies. Dark haloes and modified dynamics,” *MNRAS*, vol. 249, p. 523, 1991.
- [5] G. G. Raffelt, “Dark matter: Motivation, candidates and searches,” Dec 1997, hep-ph/9712538.
- [6] N. A. Bahcall, L. M. Lubin, and V. Dorman, “Where is the dark matter?,” *The Astrophysical Journal Letters*, vol. 447, no. 2, p. L81, 1995.
- [7] R. G. Carlberg *et al.*, “Galaxy Cluster Virial Masses and Omega,” *The Astrophysical Journal*, vol. 462, p. 32, May 1996, arXiv:astro-ph/9509034.
- [8] A. E. Evrard, C. A. Metzler, and J. F. Navarro, “Mass Estimates of X-Ray Clusters,” *The Astrophysical Journal*, vol. 469, p. 494, Oct. 1996, arXiv:astro-ph/9510058.
- [9] I. Smail *et al.*, “A comparison of direct and indirect mass estimates for distant clusters of galaxies,” *The Astrophysical Journal*, vol. 479, no. 1, p. 70, 1997.
- [10] S. Burles, K. M. Nollett, and M. S. Turner, “Big-bang nucleosynthesis: Linking inner space and outer space,” 1999, astro-ph/9903300.
- [11] C. Amsler *et al.*, “Review of particle physics,” *Physics Letters B*, vol. 667, no. 1-5, pp. 1 – 6, 2008. Review of Particle Physics.
- [12] D. Fixsen, C. Bennett, and J. Mather, “COBE far infrared absolute spectrophotometer observations of Galactic lines,” *The Astrophysical Journal*, vol. 526, p. 207, 1999.
- [13] R. Coladonato, “Cosmic Background Explorer,” *ELV payload environment*, pp. 78–80, 1991.

- [14] C. L. Bennett *et al.*, “Four-year COBE DMR cosmic microwave background observations: Maps and basic results,” *The Astrophysical Journal Letters*, vol. 464, p. L1, 1996.
- [15] E. Komatsu *et al.*, “Five-year Wilkinson Microwave Anisotropy Probe observations: cosmological interpretation,” *The Astrophysical Journal Supplement Series*, vol. 180, p. 330, 2009.
- [16] E. Komatsu *et al.*, “Seven-Year Wilkinson Microwave Anisotropy Probe (WMAP) Observations: Cosmological Interpretation,” 2010, 1001.4538.
- [17] G. Hinshaw *et al.*, “Three-year Wilkinson Microwave Anisotropy Probe (WMAP) observations: Temperature analysis,” *The Astrophysical Journal Supplement Series*, vol. 170, no. 2, p. 288, 2007.
- [18] D. G. York *et al.*, “The Sloan Digital Sky Survey: Technical summary,” *The Astronomical Journal*, vol. 120, no. 3, p. 1579, 2000.
- [19] P. J. E. Peebles, *Principles of physical cosmology*. Princeton Series in Physics, Princeton University Press, 1993.
- [20] W. J. Percival *et al.*, “Baryon Acoustic Oscillations in the Sloan Digital Sky Survey Data Release 7 Galaxy Sample,” *Mon. Not. Roy. Astron. Soc.*, vol. 401, pp. 2148–2168, 2010, 0907.1660.
- [21] M. Davis, M. Lecar, C. Pryor, and E. Witten, “The formation of galaxies from massive neutrinos,” *The Astrophysical Journal*, vol. 250, pp. 423–431, 1981.
- [22] G. R. Blumenthal, S. M. Faber, J. R. Primack, and M. J. Rees, “Formation of galaxies and large-scale structure with cold dark matter,” *Nature*, vol. 311, pp. 517–525, Oct. 1984.
- [23] B. Paczynski, “Gravitational microlensing by the galactic halo,” *Astrophysical Journal*, vol. 304, no. 1 Pt 1, pp. 1–5, 1986.
- [24] K. Griest, “Galactic microlensing as a method of detecting massive compact halo objects,” *The Astrophysical Journal*, vol. 366, pp. 412–421, 1991.
- [25] R. Nemiroff, “Probing galactic halo dark matter with microlensing,” *Astronomy and Astrophysics*, vol. 247, pp. 73–76, 1991.
- [26] A. De Rújula, P. Jetzer, and E. Masso, “On the nature of the dark halo of our galaxy,” *Astronomy and Astrophysics*, vol. 254, p. 99, 1992.
- [27] C. Afonso *et al.*, “Limits on Galactic dark matter with 5 years of EROS SMC data,” *Astronomy and Astrophysics*, vol. 400, pp. 951–956, Mar. 2003.
- [28] M. Milgrom, “A modification of the Newtonian dynamics as a possible alternative to the hidden mass hypothesis,” *The Astrophysical Journal*, vol. 270, pp. 365–370, 1983.
- [29] M. C. Weisskopf *et al.*, “An Overview of the Performance and Scientific Results from the Chandra X-Ray Observatory,” *Publications of the Astronomical Society of the Pacific*, vol. 114, pp. 1–24, 2002.

- [30] M. Johns, “The Giant Magellan Telescope (GMT),” in *Proceedings of SPIE*, vol. 6267, pp. 762–776, 2006.
- [31] G. Nurre, “Hubble Space Telescope,” in *Upper and Middle Atmospheric Density Modeling Requirements for Spacecraft Design and Operations*, pp. 73–87, 1987.
- [32] D. Clowe, A. Gonzalez, and M. Markevitch, “Weak-Lensing Mass Reconstruction of the Interacting Cluster 1 E 0657-558: Direct Evidence for the Existence of Dark Matter,” *The Astrophysical Journal*, vol. 604, no. 2, pp. 596–603, 2004.
- [33] D. Clowe *et al.*, “A direct empirical proof of the existence of dark matter,” *The Astrophysical Journal Letters*, vol. 648, no. 2, p. L109, 2006.
- [34] A. Mahdavi, H. Hoekstra, A. Babul, D. D. Balam, and P. L. Capak, “A dark core in abell 520,” *The Astrophysical Journal*, vol. 668, no. 2, p. 806, 2007.
- [35] M. Bradač *et al.*, “Revealing the properties of dark matter in the merging cluster macs j0025.4–1222,” *The Astrophysical Journal*, vol. 687, no. 2, p. 959, 2008.
- [36] G. Jungman, M. Kamionkowski, and K. Griest, “Supersymmetric dark matter,” *Physics Reports*, vol. 267, pp. 195–373, 1996, hep-ph/9506380.
- [37] R. Peccei and H. Quinn, “Constraints imposed by CP conservation in the presence of pseudoparticles,” *Physical Review D*, vol. 16, no. 6, pp. 1791–1797, 1977.
- [38] M. Turner, “Windows on the axion,” *Physics Reports*, vol. 197, no. 2, pp. 67–97, 1990.
- [39] J. Preskill and M. Wise Frank, “Cosmology of the invisible axion,” *Physics Letters B*, vol. 120, no. 1-3, pp. 127–132, 1983.
- [40] G. Cantatore, M. Karuza, V. Lozza, and G. Raiteri, “Search for solar Axion Like Particles in the low energy range at CAST,” *Nuclear Instruments and Methods in Physics Research Sec.A*, 2009.
- [41] M. Hotz *et al.*, “Limits on thermally-distributed halo dark-matter axions from ADMX,” in *APS Meeting Abstracts*, p. 9006, 2010.
- [42] E. Zavattini *et al.*, “New PVLAS results and limits on magnetically induced optical rotation and ellipticity in vacuum (12 pages),” *Physical Review-Section D-Particles and Fields*, vol. 77, no. 3, pp. 32006–32006, 2008.
- [43] N. Okada and O. Yasuda, “A sterile neutrino scenario constrained by experiments and cosmology,” *International Journal of Modern Physics*, vol. A12, pp. 3669–3694, 1997, hep-ph/9606411.
- [44] M. Maltoni, “Sterile neutrinos after the first miniboone results,” *Journal of Physics: Conference Series*, vol. 110, no. 8, p. 082011, 2008.
- [45] S. P. Martin, “A Supersymmetry Primer,” 1997, hep-ph/9709356.

- [46] G. Bertone, D. Hooper, and J. Silk, “Particle dark matter: Evidence, candidates and constraints,” *Physics Reports*, vol. 405, pp. 279–390, 2005, hep-ph/0404175.
- [47] S. W. Barwick *et al.*, “Measurements of the cosmic-ray positron fraction from 1 to 50 GeV,” *The Astrophysical Journal Letters*, vol. 482, p. L191, 1997.
- [48] J. Olzem, “AMS Collaboration,” in *Talk given at the 7th UCLA Symposium on Sources and Detection of Dark Matter and Dark Energy in the Universe, Marina del Ray, CA*, 2006.
- [49] T. G. Guzik *et al.*, “The ATIC long duration balloon project,” *Advances in Space Research*, vol. 33, no. 10, pp. 1763–1770, 2004.
- [50] W. B. Atwood *et al.*, “The large area telescope on the Fermi gamma-ray space telescope mission,” *The Astrophysical Journal*, vol. 697, p. 1071, 2009.
- [51] P. Brun, J. Glicenstein, E. Moulin, and M. Vivier, “Dark matter searches with HESS,” *Nuclear Instruments and Methods in Physics Research Sec.A*, 2010.
- [52] I. V. Moskalenko and A. W. Strong, “Production and propagation of cosmic-ray positrons and electrons,” *The Astrophysical Journal*, vol. 493, pp. 694–707, 1998, astro-ph/9710124.
- [53] O. Adriani *et al.*, “An anomalous positron abundance in cosmic rays with energies 1.5-100 GeV,” *Nature*, vol. 458, pp. 607–609, 2009, 0810.4995.
- [54] F. Barao, “AMS-02 Collaboration,” *Nuclear Instruments and Methods in Physics Research Sec.A*, vol. 535, p. 134, 2004.
- [55] Y. Fukuda *et al.*, “Evidence for oscillation of atmospheric neutrinos,” *Physical Review Letters*, vol. 81, pp. 1562–1567, 1998, hep-ex/9807003.
- [56] A. Achterberg *et al.*, “IceCube Collaboration,” in *Journal of Physics: Conference Series*, vol. 60, IOP Publishing, 2007.
- [57] V. Bertin *et al.*, “Status and first results of the ANTARES neutrino telescope,” *Nuclear Instruments and Methods in Physics Research Sec.A*, vol. 604, no. 1-2, pp. S136–S142, 2009.
- [58] J. D. Lewin and P. F. Smith, “Review of mathematics, numerical factors, and corrections for dark matter experiments based on elastic nuclear recoil,” *Astroparticle Physics*, vol. 6, no. 1, pp. 87 – 112, 1996.
- [59] J. Primack, D. Seckel, and B. Sadoulet, “Detection of cosmic dark matter,” *Annu. Rev. Nucl. Part. Sci.*, vol. 38, pp. 751–807, 1988.
- [60] R. H. Helm, “Inelastic and elastic scattering of 187-mev electrons from selected even-even nuclei,” *Physical Review*, vol. 104, pp. 1466–1475, Dec 1956.
- [61] M. T. Ressell *et al.*, “Nuclear shell model calculations of neutralino-nucleus cross sections for $si29$ and $ge73$,” *Physical Review D*, vol. 48, pp. 5519–5535, Dec 1993.

- [62] V. I. Dimitrov, J. Engel, and S. Pittel, “Scattering of weakly interacting massive particles from $ge73$,” *Physical Review D*, vol. 51, pp. R291–R295, Jan 1995.
- [63] A. Alessandrello *et al.*, “The bolometers as nuclear recoil detectors,” *Nuclear Instruments and Methods in Physics Research Sec.A*, vol. 409, pp. 451–453, May 1998.
- [64] S. Y. F. Chu, L. P. Ekstrom, and R. B. Firestone, “The Lund/LBNL nuclear data search,” Available at nucleardata.nuclear.lu.se/nucleardata/toi (accessed July 2005).
- [65] A. K. Drukier, K. Freese, and D. N. Spergel, “Detecting cold dark-matter candidates,” *Physical Review D*, vol. 33, pp. 3495–3508, Jun 1986.
- [66] R. Bernabei *et al.*, “First results from DAMA/LIBRA and the combined results with DAMA/NaI,” *The European Physical Journal C-Particles and Fields*, vol. 56, no. 3, pp. 333–355, 2008.
- [67] R. Gaitskell, V. Mandic, and J. Filippini, “Direct detection of wimp dark matter, sensitivity plots: An interactive plotter for experimental and theoretical data.” Available online at <http://dmtools.brown.edu:8080/>.
- [68] R. Bernabei *et al.*, “The liquid xenon set-up of the DAMA experiment,” *Nuclear Instruments and Methods in Physics Research Sec.A*, vol. 482, no. 3, pp. 728–743, 2002.
- [69] A. Hime, “DEAP & CLEAN detectors for low energy particle astrophysics,” in *AIP Conference Proceedings*, vol. 842, p. 852, IOP Publishing, 2006.
- [70] P. Benetti *et al.*, “First results from a dark matter search with liquid argon at 87-K in the Gran Sasso underground laboratory,” *Astroparticle Physics*, vol. 28, pp. 495–507, 2008, astro-ph/0701286.
- [71] C. Regenfus *et al.*, “The argon dark matter experiment (ArDM),” in *Journal of Physics: Conference Series*, vol. 203, p. 012024, IOP Publishing, 2010.
- [72] A. Minamino *et al.*, “XMASS experiment, dark matter search with liquid xenon detector,” *Nuclear Instruments and Methods in Physics Research Sec.A*, 2010.
- [73] G. J. Alner *et al.*, “Nuclear recoil limits from the ZEPLIN I liquid xenon WIMP dark matter detector,” *New Astronomy Reviews*, vol. 49, no. 2-6, pp. 245–249, 2005.
- [74] G. J. Alner *et al.*, “First limits on wimp nuclear recoil signals in zeplin-ii: a two phase xenon detector for dark matter detection,” 2007, astro-ph/0701858.
- [75] V. N. Lebedenko *et al.*, “Limits on the spin-dependent wimp-nucleon cross sections from the first science run of the zeplin-iii experiment,” *Physical Review Letters*, vol. 103, p. 151302, Oct 2009.

- [76] M. Atac *et al.*, “ZEPLIN IV: A future large-scale liquid xenon dark matter detector,” *New Astronomy Reviews*, vol. 49, no. 2-6, pp. 283–287, 2005.
- [77] J. Angle *et al.*, “First Results from the XENON10 Dark Matter Experiment at the Gran Sasso National Laboratory,” *Physical Review Letters*, vol. 100, p. 021303, 2008, 0706.0039.
- [78] E. Aprile *et al.*, “First Dark Matter Results from the XENON100 Experiment,” *Arxiv preprint arXiv:1005.0380*, 2010.
- [79] E. Aprile *et al.*, “The XENON Collaboration,” *Arxiv preprint astro-ph/0502279*.
- [80] D. N. McKinsey *et al.*, “The LUX dark matter search,” in *Journal of Physics: Conference Series*, vol. 203, p. 012026, IOP Publishing, 2010.
- [81] L. Baudis *et al.*, “First Results from the Heidelberg Dark Matter Search Experiment,” *Physical Review D*, vol. 63, p. 022001, 2001, astro-ph/0008339.
- [82] I. G. Irastorza *et al.*, “Status of igex dark matter search at canfranc underground laboratory,” 2002, astro-ph/0211535.
- [83] I. Abt *et al.*, “GERDA Collaboration,” *Nuclear Instruments and Methods in Physics Research Sec.A*, vol. 570, no. 3, p. 479, 2007.
- [84] S. Elliott *et al.*, “The MAJORANA project,” in *Journal of Physics: Conference Series*, vol. 173, p. 012007, IOP Publishing, 2009.
- [85] E. Armengaud *et al.*, “Preliminary results of a WIMP search with EDELWEISS-II cryogenic detectors,” *Arxiv preprint arXiv:1011.2319*, 2010.
- [86] Z. Ahmed *et al.*, “Results from the Final Exposure of the CDMS II Experiment,” 2009, 0912.3592.
- [87] S. Roth *et al.*, “Direct dark matter search with CRESST and EURECA,” *Progress in Particle and Nuclear Physics*, 2010.
- [88] S. Cebrian *et al.*, “and ROSEBUD Collaboration,” *Physics Letters B*, vol. 563, p. 48, 2003.
- [89] T. Girard *et al.*, “Simple dark matter search results,” 2005, hep-ex/0505053.
- [90] S. Archambault *et al.*, “Dark Matter Spin-Dependent Limits for WIMP Interactions on 19-F by PICASSO,” *Physics Letters B*, vol. 682, pp. 185–192, 2009, 0907.0307.
- [91] E. Behnke *et al.*, “Spin-Dependent WIMP Limits from a Bubble Chamber,” *Science*, vol. 319, no. 5865, p. 933, 2008.
- [92] G. Sciolla *et al.*, “The DMTPC project,” in *Journal of Physics: Conference Series*, vol. 179, p. 012009, IOP Publishing, 2009.
- [93] J. Davis, Raymond, D. S. Harmer, and K. C. Hoffman, “Search for neutrinos from the sun,” *Physical Review Letters*, vol. 20, pp. 1205–1209, 1968.

- [94] P. Anselmann *et al.*, “Solar neutrinos observed by GALLEX at Gran Sasso,” *Physics Letters B*, vol. 285, pp. 376–389, 1992.
- [95] J. N. Abdurashitov *et al.*, “Measurement of the Solar Neutrino Capture Rate by SAGE and Implications for Neutrino Oscillations in Vacuum,” *Physical Review Letters*, vol. 83, pp. 4686–4689, 1999, astro-ph/9907131v2.
- [96] Q. R. Ahmad *et al.*, “Direct evidence for neutrino flavor transformation from neutral-current interactions in the Sudbury Neutrino Observatory,” *Physical Review Letters*, vol. 89, p. 011301, 2002, nucl-ex/0204008.
- [97] K. Eguchi *et al.*, “First results from KamLAND: Evidence for reactor anti-neutrino disappearance,” *Physical Review Letters*, vol. 90, p. 021802, 2003, hep-ex/0212021.
- [98] S. Abe *et al.*, “Precision Measurement of Neutrino Oscillation Parameters with KamLAND,” *Physical Review Letters*, vol. 100, p. 221803, 2008, 0801.4589.
- [99] L. L. Chau and W. Y. Keung, “Comments on the Parametrization of the Kobayashi-Maskawa Matrix,” *Physical Review Letters*, vol. 53, p. 1802, 1984.
- [100] T. Schwetz, M. Tortola, and J. W. F. Valle, “Three-flavour neutrino oscillation update,” 2008, 0808.2016.
- [101] C. Kraus *et al.*, “Final Results from phase II of the Mainz Neutrino Mass Search in Tritium β Decay,” *Eur. Phys. J.*, vol. C40, pp. 447–468, 2005, hep-ex/0412056.
- [102] V. M. Lobashev *et al.*, “Direct search for neutrino mass and anomaly in the tritium beta-spectrum: Status of ‘Troitsk neutrino mass’ experiment,” *Nucl. Phys. Proc. Suppl.*, vol. 91, pp. 280–286, 2001.
- [103] G. Drexlin, “KATRIN: Direct measurement of a sub-eV neutrino mass,” *Nucl. Phys. Proc. Suppl.*, vol. 145, pp. 263–267, 2005.
- [104] A. Monfardini *et al.*, “The microcalorimeter arrays for a rhenium experiment (MARE): A next-generation calorimetric neutrino mass experiment,” *Prog. Part. Nucl. Phys.*, vol. 57, pp. 68–70, 2006, hep-ex/0509038.
- [105] A. Strumia and F. Vissani, “Neutrino masses and mixings and,” 2006, hep-ph/0606054.
- [106] S. R. Elliott, A. A. Hahn, and M. K. Moe, “Direct evidence for two-neutrino double-beta decay in Se- 82,” *Physical Review Letters*, vol. 59, pp. 2020–2023, 1987.
- [107] R. N. Mohapatra and P. B. Pal, *Massive Neutrinos in Physics and Astrophysics*. World Scientific, 3rd ed., 2004. ISBN: 98123807101.
- [108] J. Schechter and J. W. F. Valle, “Neutrinoless double- β decay in $SU(2)\times U(1)$ theories,” *Physical Review D*, vol. 25, pp. 2951–2954, Jun 1982.

- [109] F. T. Avignone, S. R. Elliott, and J. Engel, “Double Beta Decay, Majorana Neutrinos, and Neutrino Mass,” *Rev. Mod. Phys.*, vol. 80, pp. 481–516, 2008, 0708.1033.
- [110] I. Ogawa *et al.*, “Search for neutrino-less double beta decay of Ca-48 by CaF-2 scintillator,” *Nuclear Physics A*, vol. 730, pp. 215–223, 2004.
- [111] H. V. Klapdor-Kleingrothaus *et al.*, “Latest Results from the Heidelberg-Moscow Double Beta Decay Experiment,” *Eur. Phys. J.*, vol. A12, pp. 147–154, 2001, hep-ph/0103062.
- [112] H. V. Klapdor-Kleingrothaus, I. V. Krivosheina, A. Dietz, and O. Chkvorets, “Search for neutrinoless double beta decay with enriched ^{76}Ge in Gran Sasso 1990-2003,” *Physics Letters B*, vol. 586, pp. 198–212, 2004, hep-ph/0404088.
- [113] R. Arnold *et al.*, “First results of the search of neutrinoless double beta decay with the NEMO 3 detector,” *Physical Review Letters*, vol. 95, p. 182302, 2005, hep-ex/0507083.
- [114] R. Arnold *et al.*, “Double beta decay of Zr-96,” *Nucl. Phys.*, vol. A658, pp. 299–312, 1999.
- [115] F. A. Danevich *et al.*, “Search for 2 beta decay of cadmium and tungsten isotopes: Final results of the Solotvina experiment,” *Physical Review C*, vol. 68, p. 035501, 2003.
- [116] M. Pavan, “Introduction to double beta decay experiments and cuore,” in *Talk given at the XXIV International Conference on Neutrino Physics and Astrophysics, Athens, Greece*, 2010.
- [117] R. Bernabei *et al.*, “Investigation of beta beta decay modes in Xe-134 and Xe-136,” *Physics Letters B*, vol. 546, pp. 23–28, 2002.
- [118] . J. Argyriades, “Measurement of the Double Beta Decay Half-life of ^{150}Nd and Search for Neutrinoless Decay Modes with the NEMO-3 Detector,” 2008, 0810.0248.
- [119] F. T. Avignone, G. S. King, and Y. G. Zdesenko, “Next generation double-beta decay experiments: Metrics for their evaluation,” *New J. Phys.*, vol. 7, p. 6, 2005.
- [120] S. R. Elliott and P. Vogel, “Double beta decay,” *Ann. Rev. Nucl. Part. Sci.*, vol. 52, pp. 115–151, 2002, hep-ph/0202264.
- [121] J. Menendez, A. Poves, E. Caurier, and F. Nowacki, “Deformation and the Nuclear Matrix Elements of the Neutrinoless Double Beta Decay,” 2008, 0809.2183.
- [122] C. E. Aalseth *et al.*, “The Igex ^{76}Ge Neutrinoless Double-Beta Decay Experiment: Prospects for Next Generation Experiments,” *Physical Review D*, vol. 65, p. 092007, 2002, hep-ex/0202026.

- [123] A. Staudt, K. Muto, and H. V. Klapdor-Kleingrothaus, "Calculation of 2ν and 0ν double-beta decay rates," *Europhys. Lett.*, vol. 13, pp. 31–36, 1990.
- [124] H. V. Klapdor-Kleingrothaus, A. Dietz, H. L. Harney, and I. V. Krivosheina, "Evidence for Neutrinoless Double Beta Decay," *Mod. Phys. Lett.*, vol. A16, pp. 2409–2420, 2001, hep-ph/0201231.
- [125] R. Arnold *et al.*, "Technical design and performance of the NEMO 3 detector," *Nuclear Instruments and Methods in Physics Research Sec.A*, vol. 536, pp. 79–122, 2005, physics/0402115.
- [126] E. Fiorini and T. O. Niinikoski, "Low temperature calorimetry for rare decays," *Nuclear Instruments and Methods in Physics Research Sec.A*, vol. 224, p. 83, 1984.
- [127] A. Alessandrello *et al.*, "A New search for neutrinoless beta beta decay with a thermal detector," *Physics Letters B*, vol. 335, pp. 519–525, 1994.
- [128] C. Arnaboldi *et al.*, "A Calorimetric Search on Double Beta Decay of ^{130}Te ," *Physics Letters B*, vol. 557, pp. 167–175, 2003, hep-ex/0211071.
- [129] C. Arnaboldi *et al.*, "A New Limit on the Neutrinoless DBD of ^{130}Te ," *Physical Review Letters*, vol. 95, p. 142501, 2005, hep-ex/0501034.
- [130] C. Arnaboldi *et al.*, "First results on neutrinoless double beta decay of Te-130 with the calorimetric CUORICINO experiment," *Physics Letters B*, vol. 584, pp. 260–268, 2004.
- [131] C. Arnaboldi *et al.*, "Results from a search for the $0\nu\beta\beta$ -decay of ^{130}Te ," *Physical Review C*, vol. 78, p. 035502, 2008, 0802.3439.
- [132] C. Arnaboldi *et al.*, "CUORE: A Cryogenic Underground Observatory for Rare Events," *Nuclear Instruments and Methods in Physics Research Sec.A*, vol. 518, pp. 775–798, 2004, hep-ex/0212053v1.
- [133] R. Ardito *et al.*, "CUORE: A cryogenic underground observatory for rare events," 2005, hep-ex/0501010.
- [134] S. P. Ahlen *et al.*, "Study of penetrating cosmic ray muons and search for large scale anisotropies at the Gran Sasso Laboratory," *Physics Letters B*, vol. 249, pp. 149–156, 1990.
- [135] P. Belli *et al.*, "Deep underground neutron flux measurement with large bf-3 counters," *Il Nuovo Cimento A*, vol. 101, pp. 959–966, 1989.
- [136] M. Redshaw *et al.*, "Masses of ^{130}Te and ^{130}Xe and double- β -decay q value of ^{130}Te ," *Physical Review Letters*, vol. 102, p. 212502, May 2009.
- [137] V. A. Rodin, A. Faessler, F. Simkovic, and P. Vogel, "Assessment of uncertainties in QRPA 0ν beta beta-decay nuclear matrix elements," *Nuclear Physics A*, vol. 766, pp. 107–131, 2006, 0706.4304.

- [138] V. A. Rodin, A. Faessler, F. Šimkovic, and P. Vogel, “Erratum: Assessment of uncertainties in QRPA $\nu\beta\beta$ -decay nuclear matrix elements,” 2007, 0706.4304v1 [nucl-th]. 0706.4304v1 [nucl-th].
- [139] M. Kortelainen and J. Suhonen, “Nuclear matrix elements of neutrinoless double beta decay with improved short-range correlations,” *Physical Review C*, vol. 76, p. 024315, 2007, 0708.0115 [nucl-th]. 0708.0115 [nucl-th].
- [140] S. Simom, “Application of Low Temperature Calorimetry to Radioactive Measurements,” *Nature*, vol. 135, p. 763, 1935.
- [141] Y. B. Levinson, “Nonequilibrium Phonons in Nonmetallic Crystals,” *Modern Problems in Condensed Matter Sciences*, vol. 16, pp. 91–143, 1986. ISBN: 0-444-86989-1.
- [142] N. F. Mott and J. H. Davies, “Metalinsulator transition in doped semiconductors,” *Philosophical Magazine B*, vol. 42, pp. 845–858, 1980.
- [143] A. Miller and E. Abrahams, “Impurity conduction at low concentrations,” *Physical Review*, vol. 120, pp. 745–755, 1960.
- [144] K. M. Itoh *et al.*, “Neutron transmutation doping of isotopically engineered Ge,” *Applied Physics Letters*, vol. 64, pp. 2121–2123, 1994.
- [145] M. Pedretti. *et al.*, “Measurement of thermal properties for modeling and optimization of large mass bolometers,” *Physica B*, vol. 329, pp. 1614–1615, 2003.
- [146] C. Arnaboldi *et al.*, “The programmable front-end system for CUORICINO, an array of large-mass bolometers,” *IEEE Trans. Nucl. Sci.*, vol. 49, pp. 2440–2447, 2002.
- [147] F. Bellini, A. Bryant, M. Carrettoni, L. Ejzak, L. Kogler, M. Martinez, M. Pavan, and M. Vignati, “Cuoricino first-level data analysis and official n-tuple production,” CUORE Internal Note 2010-01, <https://wiki.hep.wisc.edu/cuore/AnalysisTopics>, 2010.
- [148] E. Gatti and P. F. Manfredi, “Processing the signals from solid state detectors in elementary particle physics,” *Rivista del Nuovo Cimento*, vol. 9N1, pp. 1–146, 1986.
- [149] C. Arnaboldi *et al.*, “The temperature stabilization system of CUORICINO: An array of macro bolometers,” *IEEE Trans. Nucl. Sci.*, vol. 52, pp. 1630–1637, 2005.
- [150] C. Arnaboldi, G. Pessina, and E. Previtali, “A programmable calibrating pulse generator with multi- outputs and very high stability,” *IEEE Trans. Nucl. Sci.*, vol. 50, pp. 979–986, 2003.
- [151] W. H. Press, S. A. Teukolsky, W. T. Vetterling, and B. P. Flannery, *Numerical recipes in C (2nd ed.): the art of scientific computing*. New York, NY, USA: Cambridge University Press, 1992.

-
- [152] J. Gibbs, “Fourier’s series,” *Nature*, vol. 59, p. 200, 1898.
- [153] M. Vignati, *Model of the Response Function of CUORE Bolometers*. PhD thesis, La Sapienza Università di Roma, 2009.
- [154] M. Bianchetti *et al.*, “Competition between particle-hole and particle-particle correlations in forbidden electron capture: The case of ^{123}Te ,” *Physical Review C*, vol. 56, pp. R1675–R1677, Oct 1997.
- [155] D. Münstermann and K. Zuber, “An alternative search for the electron capture of ^{123}Te ,” *Journal of Physics G: Nuclear and Particle Physics*, vol. 29, no. 2, p. B1, 2003.
- [156] S. Pirro *et al.*, “Dark matter results in the MIBETA experiment,” 2000. Prepared for 4th International Symposium on Sources and Detection of Dark Matter in the Universe (DM 2000), Marina del Rey, California, 23-25 Feb 2000.
- [157] C. Savage, G. Gelmini, P. Gondolo, and K. Freese, “Compatibility of DAMA/LIBRA dark matter detection with other searches,” *JCAP*, vol. 0904, p. 010, 2009, 0808.3607.
- [158] E. Aprile *et al.*, “First Dark Matter Results from the XENON100 Experiment,” 2010, 1005.0380.